POLITECNICO DI TORINO

Faculty of Engineering

Master's Degree in Communications and Computer Networks Engineering

Master's Degree Thesis

Design and Validation of a Technology Demonstrator for an Autonomous Orbit Determination System for Small Satellite Constellation

Mentor

Prof. Roberto GARELLO

Candidate

Pier Luigi MANFRINI

OCTOBER 2022

Abstract

This thesis work is inserted within the context of a project for a deep-space autonomous navigation system proposed by Argotec, an Italian aerospace engineering company based in Turin.

The mission considered is *"Autonomous oRbit dEtermination System for Smallsats Constellation (ARES4SC)"* which aims at developing a constellation of five small satellites capable of semiautonomously determining their precise ephemerides after being deployed around a planet.

Son of Zeus and Hera, Ares is the Greek god of war and from its Roman counterpart, Mars, the ARES4SC mission took the reference planet, with the concept being however suitable for any other celestial body.
In this scenario, this thesis presents the studies and the development steps conducted in order to design and digitally implement, on a Software Defined Radio, both the transmission and the reception of a suitable Inter Satellite Link (ISL) signal capable of extracting the radiometric observables needed in order to derive a valid orbital solution for the constellation.
ISLs share simultaneously the same frequency portion in a CDMA scheme adopting deterministic yet random-like spreading sequences that both reduce the Multiple Access Interference and allow a two-way ranging between satellites.
Other core architectural element of the constellation is a single Ultra Stable Oscillator to be placed in one satellite only. The stability of such frequency source has been characterized and the possibility to adopt a commercial (hence cheaper but presumably less accurate) oscillator has been verified by proving its noise suppression when dealing with short distances between satellites.

Thesis Summary

In the field of aerospace engineering, no matter how specialized and peculiar a mission can be, the telecommunication engineer is always involved. Spacecrafts without a reliable communication payload would be useful as much as rocks thrown in the void. That being said, it is now easier to guess the implications and the reasons behind the proposed Master's degree thesis which has been carried in Argotec, an Italian aerospace engineering company based in Turin and founded in 2008 by David Avino. Argotec's key product is, among others, an innovative small satellite platform with a form factor which is not far from resembling a server rack. As a matter of fact, nowadays technological progress has unleashed a multitude of new possibilities in favor of space exploration by allowing to condense in smaller bodies all what once used to be heavy and voluminous. As a consequence, costs have lowered, production times have become shorter and the market competition, along with research investments, signed the dawn of a new era. Cubesats, a fancy and compact term that entered the literature to address exactly these extremely small shaped spacecrafts, provide in fact big advantages not only due to their low volumes but primarily for their reduced weight with respect to legacy ones. This makes escaping Earth's gravity easier, cheaper and introduces the possibility to deploy more satellites at once, with a single rocket launch. Argotec's real strenght is the capability of facing an all-in-house development of such cubesats withstanding high quality and space-grade standards that no one has ever reached before. Moreover, coordinated constellations of satellites are now a reality and they allow for new mission concepts that only few years ago were new to the human kind. Amonge those, one project from Argotec certainly stands out.

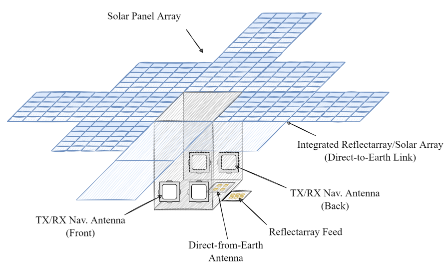

Its name, already self-describing, is *"Autonomous oRbit dEtermination System for a Smallsat Constellation"* (in short ARES4SC) and during the last semester it was my honor to carry out part of it.

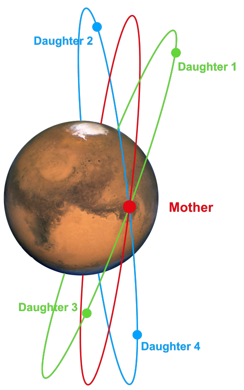

In few words the mission consists in the realization of a constellation of five small satellites which, once thrown into orbit around Mars, is able to semiautonomously determine its orbit by exploiting the planet's gravity knowledge and signals exchanged among the components of the constellation itself. The latters allow for radiometric observables, range and Doppler, to be extracted from the so called Inter Satellite Links (ISL) among the satellites, while a precise mapping of the gravity field will permit those relative measures to be converted into metrics (position and velocity) which are absolute with respect to the planetocentric reference plane. In this thesis work the study of the design of the ISL signal has been carried out, followed by its implementation using a Universal Software Radio Peripheral (USRP). Since the frequency management of the constellation has been entrusted to a Code Division Multiple Access (CDMA) the developed signal had to both grant the possibility of sharing the spectrum and performing a two-way coherent ranging: both these needs can be achieved by adopting a pseudo noise, deterministic, spread spectrum sequence. Given the fitting scenario, a CCSDS recommended standard has been identified and used as a guideline in choosing the appropriate spreading sequence and modulation.

The suggested modulation scheme - Unbalanced Quadrature Phase Shift Keying (UQPSK) - and the suggested pseudo noise sequences have been implemented and tested both in transmission and in reception to verify the possibility to acquire and track the signal, much like other GNSS signals.

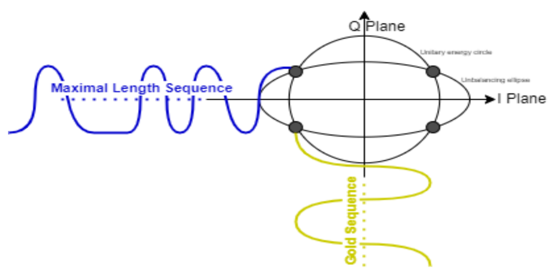

The selected spreading codes belong to two different yet similar families of pseudo random sequences with good auto and cross correlation properties. In fact, the transmitted signal is composed of two simultaneous chip streams: one modulating its in-phase component with a Gold sequence and the other carrying a Maximal Length sequence to modulate the in-quadrature component. Both sequences can be quickly generated in hardware with the use of Linear Feedback Shift Registers (LFSRs). Just like for the transmission, at the receiver-side the Digital Signal Processing needed for acquisition and tracking of the signal has been developed and implemented first in MATLAB and finally in a custom C++ software interfaced to the USRP through its hardware drivers. Similarly to a GNSS receiver, a *Cross Ambiguity Function* and a mutually aiding loop composed of a *Delay Locked Loop* and a *Phase Locked Loop* are part of the core implemented functions that allow the receiver to track the evolution of the incoming pseudo noise ranging sequence and of the carrier's phase.

One other interesting aspect of this thesis work has concerned the frequency sources. In fact, in order to obtain stable measurements the signals exchanged in the ISLs need to be generated using Ultra Stable Oscillators (USO) capable of excellent frequency stabilities. This allows the observer to trace the measured frequency shifts back to Doppler effects and not to oscillator instabilities. In the proposed constellation, it has been planned that only one spacecraft, the *Mother SpaceCraft (MSC)*, will be in charge of computing the relative measures of range and range-rate. The other satellites will participate by simply transponding the signal generated by (and received from) the MSC in a coherent way for what concerns the received frequency, according to a standardized turnaround ratio, and the received ranging code. Therefore, it is the MSC the one carrying the unique USO of the constellation and one aspect that has been investigated has been the possibility of using a cheaper Commercial Of-The-Shelf (COTS) oscillator instead of a heavier and more expensive one. To characterize frequency stability the two main metrics of phase noise and Allan deviation have been considered and the concept of phase noise suppression in the case of a short Round Trip Light Time have been tested and verified in laboratory.

Acknowledgements

In the society we live in, everyone should do its job. I loved doing mine. However nobody does great stuff alone. Being here, writing the acknowledgments section of a dissertation I am truly proud of, would not have been possible on my own: resources, affection, mentorship and passion have been the fundamental inputs to my system. Sometimes they came from people I already relied on and sometimes from those who were the least expected ones.
Explicit mentions are however deserved for the unconditioned support received from my family, for my girlfriend's love I could daily benefit from, and for the brilliant people of the Argotec's Telecommunications Unit which, along with my relator R. Garello, made me significantly grow professionally.
Special greetings go to *Leone*!

To all my inputs!
Sincerely, Pier

Table of Contents

List of Tables

List of Figures

Acronyms

ADC Analog to Digital Converter.

ADEV Allan Deviation.

AGC Automatic Gain Control.

API Application Programming Interface.

ARES4SC Autonomous oRbit dEtermination System for Smallsats Constellation.

ASI Agenzia Spaziale Italiana.

ASM Attached Synchronization Marker.

AVAR Allan Variance.

AWGN Additive White Gaussian Noise.

BLF Best Lock Frequency.

BPSK Binary Phase Shift Keying.

CCSDS Consultative Committee for Space Data Systems.

CDMA Code Division Multiple Access.

CORDIC COordinate Rotation DIgital Computer.

COTS Commercial Off-The-Shelf.

CSS Channel Select Synthesizer.

CTL Carrier Tracking Loop.

DAC Digital to Analog Converter.

DDC Digital Downconversion Chain.

DLL Delay Locked Loop.

DSC Daughter SpaceCraft.

DSN Deep Space Network.

DSP Digital Signal Processing.

DSS Deep Space Station.

DSSS Direct Sequence Spread Spectrum.

DUC Digital Upconversion Chain.

EIRP Equivalent Isotropic Radiated Power.

EKF Extended Kalman Filter.

ESA European Space Agency.

FIFO First-In First-Out.

FPGA Field Programmable Gate Array.

FSL Free Space Loss.

FTS Frequency and Timing Subsystem.

GNSS Global Navigation Satellite System.

HPBW Half Power Beam Width.

IDC Intermediate to Digital Converter.

IF Intermediate Frequency.

ISL Inter Satellite Link.

LFSR Linear Feedback Shift Register.

LNA Low Noise Amplifier.

LOS Line Of Sight.

MAI Multiple Access Interference.

MPSL Maximum Peak Side Lobe.

MSC Mother SpaceCraft.

NASA National Aeronautics and Space Administration.

NRZ Non-Return-to-Zero.

OBC&DH On-Board Computer & Data Handling.

OCXO Oven Controlled Crystal Oscillator.

PCB Printed Circuit Board.

PLL Phase Locked Loop.

PN Phase Noise or Pseudo Noise depending on the context.

PSD Power Spectral Density.

QPSK Quadrature Phase Shift Keying.

RAM Random Access Memory.

RF Radio Frequency.

RID Radio frequency to Intermediate frequency Downconverter.

RRP Receiver and Ranging Processor.

RTLT Round Trip Light Time.

SDR Software Defined Radio.

SF Spreading Factor.

SFCG Space Frequency Coordination Group.

SMA Sub Miniature version A.

SNR Signal to Noise Ratio.

SRRC Square Root Raised Cosine Filter.

SSB Single Side Band.

TCXO Temperature Compensated Crystal Oscillator.

TD Technology Demonstrator.

TE Technology Element.

TRL Technology Readiness Level.

TT&C Telemetry, Tracking & Commands.

UMTS Universal Mobile Telecommunications Service.

UPA Uplink Processor Assembly.

UQPSK Unbalanced Quadrature Phase Shift Keying.

USO Ultra Stable Oscillator.

USRP Universal Software Radio Peripheral.

VCO Voltage Controlled Oscillator.

VSA Vector Signal Analyzer.

Chapter 1

Introduction

Nowadays space exploration is in a truly steep and rapid rise both in terms of new technologies being embedded in more and more compact solutions and in terms of human and economic capital invested in it. Companies are trying to push further the quality and the distance over which missions are capable to perform and obtain scientifically relevant results. Whichever goal we might have the ambition to reach, a reliable communication system is a crucial element without which nothing would be possible.

When considering deep space missions, the communication link has to be carefully designed in order to sustain huge distances as well as atmospheric and stars' radiation effects. For such scenarios an ultra-capable ground infrastructure has to be used on Earth in order to send commands and to receive telemetries along with useful scientific data. A top-notch solution for this demands comes from the NASA's Deep Space Network (DSN) specifically designed for interplanetary missions and consisting of three 70-meters dish antennas (along with some supplementary 34-meters ones) equally spaced by 120 degrees in longitude to allow a continuous Line Of Sight (LOS) with any space probe independently from the Earth's rotational state.

Given the enormous effort needed in terms of highly engineered ground infrastructures, costs and human capital, one of the hottest research topics is the capability of making spacecraft more and more autonomous and independent from Earth aiding, thus lessening the burden on the ground antennas. Moreover, all those missions foreseeing some kind of formation flight such as constellations of satellites would require a high degree of earth-based support in terms of signals exchanged.

In scenarios like the above mentioned one, it is however possible to exploit signals exchanged among the components of the constellation itself in order to reduce the support needed from the Earth Ground Segment and improve the autonomy, and possibly the quality, of the overall system. In the literature such signals are usually referred to as Inter Satellite Link (ISL).

In this context many companies are designing missions and use-cases that exploit ISLs to exchange data and extract radiometric observable measures. Specifically, Argotec is an Italian aerospace engineering company which collaborates with the most relevant private and public entities in order to deliver to space compact solutions in the form of nanosatellites and "Autonomous oRbit dEtermination System for Smallsats Constellation (ARES4SC)" is one of its most recent projects aiming at the exploitation of ISL for the benefit of an increased independence and autonomy of a constellation system.

1.1 Scope

The scope of this thesis is the Design and Validation of a Technology Demonstrator for the ARES4SC project, focusing on the signals architecture of an ISL capable of extracting radiometic observables such as range and range-rate (Doppler). These relative measures can then be converted into absolute measures (w.r.t. a planetocentric reference system) by the knowledge of the gravitational field of the planet around which a small-satellites constellation is orbiting.
The signals will be studied starting from the state-of-the-art recommendations provided by the Consultative Committee for Space Data Systems (CCSDS) and then implemented and tested in laboratory through USRPs (Universal Software Radio Peripherals) and custom software (mainly MATLAB and C++).

Furthermore, the concept of phase noise suppression in case of a two-way link with short RTLT will be investigated and finally verified in laboratory.

1.2 Document Outline

In this section a brief description of the contents of each chapter is provided, facilitating the user's navigation throughout the document.

Chapter 2 describes the full ARES4SC project which is being carried in collaboration with *Sapienza University of Rome* and with *Agenzia Spaziale Italiana (ASI)*. Objectives of the project as well as the link budget and the prototyped satellite platforms are also discussed.

Chapter 3 provides the details of the technology demonstrator: the laboratory setup that has been used to carry on the tests. Theoretical error budgets both for the range and range-rate have been also reported and kept as a reference.

Chapter 4 analyzes the state-of-the-art solutions, such as the TX and RX ISL signal architectures, to which the software implementation is inspired.

Chapter 5 describes software implementation to transmit, receive and track the designed ISL signal on a Universal Software Radio Peripheral.

Chapter 6 focuses on the Ultra Stable Oscillator (USO) stability measurements analyzed in laboratory. It provides also an explanation of the considered metrics: Phase Noise and Allan Variance (AVAR). A laboratory test aimed at verifying the phase noise suppression for a short RTLT link is presented.

Chapter 7 recaps the obtained results evaluating the possible future improvements of the implemented system.

Chapter 2

ARES4SC Mission

2.1 Overview and Innovative aspects

The ARES4SC project consists in the development of a navigation system composed of a constellation of 5 satellites operating beyond Earth orbit and able to autonomously determine their relative and absolute positions.

The innovative aspect of this mission is the ability to obtain a valid orbit solution exploiting an ISL tracking instead of the traditional links with Earth yielding to enhanced measurement accuracies and a higher degree of autonomy. The absolute positioning is referred to the target planet around which the system will orbit and can be obtained converting the radiometric observables generated by the ISLs (range and Doppler) into an orbital solution thanks to the knowledge of the planet's gravitational field and rotational state which will provide the dynamic model for the constellation system. Having a precise knowledge of the ephemerides, the constellation system will provide future explorative missions with navigation support for manned or unmanned probes or landers.

In addition to the autonomous orbit determination and navigation capabilities, the proposed system will have to rely on a link with Earth to perform clock synchronization with the UTC (Coordinated Universal Time) or TAI (International Atomic Time) terrestrial time, to deliver scientific data back to Earth and to occasionally (on a daily or weekly basis) check the consistency of the orbital state of the constellation.

The reference planet for the ARES4SC study is Mars (Figure 2.1 and Table 2.1) but the system configuration is highly adaptable to any other celestial body for which previous explorative missions already mapped its gravitational field.

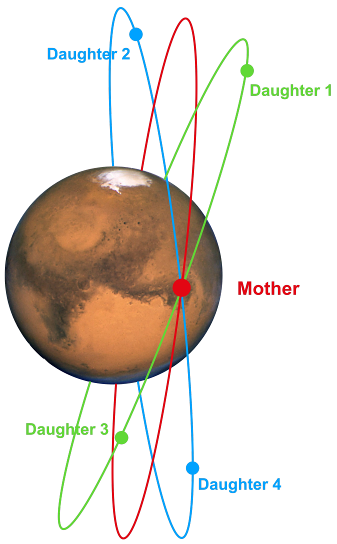

Figure 2.1: Orbital Plane of the 5 satellites constellation

Table 2.1: Orbital Planes Configuration

	Plane #1 (DSC 2,4)	**Plane #2** (MSC)	**Plane #3** (DSC 1,3)
Semi-Major Axis [km] (Altitude)	8106.7 (4717.2)	8106.7 (4717.2)	8106.7 (4717.2)
Eccentricity	0	0	0
Inclination [deg]	60	75	90
MA [deg]	± 42	0	± 48
Orbital Period [hrs]	6.16 (T/4)	6.16 (T/4)	6.16 (T/4)

In the considered scenario, three different orbital planes can be identified: a main one for the Mother SpaceCraft (MSC) and two for the four Daughter SpaceCraft (DSC). All have a quite low orbit with respect to the Mars terrain and an orbital period of a quarter of the planet's one. DSC 1 and 2 (as well as DSC 3 and 4) will span an evaluated maximum separation angle of 38.2 degrees with respect to the MSC.

2.2 Objectives of the ARES4SC study

The objective of the ARES4SC study is the evaluation of the feasibility of the proposed constellation system both in terms of available technologies and in terms of economical sustainability.

The first part of the project, carried out by *Sapienza University of Rome*, consists in the definition of a mathematical dynamical model of the system thanks to which an extended non-linear version of the Kalman Filter[1] (the EKF) will be able to convert the radiometric observables, hence the relative positioning and velocity, into a precise orbital state. For such dynamical model, an a-priori full knowledge of the Martian gravitational field is required as well as other non-gravitational accelerating factors such as the solar radiating pressure.

Subsequently, a laboratory Technology Demonstrator (TD) has to be designed and realized in order to validate the critical Technology Elements (TE) of the constellation system, a necessary step to bring the whole architecture to a Technology Readiness Level (TRL) of 4 (See section 2.3). From a technology-related point of view the TD should validate an architecture able to perform Range and Range-Rate (Doppler) measurements using radio links in a Code Division Multiple Access (CDMA) scheme (Figure 2.2). The latter has been selected as the most convenient way of handling simultaneous and continuous communication between the satellites without increasing the frequency management complexity.

[1]An appendix on the basics of the linear version of the Kalman Filter is included at the end of this thesis

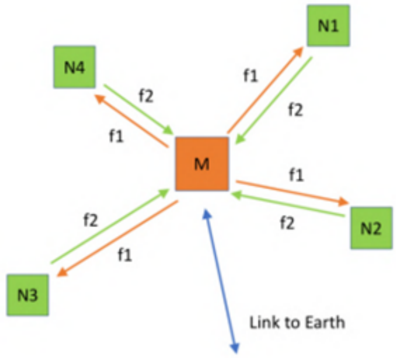

Figure 2.2: Radio Links Scheme

The two principal technical requirements that shall be verified in laboratory are the relative positioning accuracy to be less than 1 m and the relative speed accuracy to be less than 0.1 mm/s. Another fundamental goal of the technology demonstrator will be to verify the possibility of having only one Ultra Stable Oscillator (USO) in the whole constellation (to be placed on-board the Mother SpaceCraft), thus minimizing the overall cost of the mission or, for the same cost, maximizing the oscillator's performances. In fact, the MSC is the only one in charge of generating, within the computational limits of its On-Board Computer & Data Handling (OBC&DH) subsystem, the radiometric observables hence the need of having here an ultra-stable clock reference. In particular, the following four main objectives have been identified for the TD:

1. Prove the USO phase noise suppression
2. Verify that the longer the integration time of the received signal the better the Phase Noise (PN) suppression that we can achieve
3. Implement and test the CDMA-based radio link configuration to be used for the radio observables generation (Range and Doppler)
4. Simulate a realistic communication channel between the MSC and DSC (delay, Doppler shift, attenuation, Additive White Gaussian Noise)

2.3 TRL

The Technology Readiness Level (TRL) represents a way of expressing the maturity of a given product given its implied technologies. It ranges from 1 to 9, the latter being the required level to operate in a real space environment and to withstand the expected performances. It was originally developed by NASA in the 1970s [1] and nowadays also in use at the European Space Agency (ESA) [2]. Both level scales are reported in Table 2.2.

Table 2.2: Technology Readiness Levels as per NASA and ESA definitions

TRL	Current NASA Usage	Current ESA Usage
1	Basic principles observed and reported	Basic principles observed
2	Technology concept and/or application formulated	Technology concept formulated
3	Analytical and experimental critical function and/or characteristic proof of concept	Experimental proof of concept
4	Component and/or breadboard validation in laboratory environment	Technology validated in lab

TRL	**Current NASA Usage**	**Current ESA Usage**
5	Component and/or breadboard validation in relevant environment	Technology validated in relevant environment (industrially relevant environment in the case of key enabling technologies)
6	System/sub-system model or prototype demonstration in an operational environment	Technology demonstrated in relevant environment (industrially relevant environment in the case of key enabling technologies)
7	System prototype demonstration in an operational environment	System prototype demonstration in operational environment
8	Actual system completed and "flight qualified" through test and demonstration	System complete and qualified
9	Actual system flight proven through successful mission operations	Actual system proven in operational environment (competitive manufacturing in the case of key enabling technologies; or in space)

2.4 Satellite Platforms and Payloads

As mentioned, the proposed constellation comprehends one master spacecraft (the MSC) and four slave spacecraft (the DSC) continuously communicating with the former through a fully coherent two-way link. The coherency of the ISL is necessary in order to allow two-way Doppler measurements to be computed inside the OBC&DH of the Mother SpaceCraft [3].

The latter is designed to carry all the necessary payloads and antennas in order to enable the navigation and computing capabilities and it is therefore packed in a bigger platform of 12 units (12U) with respect to the other members of the constellation which are 6U satellites.
When referring to cubesats units, 1U corresponds to a volume of 10^3 cm^3.

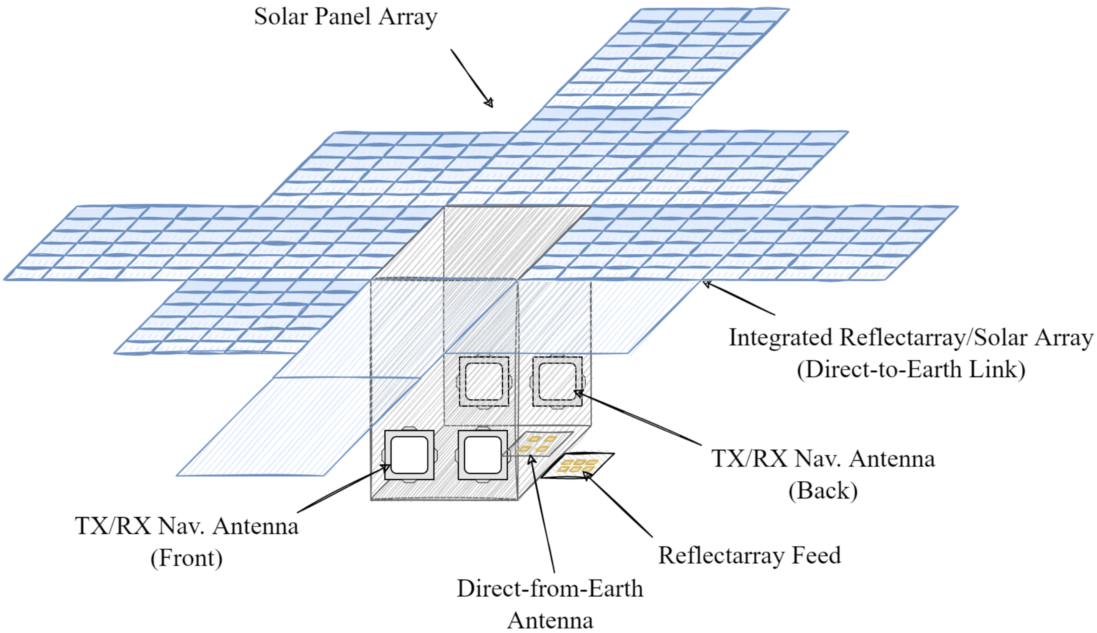

Figure 2.3: MSC Platform Top View

Figures 2.3 and 2.4 depict some of the MSC's payloads of major interest for a telecommunication perspective.

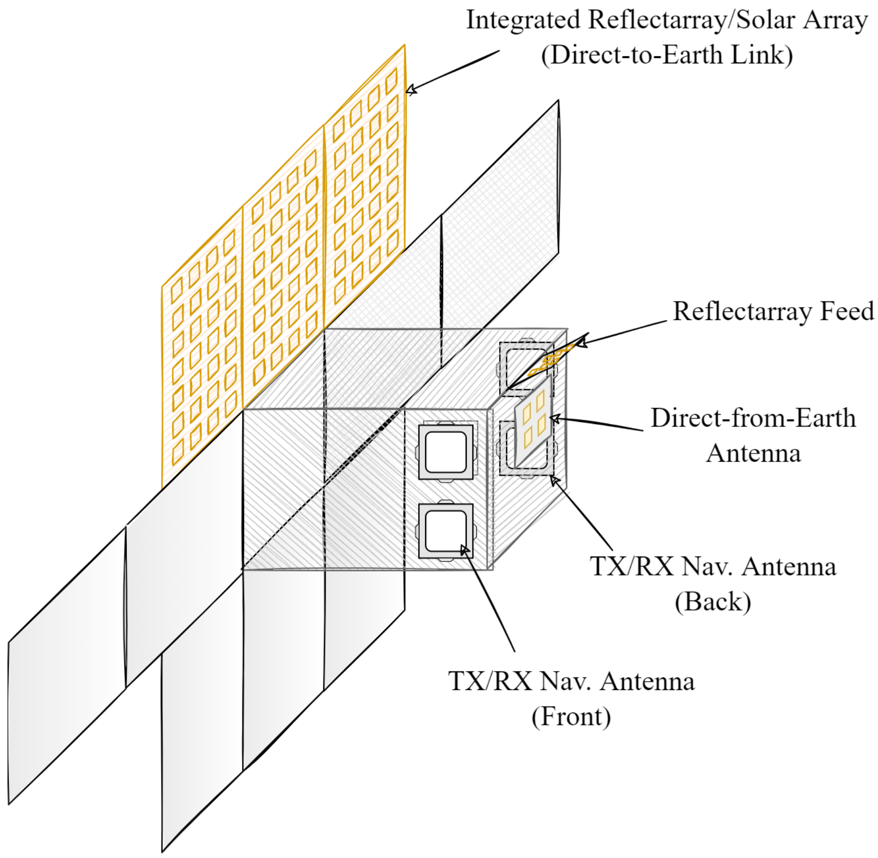

Figure 2.4: MSC Platform Bottom View

Along with the necessary subsystems for Structure, Thermal, Propulsion, Attitude Control, Electrical and Computing support, the Mother SpaceCraft is equipped with the unique USO of the constellation, a transponder for Telemetry, Tracking & Commands (TT&C) with Earth (matched with patch array and reflect array antennas), a transceiver for the generation of a CDMA-compliant ranging signal and the patch antennas for the communication with the leading and trailing DSC.

The transceiver's transmitted signal will be detailed in the core of this Thesis while the role of the USO, its stability characterization and its noise suppression concept will be detailed in **Chapter 6**.

Ultimately the platform schematic of the Daughter SpaceCraft is reported in Figure 2.5

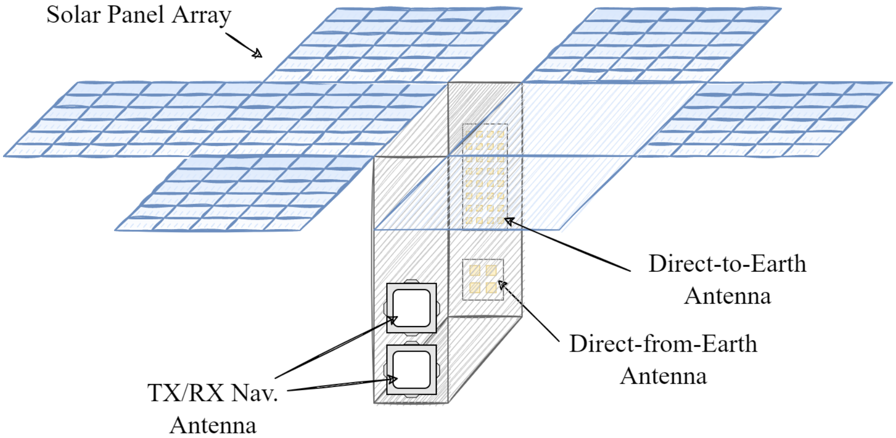

Figure 2.5: DSC Platform

2.5 Link Budget

In order to have a reference for the Technology Demonstrator results it is important to rely on a link budget study of the ISL, which constitutes the core element to ensure the feasibility of the communication link. It is worth to remind that the communication between the MSC and the DSCs happens continuously through directional patch antennas placed in the front (with respect to the MSC's velocity vector) and in the back of the mothercraft so that two daughtercrafts are always in visibility of the same antenna (see Figure 2.6).

Since the maximum separation angle between two DSCs with respect to the MSC is below 40 degrees, high gain antennas have to be excluded in order not to bring to the table too complex pointing requirements. Therefore high values of Half Power Beam Width (HPBW) should be preferred. Moreover, considering the radio frequency regulations defined by the Space Frequency Coordination Group (SFCG) for the Martian Orbit [4], the target RF for the project has fallen into the X-band.
In particular:

- 7.190 – 7.235 GHz for the MSC -> DSC forward link
- 8.450 – 8.500 GHz for the DSC -> MSC return link

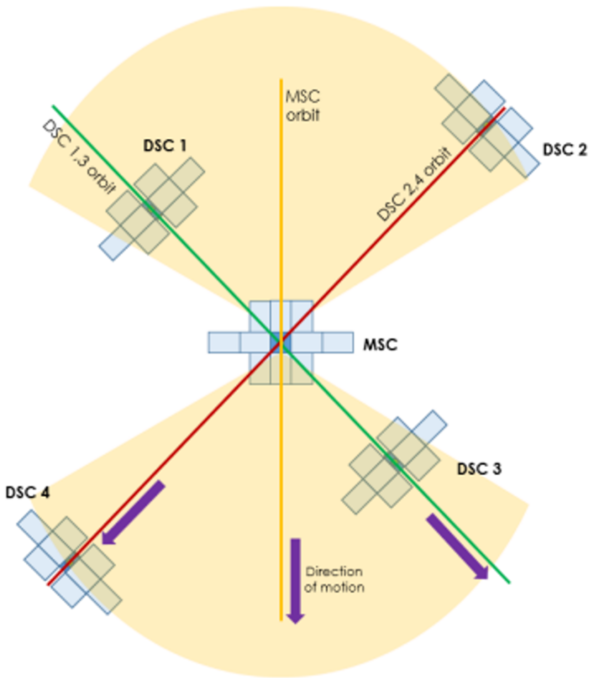

Figure 2.6: MSC's antenna beam coverage. Nadir view from Top.

The ratio between the forward and return link frequencies is determined by the Deep Space Network (DSN) which recommends a turnaround ratio of 880/749 for all the spacecraft transponders willing to receive and coherently retransmit an X-band signal to compute the two-way (or three-way) Doppler shift [5]. Such transponding ratio is actually just a suggestion and not a technological constraint. The Deep Space Stations are, in fact, already predisposed to track signals transmitted and received in specific frequency channels and anyone willing to exploit their tracking facilities might want to accommodate their preferences, but virtually any frequency can be served with a prior agreement. Furthermore in the considered scenario the ground stations are, of course, not involved by any means in the ISL tracking so the compliance to the turnaround ratio is just a matter of tradition considering also a possible better availability of COTS elements. On the other hand, respecting the transponding ratio may instead represent a more desirable feature for the link with Earth. The latter is taken charge of by the

MSC, while the DSC antennas for communicating with Earth are there just for redundancy.

The identified radiating element that mostly suits the need of the ARES4SC mission is the "*Anywaves X-band Payload Telemetry Antenna*" shown in Figure 2.7.

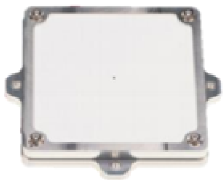

Figure 2.7: Anywaves X-band Patch Antenna

Specifications of the selected antenna are reported in Table 2.3 [6].

Table 2.3: Technical specifications of the MSC's navigation antenna

Metric	Value
Antenna Type	Patch Antenna
Supplier	Anywaves
Frequency Bands	8.025 – 8.4 GHz
Maximum Gain (@8.2 GHz)	12 dBi at boresight
RF power	> 3 W
Bandwidth	> 375 MHz
Half Power Beam Width	$\sim 40^o$
Polarization	LHCP or RHCP

Metric	**Value**
Connector	SMA female 50 Ω
Mass with connector	59 ± 3 g
Volume	L 72.6 x W 72.6 x H 11 mm^3
Operational Temperature	-120 °C / $+120$ °C
TRL	9

Initially, the proposed CDMA scheme (see section 4.1 for deeper details on this spread-spectrum multiple access technique) was thought to have the MSC transmitting a different PN code for each of its four daughtercraft in order to share the forward link frequencies with a multiple access logic.
The methodologies with which the codes can be distributed to the DSCs can be various. It is in fact possible to either use a *CDM-Time Division Multiplexing* technique in which, in rotation, chips are transmitted one at a time or, otherwise, adopt a majority voting scheme (*CDM-Majority Voting*) in which at each chip time the mother node transmits $+1$ or -1 depending on the majority of the chips, resolving possible conflictual situations (there is an even number of daughter nodes) by randomly choosing one of the two possible chip values.

However, the classical CDMA scheme has been selected, hence allowing the simultaneous transmission of all codes at the same time and forcing the MSC's power amplifier to work in saturation. This causes the peak power of the transmitted signal to have a reduction proportional to $1/N^2$ (1/16 for the considered constellation), and the average power to have a reduction of $10\log_{10}(\frac{1}{4}) = -6$ dB.
This led the radio link to be requiring such gain at the antennas (12 dB gain at boresight which translates to 6 dB gain at the two DSC placed one HPBW apart), but at the present state of the study this could be

no more considered since the multiple access scheme of choice, following the CCSDS recommendations (further details in Chapter 4) as in *"Data Transmission and PN Ranging for 2 GHz CDMA Link Via Data Relay Satellite"* Blue [7] and Green [8] books, suggests the same code to be transmitted from the MSC to all of the DSCs. The latter are then in charge of regenerating a different (their own) PN code to grant the multiple access for the return link spectrum. For these reasons, the final MSC's transmitting architecture could, in principle, use only one isotropic antenna instead of the two directional ones. However, Table 2.4 presents the radio link budget at X-band tailored for the worst-case scenario hence taking into account such loss due to the CDMA scheme adopted since the goal of the demonstrator is not the validation of the whole multiple access scheme but rather the validation of a single CDMA link generating radiometric observables.

Table 2.4: ISL Link Budget

Metric	Value	Notes
Slant Range	$7 \cdot 10^6$ m	Maximum LOS between MSC and DSC
Frequency	8.4 GHz	
Symbol Rate	$3 \cdot 10^6$ symbols/s	
Modulation	UQPSK	Unbalanced QPSK with $I : Q = 10 : 1$
Shaping Filter	Rectangular Pulse	no shaping
Bandwidth	6 MHz	Width of the main lobe from null to null
TX Power	2 W	33.01 dBm

Metric	Value	Notes
TX circuit loss	2 dB	
TX antenna gain	12 dBi	
TX pointing loss	1 dB	
EIRP	**15.88 W**	**42.01 dBm**
FSL	188.1 dB	@ 8.4 GHz for 7000 km (worst case)
CDMA scheme loss	6 dB	
RX antenna gain	12 dBi	
RX circuit loss	2 dB	
RX power	**6.180164 e-18 W**	**−142.09 dBm**
Noise spectral density (one-sided)	4.14194556e-21 $\frac{\mathrm{W}}{\mathrm{Hz}}$ (J)	$-173.83\frac{\mathrm{dBm}}{\mathrm{Hz}}$ (calculated for a $T_{sys} = 300\mathrm{K}$)
Received $\frac{\mathbf{P_c}}{\mathbf{N_o}}$ (worst case)	**31.74 dB Hz**	**The worst case is considering an ISL @ 8.4 GHz at the maximum slant range of 7000 km**

Metric	Value	Notes
Received $\frac{\mathbf{P_c}}{\mathbf{N_o}}$ (best case)	**33.44 dB Hz**	**The best case is considering an ISL @ 8.4 GHz at the minimum slant range of 5800 km for which the FSL decreases from 188.1 to 186.4 dB. The rx power in this case is −140.39 dB**

The obtained $\frac{P_c}{N_o}$ values, between 31.7 and 33.4 dB Hz are enough to acquire the code but are quite low if compared to those of GNSS navigation signals (40 $\sim$ 50 dB Hz) which also adopt a CDMA logic to share the frequency spectrum.

Chapter 3

Technology Demonstrator Architecture

In this chapter the structure as well as the hardware elements of the built Technology Demonstrator are presented.

3.1 USRPs and RF Front-End

Nowadays the whole field of telecommunications is moving towards architecture solutions which, spanning from the network infrastructures deployment to radio circuits design, are more and more customizable and manageable thanks to the reproduction in software of all the functions once performed through specific analog hardware elements. Remarkable is the case of Software Defined Radios (SDRs), or equivalently Universal Software Radio Peripheral (USRP)s, which allow engineers to move all the signal processing in the digital domain, hence treating the hardware as an API toward the RF world. Even though the architecture varies from model to model, the general principle is to have configurable RF front-ends, mixers, filters, oscillators and amplifiers to translate the analog high frequency signal from the antennas to a digital baseband (or to IF depending on the maximum feasible clock rate of the ADCs) complex domain suitable for some DSP to be performed in software, by an attached host computer. Before being transmitted to an external machine through an Ethernet or USB interface, the FPGA image of such radios generally offers features like digital fine frequency tuning (through a CORDIC), decimation (for the DDC) or interpolation (for the DUC).(Figure 3.1).

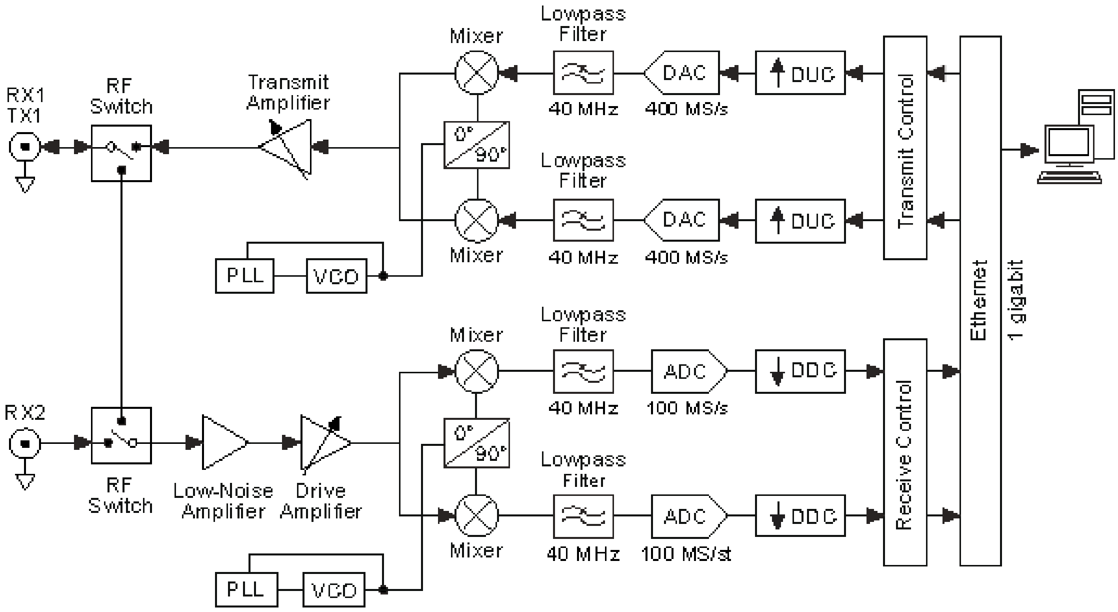

Figure 3.1: General USRP Architecture

As shown in Figure 3.2, the high-level system functions of the TD are decomposed in smaller subsystems, each highlighted by a dotted line. The roles of the MSC and a single DSC are reproduced with a testbed that aims at simulating a meaningful scenario, implementing a full transmission-reception chain of the signal to be exchanged in a single ISL.

Logically speaking the first function to implement is the stable reference signal generation which drives the MSC's hardware clock distribution tree. It will be provided by a Commercial Off-The-Shelf (COTS) USO for which the frequency stability shall be characterized, mainly in terms of Phase Noise and Allan Deviation (ADEV) (see Chap. 6). Different USOs shall be tested in order to prove the analytical

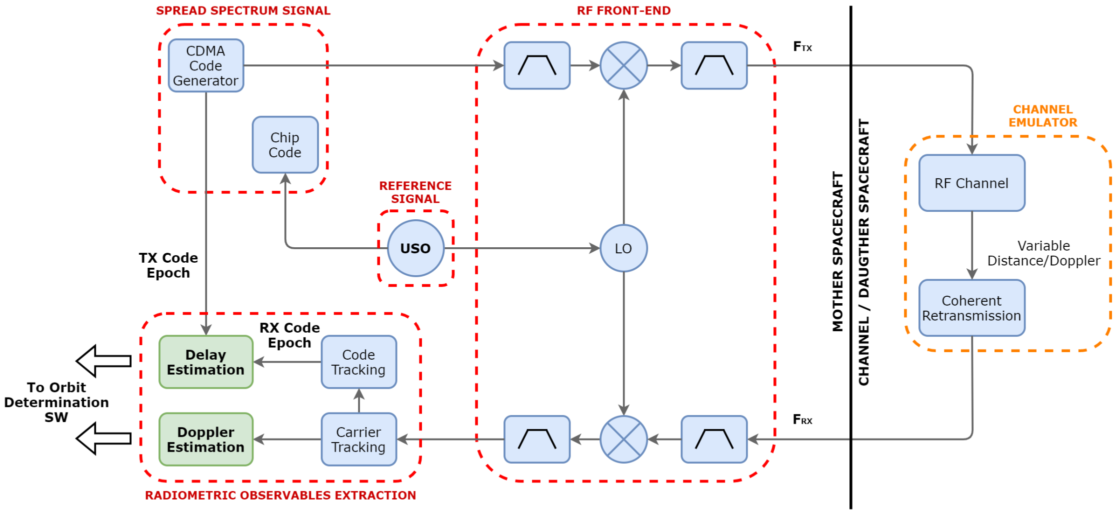

Figure 3.2: Technology Demonstrator Block Diagram

demonstration of phase noise suppression derived from the fact of having the same reference for both the transmission and the reception of a signal for which the expected Round Trip Light Time (RTLT) will be less than 50 ms (see Sec. 3.3.2).

Subsequently, the clock reference is exploited for the generation and Intermediate Frequency (IF) up-conversion of the spread spectrum CDMA code. The latter has to be properly chosen in order to both grant multiple DSCs to simultaneously transmit on the same frequency and to perform ranging measurements by comparing the same code epoch of reference in Tx and Rx stages.

The resulting ranging signal will be then filtered and up-converted to a final frequency which will be different from the one chosen for the final reference ARES4SC mission. In fact, since a simple prototyping solution could come from the exploitation of SDR which are typically limited to a maximum of 6 GHz, the operative RF could be translated into the S-band region without compromising the demonstrator's validity:

- 2.025 – 2.120 GHz for the MSC -> DSC forward link
- 2.200 – 2.300 GHz for the DSC -> MSC return link

After the RF signal has been transmitted, it should be impaired by a software-defined Channel Emulator in order to relate to the characteristics of the real-case environment. Attenuation, AWGN noise, delay and doppler will be added to the propagated signal according to link budget studies for the ARES4SC mission. Moreover, the Channel Emulator will include also the simulation of the DSC acquiring the transmitted signal, coherently generating their code and transmitting it toward the MSC.

Finally, signal down-conversion and radiometric observables extraction can be performed.

All the functions relative to the MSC are implemented, after a software testing and validation phase, on the USRP X300, while the behavior of the DSC will be simulated by the Channel Emulator software block running interfaced to a different software-defined radio, namely the USRP N210 (Figure 3.3)

Figure 3.3: USRP X300 (left) & USRP N210 (right)

The USRP X300 has been attached to two interfaces between its ADCs/DACs and the IFs, from 1 to 250 MHz: these interfaces are respectively the BasicRX and the BasicTX daughterboards. Similarly the USRP N210 is matched with the WBX daughterboard acting as a wideband interface between baseband and RF, allowing operating in the much wider range from 50 MHz to 2.2 GHz thanks to the presence of an embedded VCO.

The mentioned daughterboards are reported in Figure 3.4.
The overall block scheme of the MSC and DSCs's hardware implemen-

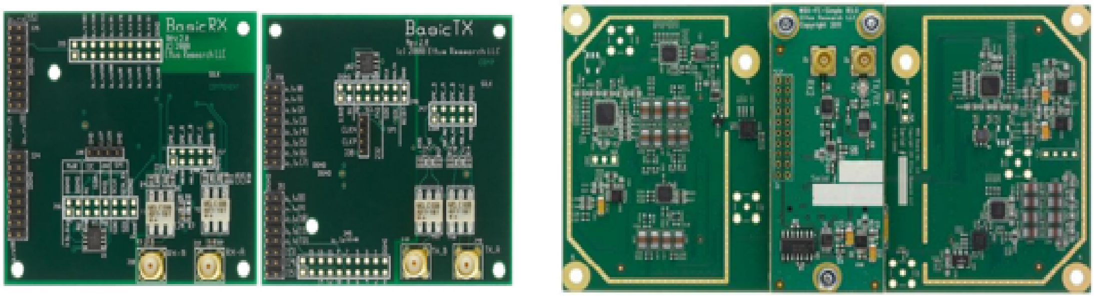

Figure 3.4: BasicRX and BasicTX (left) & WBX (right)

tations are shown in Figures 3.5 and 3.6 respectively.

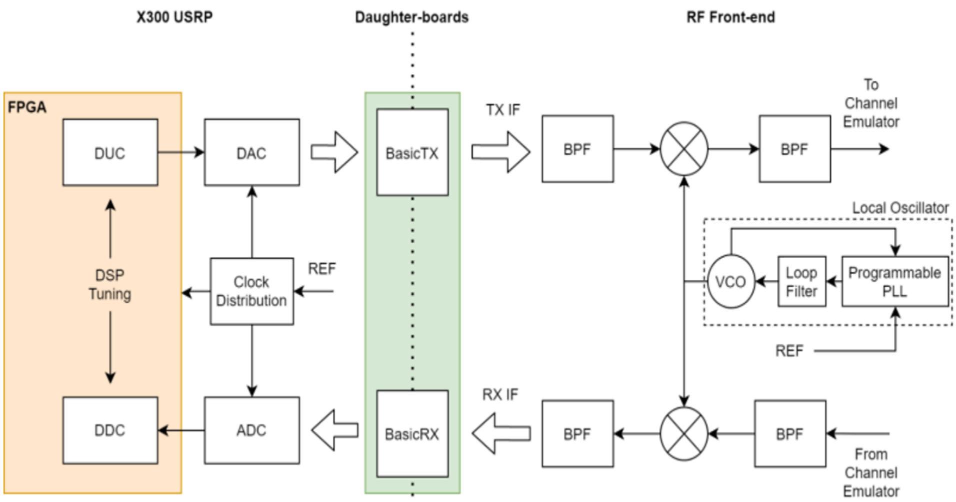

Figure 3.5: MSC's Hardware Blocks

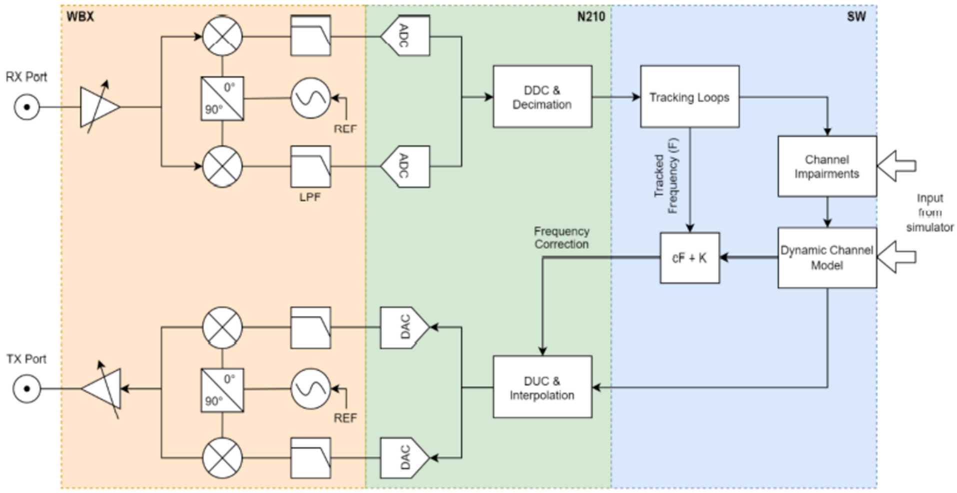

Figure 3.6: DSC's Hardware Blocks

3.2 Channel Emulation

Channel emulation will be fundamental to bring the laboratory operative conditions as similar as possible to the ones of the real case scenario. Since in the testbed the signal will travel either through a few centimeters cable or through a few centimeters wireless link it is important to impair such signal with realistic channel effects. The behavior of the DSC shall be included in the channel emulation, in particular for what concerns the coherent retransmission according to the standardized turnaround ratio for uplink and downlink in S-band that, as for the module 201 Rev. B of [5], is 240/221. Both static and dynamic channel impairments should be considered in the channel emulator, which are:

- Static delay, static doppler, static attenuation and static AWGN
- Dynamic delay, dynamic doppler rate and doppler acceleration and dynamic attenuation

All the RF signal processing will be interfaced to the USRP N210 through the provided drivers.

3.2.1 Variable Attenuation

Attenuation in the Mars orbital environment is expected to be dominated by the Free Space Loss (FSL).

$$FSL = \left(\frac{4\pi d}{\lambda}\right)^2$$

A graph with the relative ranges between the satellites of the constellation has been derived from the orbital predictions and reported in Figure 3.7.

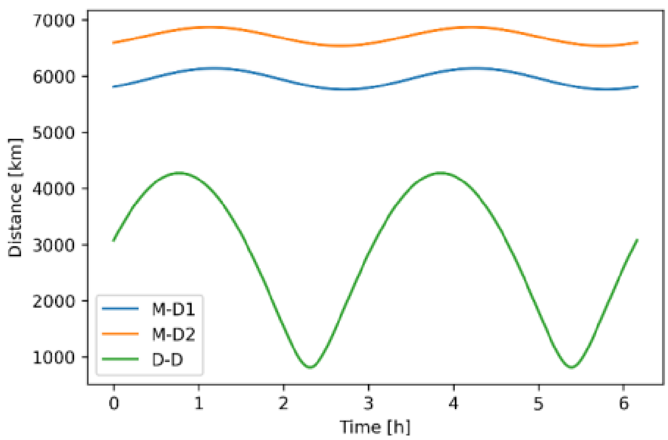

Figure 3.7: Relative Ranges between the MSC and DSCs

From the link budget study for the ISL, which was considering 2 W of transmitted power at X-band (7.2 and 8.4 GHz for uplink and downlink), the total FSL for the maximum slant range of 7000 km was $\sim$ 188 dB (@ 8.4 GHz). This, accounting also Tx/Rx antenna gains and circuitry loss, was able to provide a high-enough P_c/N_o of 32 dB-Hz. At the same maximum distance, for an S-band link (2.1 GHz and 2.3 GHz for uplink and downlink) the expected FSL attenuation would be reduced and approximately $\sim$176 dB (@ 2.3 GHz).

Considering also the minimum distance between the mother node and any of the daughter nodes of 5800 km the attenuation profile over time would range between:

- 186.4 - 188.1 dB for X-band
- 175.2 - 176.8 dB for S-band

Therefore, the emulation of the attenuation over time should reflect the sinusoidal behavior of the relative ranges shown in Figure 3.7, oscillating between the identified lower and upper bounds, hence with the magnitude of such variation limited to 2 dB . Digital simulation of FSL can be achieved by simply multiplying the data bearing signal (the complex baseband digital envelope) by a time-varying constant.

3.2.2 Delay

Considering the operative range limits described in the previous section we expect the RTLT delays of an Inter Satellite Link to be in the order of tens of milliseconds.

- At the maximum distance of 7000 km -> round trip distance of 14000 km -> RTLT of 46.7 ms
- At the minimum distance of 5800 km -> round trip distance of 11600 km -> RTLT of 38.7 ms

Simulating such delays could be accomplished by a FIFO queue (Figure 3.8) in the USRP N210 (emulating the daughter node). It could

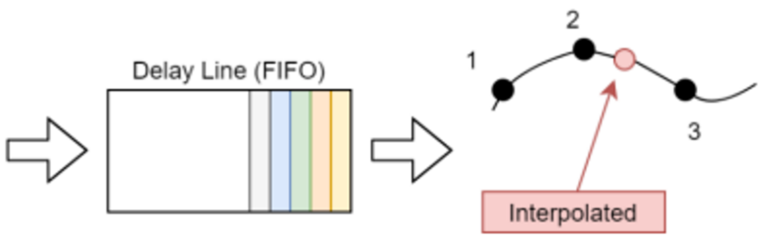

Figure 3.8: FIFO queue for delay emulation

be possible, in fact, to simply store the IQ samples of the regenerated RF signal and “forward” them after the desired delay. Assuming a generous sampling rate of 20 Msample/s and a quantization resolution of 16 bits for both the in-phase and in-quadrature samples (thus 32 bits per sample overall) we need 20000 samples and 640 kbit per millisecond leading to a total required memory of 29,89 Mbit of RAM (3.73 MB) for the worst case. Interpolation could be performed if an "extracting rate" equal to a fraction of the sampling rate is needed.

3.2.3 Doppler

The doppler effect occurs any time that a wave-like physical quantity propagates between two endpoints among which exists a relative velocity in the direction of propagation of such quantity. Being it air pressure or an electromagnetic wave, if the two nodes exchanging it are in relative motion, the receiver will see the frequency of what has been transmitted shifted left or right (lower or higher). The amount of that shift is the so-called Doppler Shift.

Historically, the Doppler shift has been defined from the point of view of a Ground Station tracking a deep-space spacecraft and is equal to the transmitted frequency minus the received frequency divided by the turnaround ratio performed by the spacecraft. Therefore, it is a positive quantity whenever the tracked spacecraft is moving away from the observer. Also, if the speeds of the nodes exchanging information is negligible compared to the speed of propagation of the latter, then classical physics can be applied and the following holds:

- $\Delta f = \frac{\Delta v}{c} f_{tx}$ if one-way
- $\Delta f = \frac{2\Delta v}{c} f_{tx}$ if two way, assuming a turnaround ratio of 1

Doppler, in fact, can be measured in a one-way, two-way or three-way fashion although the former is less desirable and strongly susceptible of the inherent instability of the oscillator onboard the spacecraft, moreover in one-way measurements the spacecraft's transmitting frequency cannot be known precisely and must be inferred. In all three cases, the measurement is performed on the downlink channel by constantly monitoring and recording over time the phase of the received carrier since the frequency is the rate of change of the phase. The most accurate solution for measuring the doppler shift is to have the same node to transmit and receive a signal that is coherently transponded by a second far node, namely the two-way measurement. In Figure 3.9, an image taken from a JPL publication "Radiometric Tracking Techniques for Deep-Space Navigation" [9], shows a simplified doppler extraction process.

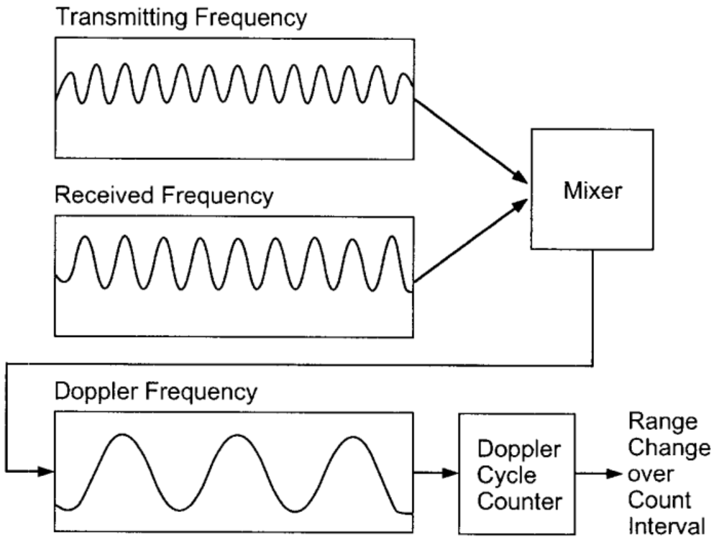

Figure 3.9: Doppler Extraction Process

As 3.9 suggests, counting the phase change of the doppler tone (obtained from mixing the reference frequency and the received one) gives a measure of the range change during one count interval. The Doppler Cycle Counter has a resolution better than one-hundredth of a cycle and *"each time the phase of the received signal slips one cycle relative to the phase of the transmitted signal, the distance over which the signal has propagated has increased by one wavelength"*[9]. This corresponds to a distance increase of 3.75 cm if using an X-band link ($\sim$ 8 GHz) and 13,6 cm in the case of an S-band ($\sim$ 2,2 GHz) link. It also might be noticed that, since doppler depends on the frequency, the different spectral components of a signal are affected differently. In a Technology Demonstrator this fact can be neglected, as long as the signal's bandwidth is much smaller than the carrier frequency.

Since doppler is dependent on the relative speed, or relative distance's rate of change, within a channel emulation it would go hand-in-hand with the delay simulation. In Figures 3.10, 3.11, 3.12 and 3.13 are presented the predictions of the operative levels of Doppler shift and Doppler rate, extracted from the predicted speeds of the spacecrafts of the constellation and evaluated both for an X-band and for an S-band scenario.

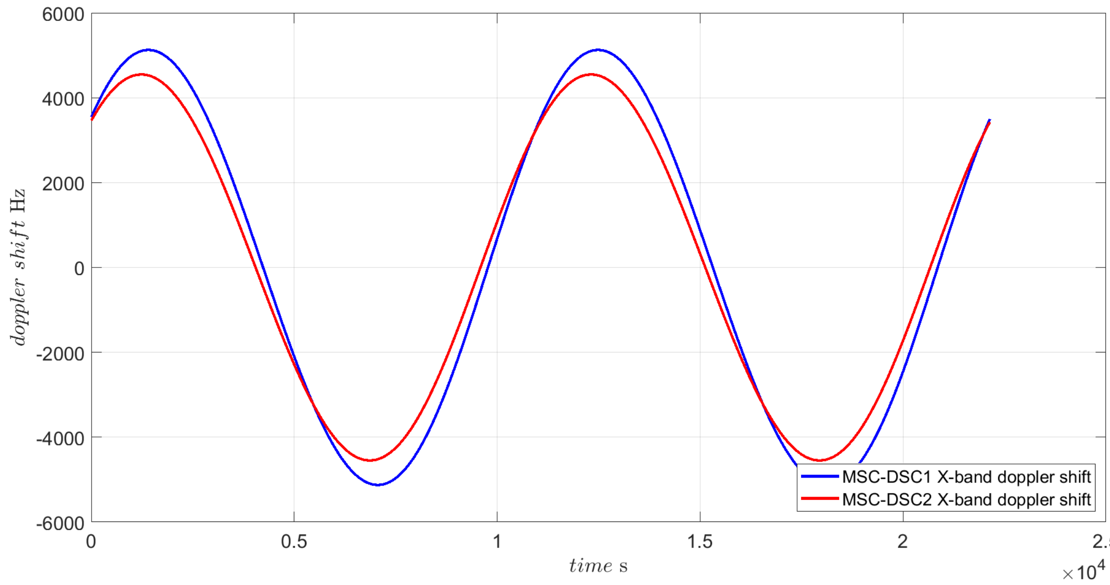

Figure 3.10: X-band Doppler Shift over time

As highlighted in the plots, satellites communicating with X-band links should expect greater frequency shifts:

- $\pm$5130Hz @ X-band
- $\pm$1495Hz @ S-band

Moreover, the incoming signal's frequency observed by the receivers will have faster rates of change in the X-band rather than the S-band case:

- $\pm 3\,{}^{\mathrm{Hz}}/_{\mathrm{s}}$ @ X-band
- $\pm 0.87\,{}^{\mathrm{Hz}}/_{\mathrm{s}}$ @ S-band

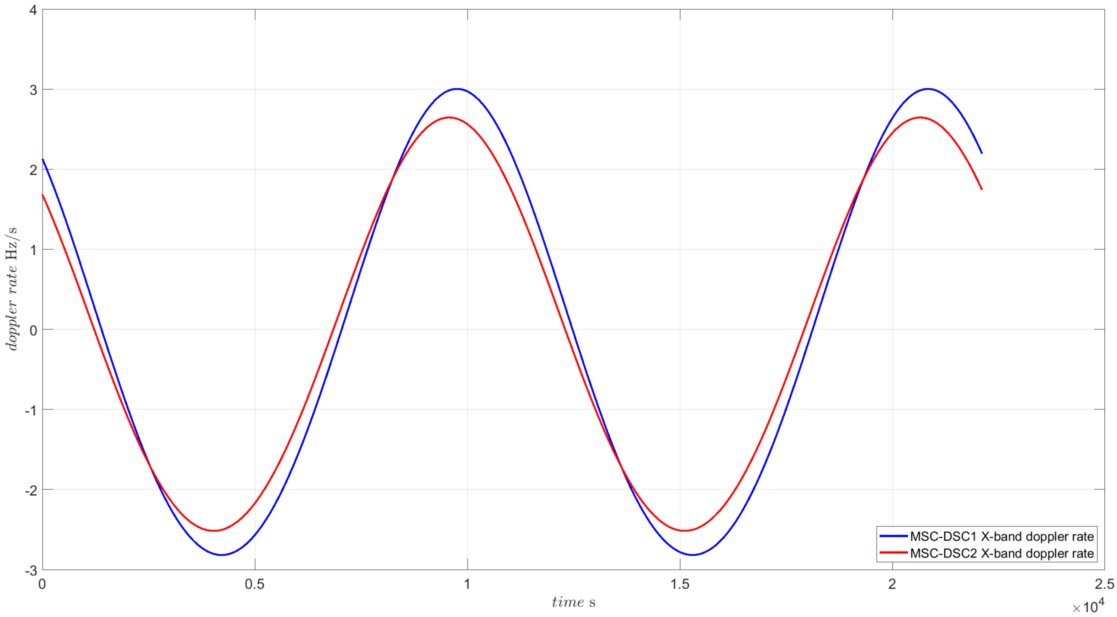

Figure 3.11: X-band Doppler Rate of change

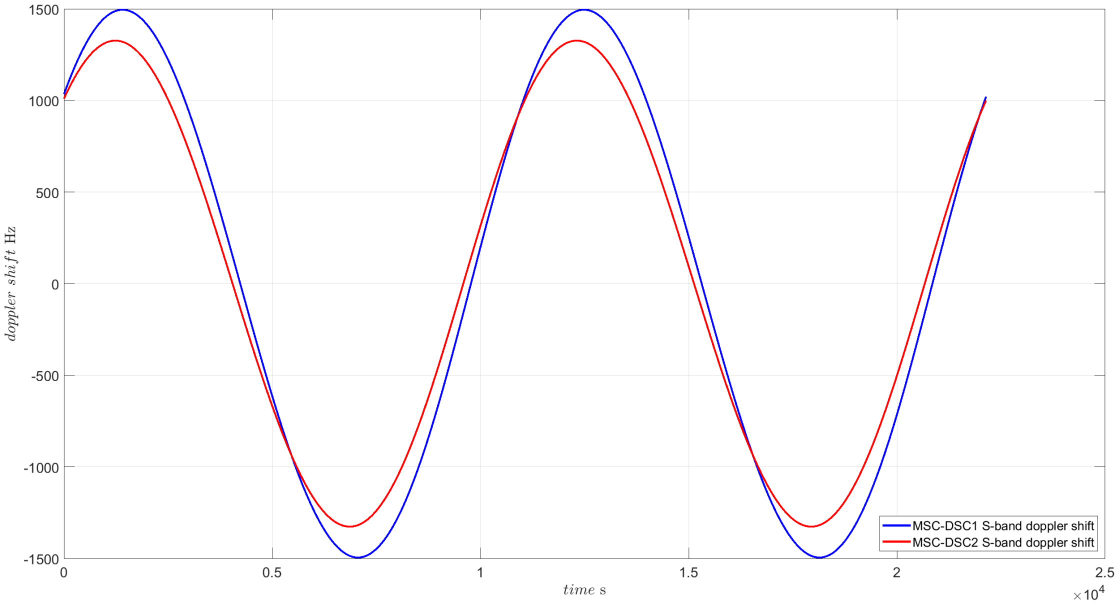

Figure 3.12: S-band Doppler Shift over time

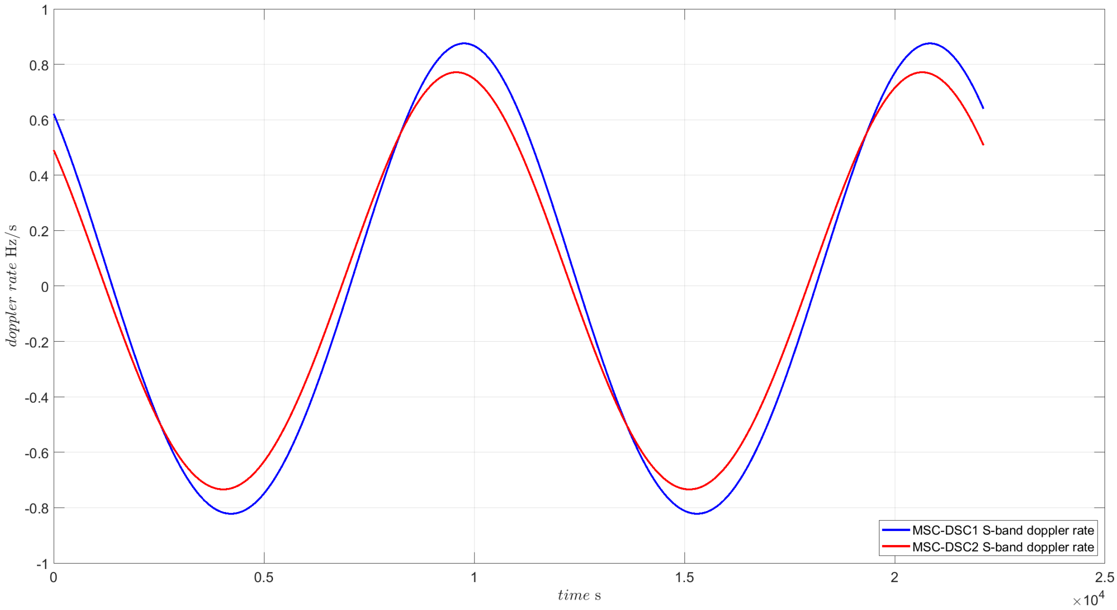

Figure 3.13: S-band Doppler Rate of change

3.2.4 Additive White Gaussian Noise

Unlike wireless terrain communications, space communications are not affected from noise sources like multipath, atmospheric perturbances, electromagnetic interference from nearby electronic devices or even intentional jamming. The main noise source is usually just the hardware of the transmitter/receiver itself. This is mainly related to the fast power transitions and power dissipation of the electronic components and usually expressed as a function of the operative temperature of the circuitry.

Thermal noise is modelled as White Noise with a two-sided power spectral density constant over all frequencies (at least below 1 THz according to the Johnson-Nyquist model) and equal to $N_o/2$ with:

$$N_o = kTF$$

k is the Boltzmann's constant (1.38e-23 J/K), T is the operative temperature of the signal's receiver and F its noise figure.

Therefore, a proper digital channel emulation can be performed by simply adding to each IQ sample a random noise value extracted from a Gaussian density function with zero mean and variance $N_o/2$ assuming $T_{sys} = 300\text{K}$ ($T_{sys} = TF$)

$$AWGN \sim N\left(0, \frac{N_o}{2}\right)$$

3.3 Range and Doppler Error Budgets

The final software block of the TD to be implemented on the USRP X300 (implementing all MSC's functions of interest) is the extraction of the radiometric observables to be forwarded to the software in charge of the autonomous orbit determination. It is worth to remind that these are relative metrics which need to be converted into absolute values (with respect to a planetocentric reference plane) with the aid of the EKF and a complete knowledge of all the accelerating forces acting on the spacecrafts of the constellation.

In the following sections theoretical examinations of the uncertanties relative to the extraction of such radiometric observables are reported.

3.3.1 Range Measurement Error Budget

Range measurements are derived by comparing timestamps of the same epoch of a PN code in transmission and in reception. By subtracting the processing time needed by the digital transponder to reply and multiplying by the speed of light we get a very precise range measure. However, in presence of thermal noise its accuracy is greatly reduced with a standard deviation of:

$$\sigma_{sine-sine} = \frac{c}{4\pi f_{rc}}\sqrt{\frac{2B_l N_o}{P_R}}$$

Where:

- c — the speed of light
- f_{rc} — the code's range clock (1.5 MHz for a 3Mcps code)
- $\frac{P_R}{N_o}$ — the signal's SNR
- B_l — the loop bandwidth of the MSC

Setting B_l to 1 Hz and considering the expected SNR to be 32 dB-Hz the accuracy would be $\sim$ 2 m with the possibility to reach $\sim$ 30 cm by integrating for 60 s. Other critical factor that can degrade the accuracy of range (and doppler) measurements is the clock instability of the MSC. According to [9] the clock instability determines an uncertainty in the range measure of:

$$\Delta range = \sqrt{2} c \tau \sigma_y(t)$$

Where τ is the RTLT and $\sigma_y(t)$ is the USO's ADEV evaluated in $t = \tau$. Ultimately also the solar plasma can strongly affect range measurements. This could be however overcome by using higher frequencies or by using multiple links in different frequency bands as cited by [9]:

"For example, solar plasma delays exceeding 200 m in S-band Viking Lander range measurements were calibrated to about 8-m accuracy using dual S and X downlinks from the Viking orbiters [86,87]. Today, spacecraft operate primarily with an X-band uplink and downlink. Plasma effects for an X-band two-way link are reduced by a factor of 13 when compared to an S-band link."

Finally, the same reference document also suggests:

"It should also be pointed out that range data, if continuously acquired, have a time signature similar to those for Doppler and provide spacecraft angular information as well as geocentric range and range rate. In fact, several days of continuous, biased range data with an accuracy of 1 m have the same angular information as a comparable track of Doppler with an accuracy of 0.1 mm/s."

3.3.2 Doppler Measurement Error Budget

This section will report the measurement error that occur when tracking the doppler shift of an incoming signal due to operative conditions of the transmitter and the receiver (such as the experienced SNR, the thermal noise of the circuitries, the carrier loops' bandwidth and the oscillators instabilities) and due to the effects of the solar scintillations that may cause charged plasma to get trapped in the propagating electromagnetic wave.

Remembering that:

- $\Delta f = \frac{\Delta v}{c} f_{tx}$ if one-way
- $\Delta f = \frac{2\Delta v}{c} f_{tx}$ if two-way, supposing turnaround ratio 1

the errors that, on average, an observer would face in computing the speed of the relative motion between himself and the remote signal source of interest will be evaluated. The discussion of such errors follows the guidelines of the DSN Telecommunications Link Design Handbook [5] and all measurement uncertainties are characterized with their standard deviations or variances. The described errors are referring to the final range-rate measure extracted, hence they are expressed in $\frac{\mathrm{m}}{\mathrm{s}}$. However, it is possible to pass between an error in velocity to an error in frequency simply by applying:

- $\sigma_f = \frac{f_c}{c} \sigma_v$ if one-way
- $\sigma_f = \frac{2f_c}{c} \sigma_v$ if two (or three)-way

where f_c is the downlink carrier frequency.

From the same reference handbook [5] are reported the block schemes highlighting the doppler extraction process performed at a Deep Space Station (DSS) in the cases of one-way and two-way links (Figure 3.14 and 3.15).

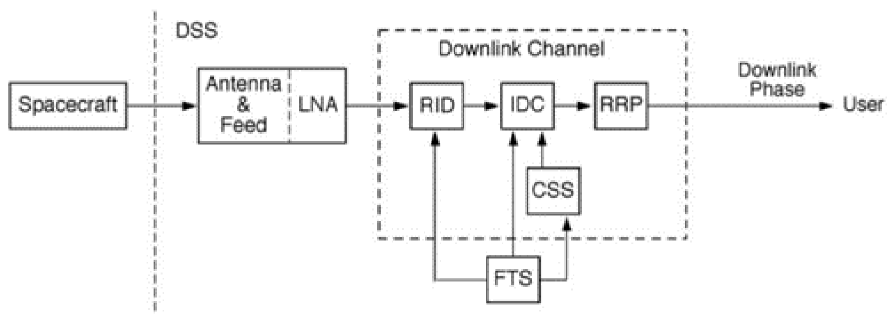

Figure 3.14: One-Way Doppler Measurement at DSS

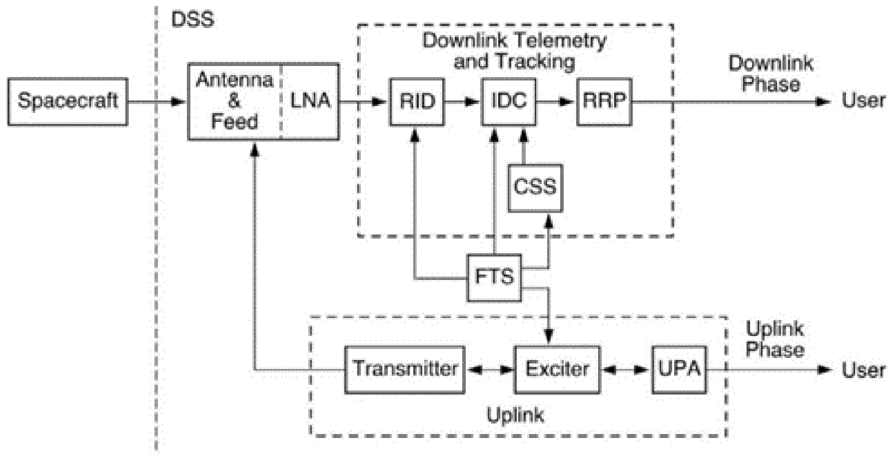

Figure 3.15: Two-Way Doppler Measurement at DSS

where

- LNA is the Low Noise Amplifier
- RID is the RF to IF Downconverter
- IDC is the Intermediate to Digital Converter
- RRP is the Receiver and Ranging Processor
- CSS is the Channel Select Sythesizer
- FTS is the Frequency and Timing Subsystem
- UPA is the Uplink Processor Assembly

Whether we consider a one-way or two-way measure, doppler measurements are mainly affected by three contributing factors: thermal noise, carrier phase noise and solar scintillation.

$$\sigma_V^2 = \sigma_{VN}^2 + \sigma_{VF}^2 + \sigma_{VS}^2$$

where:

- σ_V^2 doppler measurement variance

- σ^2_{VN} contribution due to thermal noise
- σ^2_{VF} contribution due to oscillators' phase noise
- σ^2_{VS} contribution due to solar phase scintillation

Moreover, when using phase shift keying modulations such as BPSK or QPSK, an imbalance in the number of logical ones or zeros in the modulated data would add phase jitter to the carrier tracking loop, hence constituting another contribution to the doppler measurement variance. Pseudo randomization of the modulated data can however easily overcome this problem by balancing the number of 0s and 1s. In the studied signal for the ARES4SC project this balancing comes as a natural benefit from the adoption of a balanced pseudo random code as spread spectrum sequence for the CDMA scheme.

Thermal Noise

Thermal noise can be treated as white noise, spanning virtually across all the frequency spectrum with equal intensity. The contribution (σ^2_{VN}) it provides to the overall doppler measurement variance can be modelled as:

$$\sigma^2_{VN} = 2 \cdot \left(\frac{c}{2\pi f_C T}\right)^2 \cdot \frac{1}{\rho_L} \quad if\ one-way$$

$$\sigma^2_{VN} = \sigma^2_{VNU_{plink}} + \sigma^2_{VND_{ownlink}} \quad if\ two-way$$

where:

- $\sigma^2_{VNU_{plink}} = \frac{1}{2} \cdot \left(\frac{c}{2\pi f_C T}\right)^2 \cdot \frac{G^2}{\rho_{TR}} \cdot \frac{B_L}{B_{TR}}$
- $\sigma^2_{VND_{ownlink}} = \frac{1}{2} \cdot \left(\frac{c}{2\pi f_C T}\right)^2 \cdot \frac{1}{\rho_L}$

In particular:

- T is the integration time [s]
- f_C is the downlink carrier frequency [Hz]

- c is the speed of light
- G is the turnaround ratio
- B_L one-sided, noise-equivalent, loop bandwidth of downlink carrier loop [Hz]
- B_{TR} one-sided, noise-equivalent bandwidth of the transponder's carrier loop [Hz]
- ρ_L is the downlink carrier loop signal to noise ratio

Behind this formula there is though the assumption of a carrier loop bandwidth in the DSC much larger than the one for the Carrier Tracking Loop (CTL) in the MSC. Concerning the CTL, a Costas Loop has been chosen to track the UQPSK-modulated signal due to its excellent sensitivity, double with respect to other PLL detectors. Its loop error voltage is, in fact, proportional to $sin(2(\theta_{in} - \theta_{ref}))$ instead of the classical $sin(\theta_{in} - \theta_{ref})$. This makes the Costas Loop well suited for tracking Doppler-shifted carriers[10].

Concerning the carrier loop signal to noise ratio ρ_L, when tracking a phase-modulated carrier such the one adopted in the ISL, it is defined as:

$$\rho_L = \frac{P_T}{N_o}|_{\frac{D}{L}} \frac{S_{LQ}}{B_L}$$

where:

- $\frac{P_T}{N_o}|_{\frac{D}{L}}$ is the signal power to noise spectral density [Hz]
- B_L is the one-sided, noise-equivalent, loop bandwidth of the downlink carrier loop [Hz]
- S_{LQ} is the squaring loss of the QPSK Costas Loop which is defined as:

$$S_{LQ} = \frac{1}{1 + \frac{9}{\frac{2E_{SQ}}{N_o}} + \frac{6}{\left(\frac{E_{SQ}}{N_o}\right)^2} + \frac{3}{2\left(\frac{E_{SQ}}{N_o}\right)^3}}$$

- $\frac{E_{SQ}}{N_o}$ is the energy per quaternary channel symbol to noise spectral density ratio [Hz]

Phase Noise

For one-way Doppler measurements the main factor contributing in an erroneous estimate is the frequency source of the spacecraft. The latter, in fact, introduces two kind of errors: an unknown bias in the effectively transmitted frequency and a random error due to the frequency instability of the oscillator on-board. Such instability can be expressed either in terms of phase noise or in terms of allan deviation (see **Chapter 6** for more details). Instead, for a two-way doppler measurement the bias in the exact frequency of the signal is no more present and only the frequency instabilities of the oscillator at the Deep Space Station are playing a role. Among others, one parameter that determines the error in the doppler shift computation is the bandwidth B_L of the carrier tracking loop of the ground station receiving the signal. Assuming the latter large enough to pass all the low-pass power spectral density of the spacecraft transponder's phase noise, the phase noise contributions can be approximated as:

$$\sigma_{VF} \approx c\sigma_y(T) \quad if\ one - way$$

$$\sigma_{VF} \approx \frac{c\sigma_y(T)}{\sqrt{2}} \quad if\ two - way$$

As depicted by the above equations, the error's standard deviation for a two-way coherent link mainly depends on the Allan Deviation of the oscillator at the ground station with a factor $\frac{1}{\sqrt{2}}$ (which translates to a factor 2 if considering the variances instead of standard deviations) to distinguish the two-way case from the one-way. The Allan Deviation should be evaluated in the Doppler measurement time T = RTLT.

Usually, when performing a two-way coherent tracking with a deep-space spacecraft the phase noise of the frequency provided in uplink by the FTS is uncorrelated with the phase noise of the same frequency source at the station due to the large round trip light time. However, it is interesting to investigate what happens when such RTLT is short as in the case of the ARES4SC study. In fact, the relatively short slant ranges between the communicating spacecrafts of the constellation (with a RTLT below 50 ms) implies a strong USO's noise suppression since an instability that occurs at time scales larger than the RTLT is almost canceled [11]. For this suppression is fundamental, of course, to use the same frequency reference both for transmission and reception of the signal. The instability of the relative frequency shift $y(t) = \frac{\delta f}{f}$ between the reference frequency and the received signal's frequency can be modeled taking in consideration that the clock noise transfer function consists in two anticorrelated delta functions separated in time by a RTLT.

$$y(t) = y_c\delta(t - RTLT) - y_c\delta(t)$$

Figure 3.16 visually shows the noise cancellation process. The blue bell-shaped curves represent the USO's frequency instability of duration T. The red arrows show, instead, the clock noise transfer function with the two anti-correlated delta functions separated by $\frac{2L}{c}$ where L is the ISL slant range.

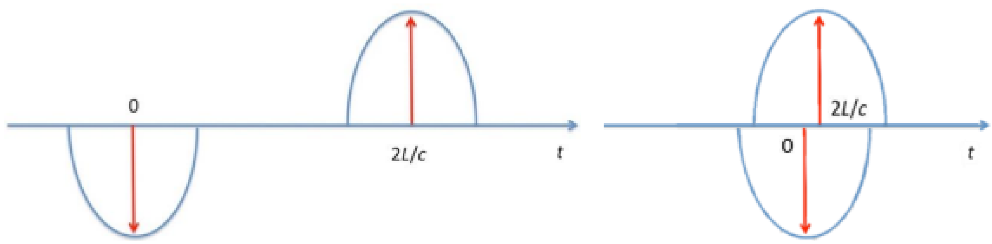

Figure 3.16: Noise cancellation process, visual representation

When the RTLT >> T the error due to instability happens twice (left side of the figure) while on the right we can see how having a short RTLT allows for the cancellation of such instability, thus suppressing the USO's noise.

Solar Scintillation

Despite being irrelevant for the ARES4SC mission since the ISL will travel nowhere near the Sun it is worth mentioning this modeled and well-known impairment.

Whenever the electromagnetic wave to/from a spacecraft passes through the solar corona, plasma interacts with it and the charged particles cause phase scintillations in the data bearing signal. The main factors involved are the Sun-Earth-Probe angle θ_{SEP}, the carrier frequency f_c, the light speed c and the measurement integration time T.

For $0^o < \theta_{SEP} \leq 90^o$:

$$\sigma_{VS}^2 = \frac{2.13 C_{band} c^2}{f_c^2 T^{0.35} [sin(\theta_{SEP})]^{2.45}} \quad if\ one - way$$

$$\sigma_{VS}^2 = \frac{0.53 C_{band} c^2}{f_c^2 T^{0.35} [sin(\theta_{SEP})]^{2.45}} \quad if\ two - way$$

For $90^o < \theta_{SEP} \leq 180^o$:

$$\sigma_{VS}^2 = \frac{2.13 C_{band} c^2}{f_c^2 T^{0.35}} \quad if\ one - way$$

$$\sigma_{VS}^2 = \frac{0.53 C_{band} c^2}{f_c^2 T^{0.35}} \quad if\ two - way$$

where C_{band} is a band-dependent parameter which for the X-band equals to $2.7 \cdot 10^{-6}$.

Chapter 4

CCSDS Recommendations

This chapter will depict the state-of-the-art guidelines that have been taken as reference for the subsequent development of the digital signal processing stages needed to transmit, receive and track the range-bearing signal of the Inter Satellite Link under study.

Before any software development a research phase was needed to understand the critical parameters and the fundamental requirements in order to perform the radiometric observables extraction in the foreseen operative environment for the ARES4SC mission.

As previously mentioned, the ISL is the primary resource for the constellation in order to be able to retrieve the precise orbital state vector of the constituent satellites. The Mother SpaceCraft will be continuously communicating with the 4 DSC adopting a CDMA scheme in order to share the same portion of the spectrum. In the Technology Demonstrator the forward link is planned to be centered within 2025-2120 MHz and occupied by the sole central node. The return link falls into the 2200-2300 MHz frequency range and is shared by all the daughter crafts which simultaneously retransmit the signal received from the mothercraft in a coherent way for what concerns both the carrier and the PN code. What being coherent with respect to the PN code means will be clear later. The latter, in particular, is the key enabler element to perform ranging measurement and user (daughter nodes) multiple access. Given the fitting scenario, a Consultative Committee for Space Data Systems (CCSDS) Recommended Standard has been taken as a reference for the spread spectrum signal generation. It consists of the blue book [7] and the green book [8] for *"Data Transmission and PN Ranging for 2 GHz CDMA Link Via Data Relay Satellite"*. The aforementioned books relate to a scenario which is slightly different from the required one. In fact, if we consider only the SmallSat constellation system (thus ignoring possible data forwarding to the DSC coming from the link with Earth), we have no satellite acting as data relay however the CDMA spread spectrum modulation schemes described are fully compatible with our ranging needs. Moreover, the architecture suggested by the CCSDS recommendation highlights the possibility of implementing low-rate data transmission along with the ranging services. This should come as a natural benefit of the modulation structure without compromising the ranging capabilities of the system and it will be subject to further laboratory investigations.

4.1 CDMA Scheme and Spread Spectrum

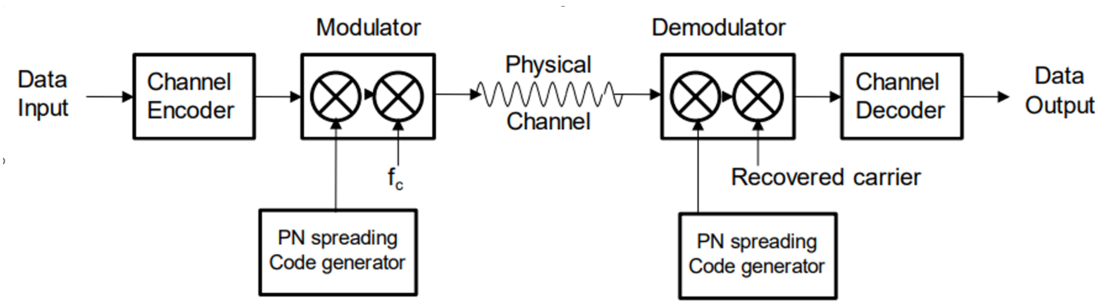

Figure 4.1: Basic Spread Spectrum Modulation Scheme (from [8])

The main idea behind spreading the RF bandwidth of the desired signal to be transmitted is to have a much lower (even below the noise floor) Power Spectral Density and, choosing the appropriate spreading codes, to limit the Multiple Access Interference (MAI) coming from other users transmitting in the very same frequency band with other spreading codes. Moreover, even if this might not be relevant around the Mars orbit environment, spreading the data signal spectrum makes the communication resilient to jamming or, in general, to narrow-band interference. The spreading and de-spreading process is shown in Figure 4.1 and 4.2 with simplified drawings taken from the CCSDS Green book [8]. At the receiver side the signal is correlated with an in-phase

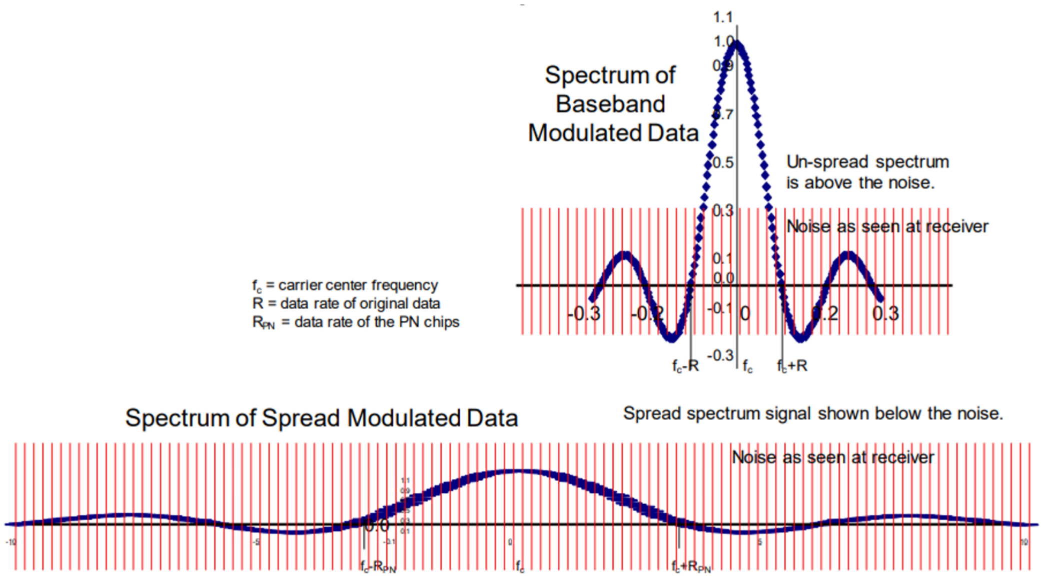

Figure 4.2: Un-Spread vs. Spread Data Bandwidth (from [8])

replica of the same spreading code that was used by the transmitter, consequently having that the original low-datarate signal turns back to its narrow bandwidth occupancy and any possible interfering signal spreads in frequency and fades below noise floor (Figure 4.3)

Of major interest for the mission scope was understanding which spreading code to use and which properties it should satisfy in order to allow a proper multiple access between the DSCs and a proper ranging measurement extraction. There are different spreading code families available for DSSS systems and all exhibit properties similar to those of pure random sequences, hence the name of Pseudo Random (PN) sequences since they are not truly random and, moreover, they are deterministic. The PN sequences to use mainly depend on whether the chip stream is synchronous with the data stream or not: in systems like UMTS where the data and the spreading stream are synchronous

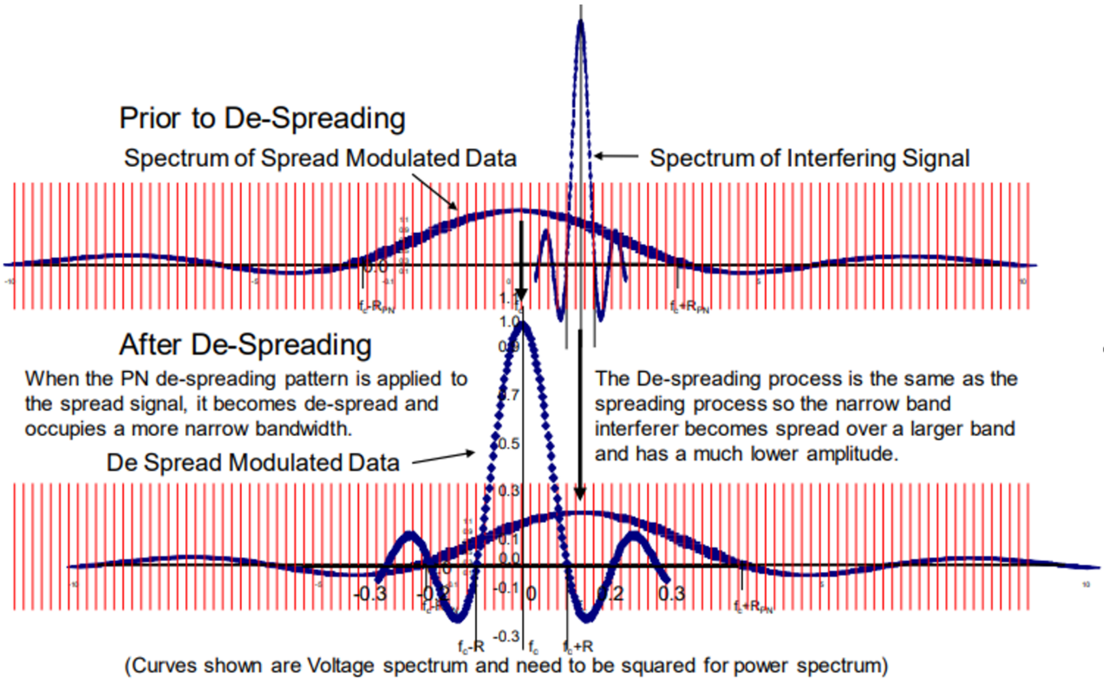

Figure 4.3: Receiver De-Spreading Process (from [8])

and one data bit equals one period of the spreading sequence the code type of choice is the Walsh code family which shows completely orthogonal cross-correlation properties. In the CCSDS recommendation instead a complete orthogonality is not required as the data stream is transmitted asynchronously with respect to the spreading chips. Not fully orthogonal codes which maintain very low cross-correlation are Gold codes and Maximal-length sequences. Both can be hardware-generated through Linear Feedback Shift Registers and have been subject of analysis in further sections of this chapter. In Figure 4.4, taken as well from the CCSDS Green reference book [8] it is shown the principle of asynchronous mixing between the PN pattern and the data stream. Figure 4.5 instead reports the corresponding demodulation process.

Typical parameter used to describe Spread Spectrum Systems is the Spreading Factor, which is a measure of how much the bandwidth of the TX RF signal has been expanded with respect to its original form

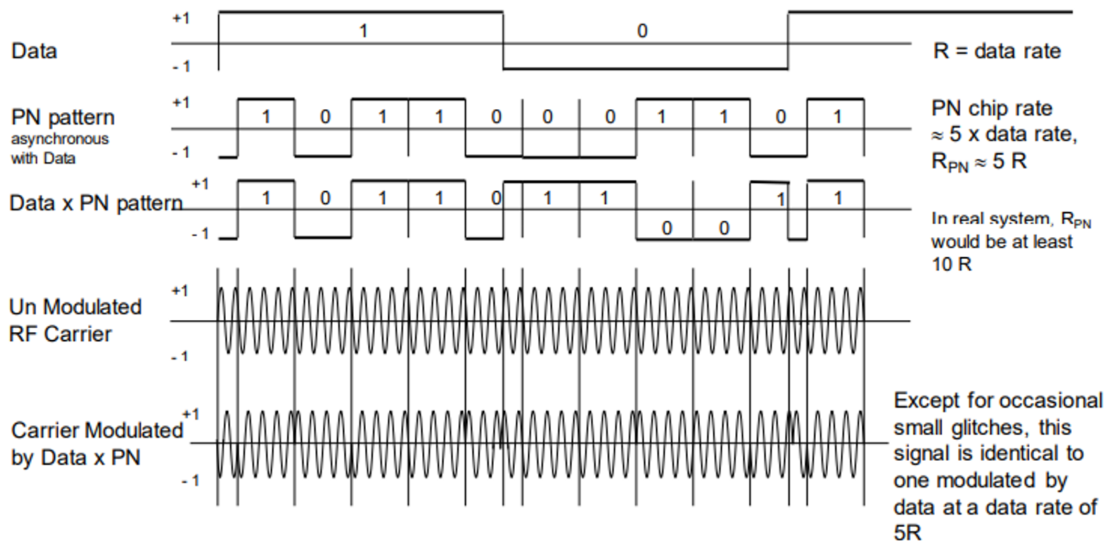

Figure 4.4: Spread Spectrum Modulation (from [8])

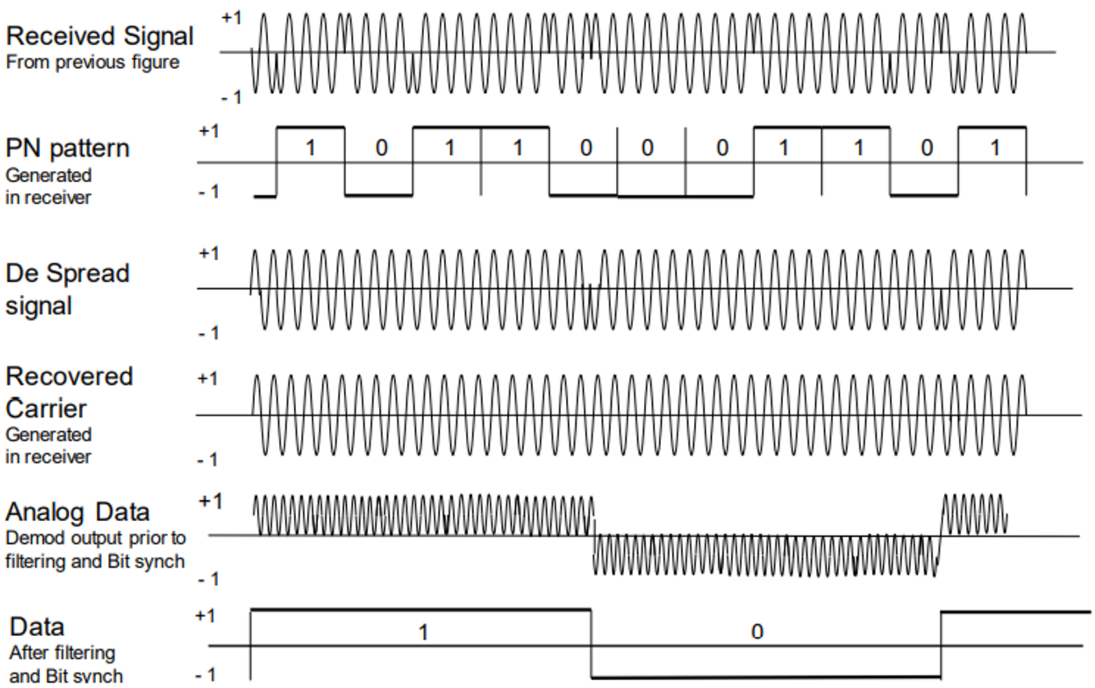

Figure 4.5: Spread Spectrum Demodulation (from [8])

and is expressed as:

$$SF = \frac{BW_{tx}}{BW_{baseband}} \approx \frac{R_{PN}}{R_{DATA}}$$

CCSDS recommendations suggest that the SF shall be approximately 10 and, in general, it is desirable to have the highest SF possible under the bandwidth constraints of our system. As the reader might notice, in the receiver demodulation process depicted in Figure 4.5 the de-spreading process comes before the carrier demodulation, hence there isn't a specular reversed order with respect to the modulation process. This is due to the fact that the link over which we are transmitting has to be designed to sustain the useful coded data rate and not the 10 times higher chip rate of the spreading sequence. Therefore, we have that:

$$\frac{E_c}{N_o} \ll \frac{E_b}{N_o}$$

where E_c refers to the energy per chip while E_b refers to the energy per bit. In particular, the SNR will be from 10 to a huge 30 dB below the data SNR and the expected chip error rate would be close to 50%. It is therefore suggested to perform PN de-spreading before carrier demodulation. In a digital domain, multiple correlators should be running in parallel to quickly achieve chip synchronization by cross-correlating the incoming signal with different phase shifts of a local replica of the spreading code.

From CCSDS [8]: *"As an example of why a correlator is used rather than a direct chip comparison between the received chip values and the internally generated PN pattern chip values, a 1 kb/s forward data rate can be considered, where the channel is operating near threshold. The SNR (the $\frac{E_c}{N_o}$) for the range channel will be much lower than the SNR of the 1 kb/s command data channel. It will be 10 dB less because of the lower power* (as it will be stated later, the suggested modulation foresees an unbalance ratio of 10:1 between the spread data stream on the I branch and the ranging sequence stream on the Q branch) *and it will be another (3 Mcps / 1 kbps = 3000) 34.8 dB less because of the higher chip rate. Individual chip values (0 or 1) cannot be identified at such a low SNR, requiring a correlation process to be used."*

As it will be discussed later, the acquisition time (and consequently the sequence length) is one of the fundamental quality measures for a PN sequence, along with its spectral properties.

One critical aspect to consider is the power management of the signals to be de-spread. Particular attention, in fact, must be given to avoid transmitting a signal with much more power than expected by the receiver since the de-spreading process is susceptible of false lock: a well-known issue for DSSS systems, also known as "near-far" problem. Specifically, as the receiver requires a PN lock detection signal before correctly demodulating the carrier to generate bits, it may happen that a peak voltage in the received signal will induce a false lock in the receiver circuitry. This is due to the fact that the receiver's correlator generally implements a serial search over all the possible shifts of the sequence and the correlation peak will determine the phase position of the received periodic sequence. However, this maximum search strategy is not sufficiently robust since it may declare lock even if there is no incoming signal or if the ranging channel is active but no ranging signal is actually transmitted over it. For this reason, more reliable implementations usually foresee a threshold comparison approach. Such threshold needs careful calibration to avoid to false lock to a signal stronger than expected. This idea is depicted in Figure 4.6. However, in a digital domain, we could tune an Automatic Gain Control (AGC) block in order to bring the received signal's power to a suitable reference level allowing to expect a correlation value, normalized by the sequence length, of 1, thus avoiding the false lock problem.

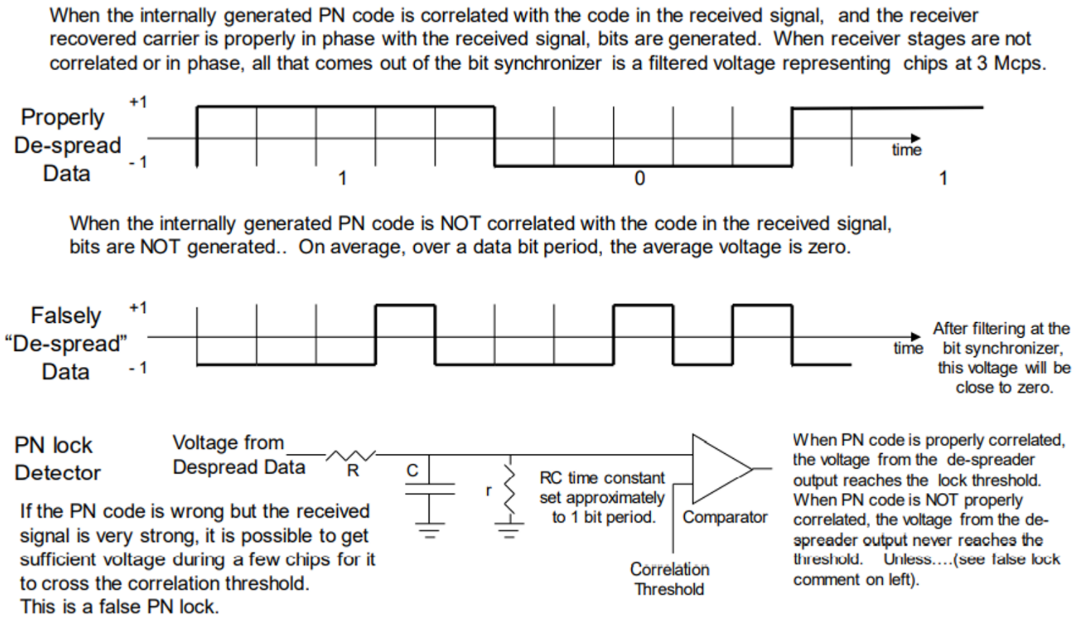

Figure 4.6: Correct lock vs. False lock (from [8])

4.2 Forward Link

In this section the modulator architecture for the forward link as well as the properties of the spreading codes to be used are described. From [8], in Figure 4.7 a model of the suggested TX architecture for the MSC is shown along with the proper "matched" architecture for the receiver (Figure 4.8). As highlighted by the transmitting architecture scheme, the I channel is dedicated to a low-datarate transmission and is referred to as the Command channel, while the Q channel is to be used only for a long (261888 chips) ranging sequence transmission without any spreading of a baseband digital data signal. The spreading process happens in the I channel only, between the data stream and a shorter (1023 chips) spreading sequence. The PN code for the forward I channel shall meet the requirements in Table 4.1.

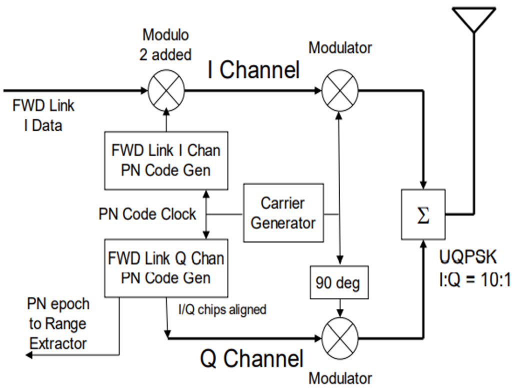

Figure 4.7: MSC transmitter (from [8])

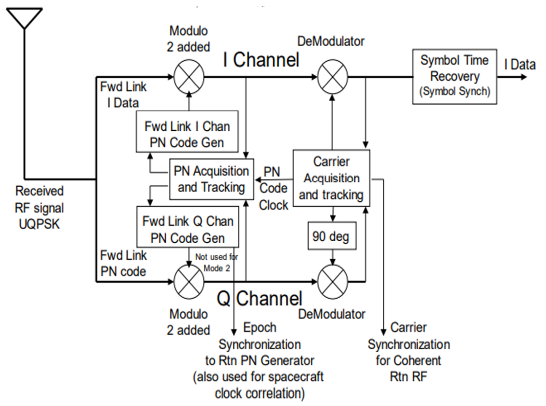

Figure 4.8: DSC receiver (from [8])

Table 4.1: I channel Gold Code properties

Property	Value
Tx Carrier Frequency	2025-2120 MHz in accordance with SFCG recommendations for Mars Orbit
Carrier Suppression	30 dB minimum
PN code family	Gold Codes
PN code length	$2^{10} - 1$ (generated with two 10-stages LFSRs)
PN code chip rate	$f_{tx} \cdot \frac{31}{221 \cdot 96}$ (≈ 3 Mcps)

Property	Value
PN code modulation	Unbalanced QPSK (UQPSK). The TX power is unbalanced with 10/11 of the total power P_t for the I channel and 1/11 P_t for the Q channel. PN chips of I and Q channel are aligned.
PN code epoch reference	User's unique initial conditions
Data modulation	Modulo-2 added asynchronously (a multiplication in the analog case where we have the encoded levels $\pm$ 1)
PN chip jitter (rms)	$\leq$ 1 degree
PN chip skew deviation between I and Q channel chips (peak)	$\leq$ 0.01 chip
PN chip asymmetry (peak)	$\leq$ 0.01

Property	Value
PN chip rate error (peak) relative to absolute coherence with carrier rate	$\leq$ 0.01 chip/s at PN code chip rate

The hardware generation of the Gold Code mentioned above is obtained through two 10-stages LFSRs (Figure 4.9) with the taps being the same for all the agencies/missions since the codes shall differ only in the initial conditions of register A. Changing the intial conditions

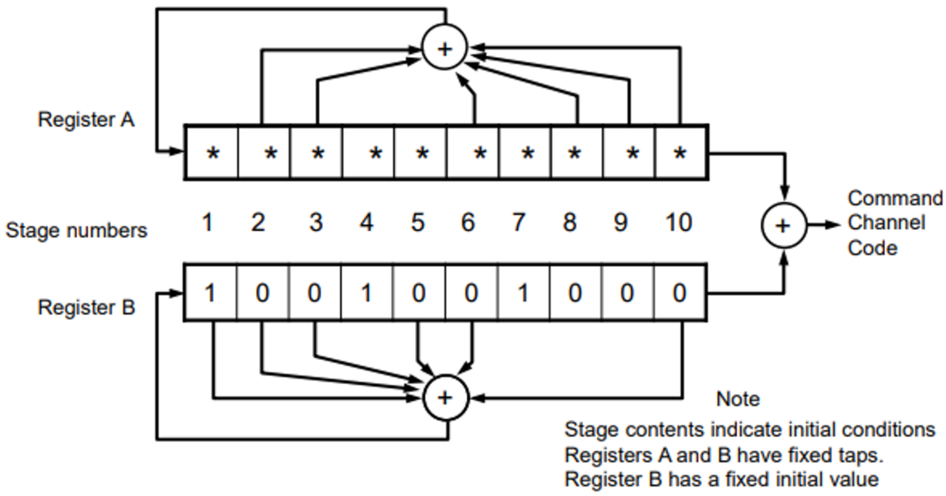

Figure 4.9: Command I Channel Gold Code Generator (from [8])

(which are unique to each agency and determine the epoch of reference for the RTLT computation), we have a total of 1024 sequences of length 1023, of which 768 are balanced (meaning that contain 512 ones and 511 zeros) and should be preferred.

On the other hand, the PN code for the forward Q channel shall meet the requirements in Table 4.2.

Table 4.2: Q channel Maximal Length Sequence properties

Property	**Value**
Tx Carrier Frequency	2025-2120 MHz in accordance with SFCG recommendations for Mars Orbit
Carrier Suppression	30 dB minimum
PN code family	Maximal Length sequence generated by a 18-stages LFSR, then truncated of its last 255 bits in order to fit 256 times the lenght of the PN I channel Gold sequence
PN code length	$2^{18} - 1 - 255 = (2^{10} - 1) \cdot 256 = 261888$
PN code chip rate	Same chip rate as on the forward I channel
PN code modulation	Unbalanced QPSK (UQPSK). The TX power is unbalanced with 10/11 of the total power P_t for the I channel and 1/11 P_t for the Q channel. PN chips of I and Q channels are aligned
PN code epoch reference	All 1's condition synchronized to the 1001001000 state of the B register for the command I channel code

The long ranging sequence for the Q forward channel can be generated with the 18-stages LFSR shown in Figure 4.10) and for which the initial condition (the all 1s condition) must be the same for all users since codes shall differ only for their feedback taps assignment. The number

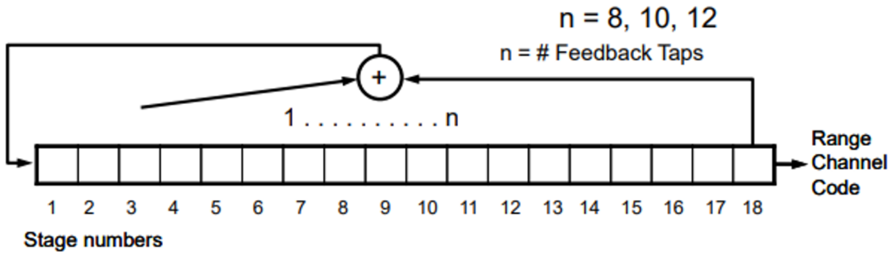

Figure 4.10: Range Q channel Range Sequence Generator (from [8])

of taps must be even. Considering 8, 10 or 12 taps a total of 1898 maximal length sequences have been identified.

4.3 Return Link

Being the target application of the ISL the two-way range and Doppler measurements along with, possibly, a return data service at rates ≤ 300 kbps there is the need of a coherent turnaround both for the received carrier frequency and for the long PN code transmitted, in uplink, on the forward Q channel. The CCSDS recommended I and Q PN codes shall be two identical Maximal Length codes separated (shifted in time) by at least 20000 chips. The latter is needed in order to reuse the same PN sequence without the risk of wrongly identifying each data channel. However, the sequence transmitted on the return I channel must be phase aligned with the sequence received in the forward Q channel. In Figure 4.11 the suggested modulator architecture of the return link transmitter is reported, aligned with the "matched" architecture for the receiver (Figure 4.12).

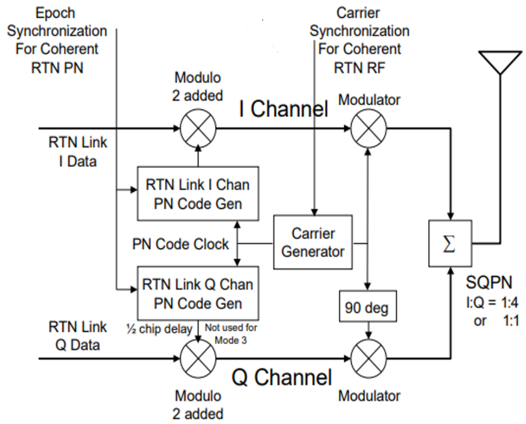

Figure 4.11: DSC transmitter (from [8])

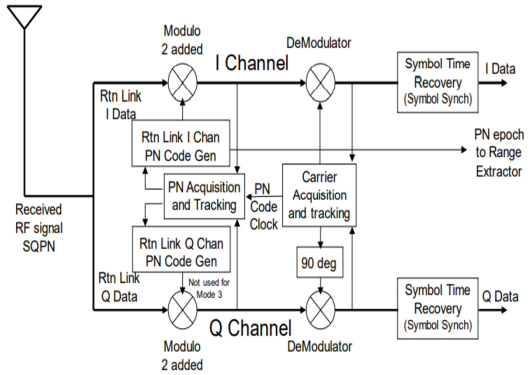

Figure 4.12: MSC receiver (from [8])

4.4 Codes Acquisition

The suggested codes are designed to ease the life of the receiver which has to acquire the spread-spectrum signal.
Acquiring the incoming PSK-modulated signal requires frequency and phase locking not only of the locally generated carrier but also of the local replica of the spreading sequence. Since, usually, the receiver has no knowledge of the incoming PN code's phase, it has to search (cross-correlate) over the entire range of possible code shifts. For this reason, the DSC acquisition process is simplified by having to search over a short incoming code (1023 chips Gold Code received on the I channel). Once the proper correlation is obtained, it will take the DSC only 255 additional phase shifts to test before obtaining a proper phase lock also on the long ranging sequence received on the forward Q channel. This thanks to the fact of having the forward long ranging sequence whose length is an exact integer multiple (256) of the forward short Gold sequence.

A possible auxiliary precaution to simplify the receiver's acquisition process could be a continuous Doppler pre-compensation performed by the transmitter (the MSC) in order to make the signal reach the receiver as close as possible to its Best Lock Frequency (BLF) hence allowing a quick frequency lock.

Regarding the short code acquisition time, CCSDS states that whenever the received signal falls within ±1500 Hz (which, though, corresponds exactly to the maximum Doppler shift foreseen for the studied ISL @ S-band) from the BLF the receiver's transponder shall acquire the short Gold code within 20 seconds with a probability > 90%. Subsequently, by CCSDS performance requirement, the receiver must lock to the long PN code within 5 seconds from the synchronization with the short code with a probability > 95%. This shorter acquisition time is made possible by the fact that the receiver has to test only 256 cross-correlation points in this time window.

One of the main parameters to consider for ranging purposes is the ranging sequence length which consequently determines the unambiguous range. Range measurements are, in fact, obtained by keeping track of the time elapsed between the transmission of one specific PN code epoch and the reception of the same epoch coherently turned-around. After having subtracted the DSC processing time delay, a measure of the round trip range can be obtained simply by multiplying by the speed of light. For the ARES4SC mission the maximum slant range between MSC and DSC of 7000 km yields a round trip range ≤ 14000 km. The recommended PN ranging codes are 261888 chips long and, being the chip rate approximately 3 Mcps, we have the code period to last in time $\frac{261888 \text{ chips}}{3 \cdot 10^6 \text{ chips/s}} \approx 0.087$ s. Therefore, during this time the light will travel a distance of:

$$d = c \cdot t = 2.9979258 \cdot 10^8 \text{ m/s} \cdot 0.087 \text{ s} \approx 26170 \text{ km}$$

Such distance constitutes the unambiguous range for the selected PN code and it is more than enough to cover the mission's distances. Exceeding this distance would result in the PN code repeating itself for more than one period, hence raising a spatial resolution ambiguity that could, however, be resolved thanks to trajectories models. As mentioned, the processing time delay of the daughter craft must be known and considered while computing the RTLT. Following the CCSDS recommendations, the derived requirement for such delay imposes constraint on its stability and not on its duration. While analog transponders usually had a reply time in the order of 300-400 ns with a variability of $\pm$ 100 ns, the response time of digital transponders is in the order of microseconds. This longer time is perfectly allowable as long as it is fixed and with a maximum instability in the order of $\pm$ 30 ns [8].

4.5 Generic Analog Architectures

Putting together the architecture tips, a rough schematic of the transmitters/receivers involved in one ISL is presented (Figures 4.13 and 4.14), with some insights on the handling of the signals exchanged.

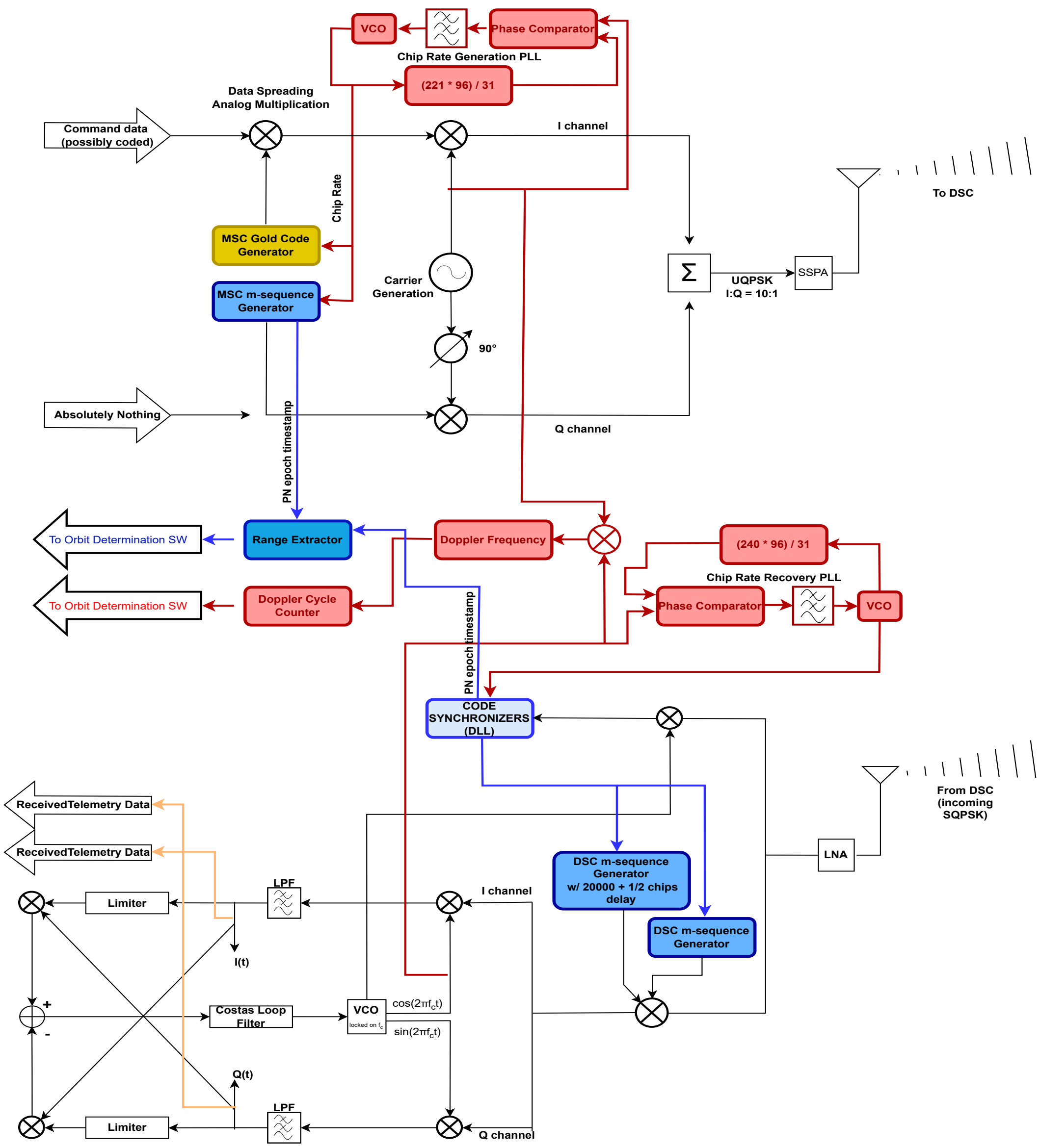

Figure 4.13: MSC Transmitter and Receiver

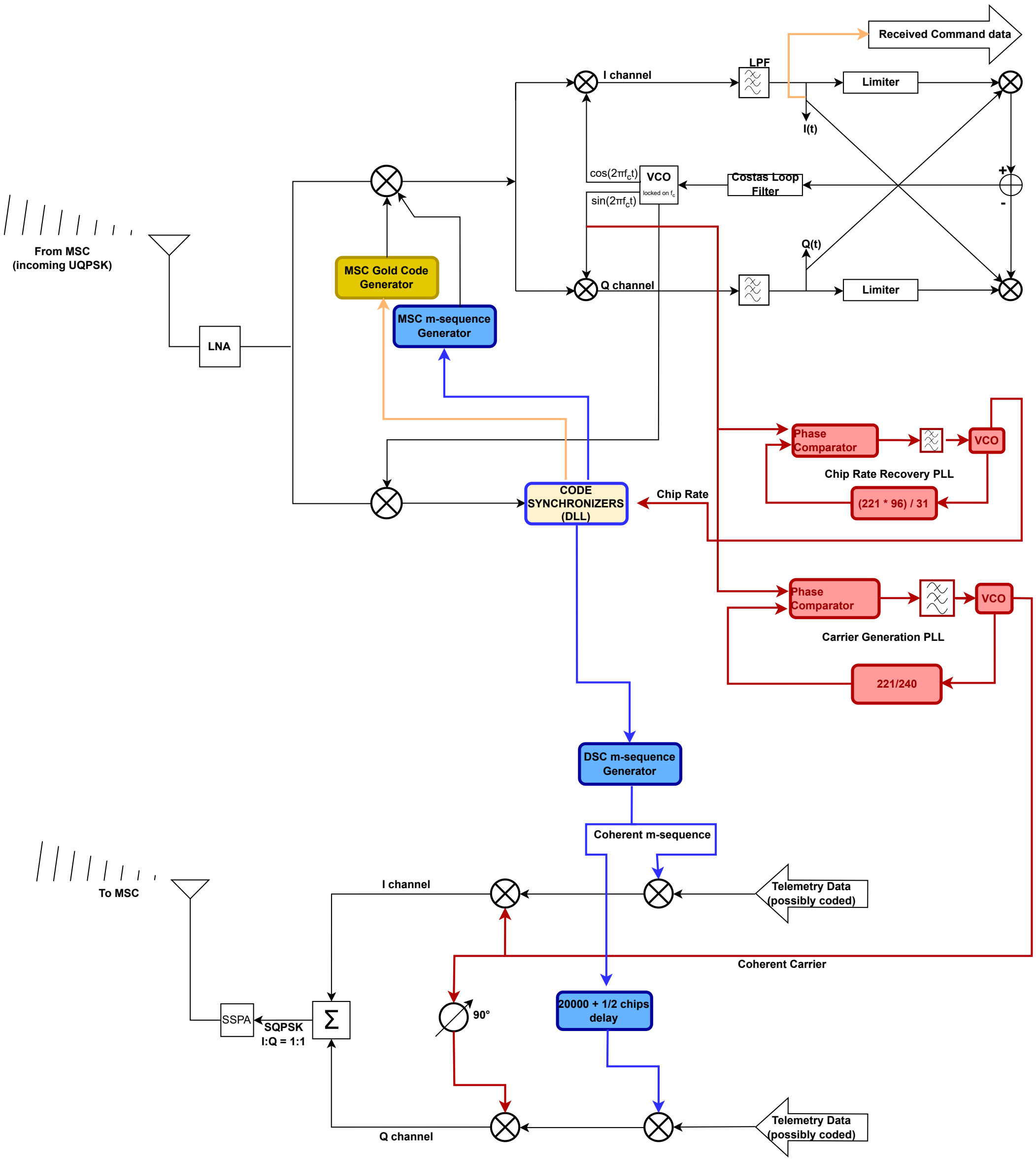

Figure 4.14: DSC Receiver and Transmitter

Chapter 5

Developed Software Elements

5.1 TX DSP Chain

The work carried out in this part of the thesis project falls within the category of digital modulations, approached with USRPs. These are software defined radios, widely exploited nowadays since they allow to perform all the baseband processing in the digital domain, forgetting about the old days in which a case-specific analog signal processing was slowing down the development and testing process. A subsequent digital to analog conversion (through the use of on-board DACs) will serve as interface with the RF front end. The X300 (embodying the MSC functions) relies on its daughterboard, the BasicTX, for the conversion of its digital samples into a modulated waveform lying in IF between 1 and 250 MHz.

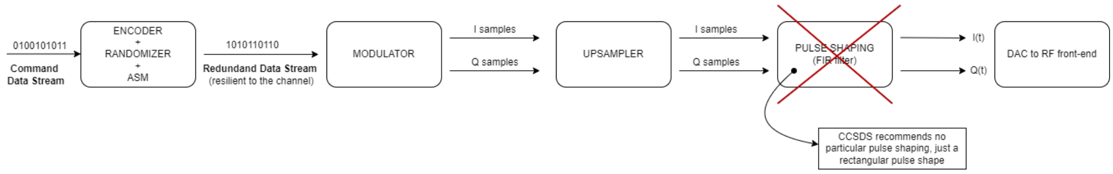

Figure 5.1: MSC Baseband Tx Processing

Figure 5.1 shows the logic steps in order to modulate the electromagnetic physical layer for digital data transmission using a software defined radio. The first block in the depicted processing chain, the Encoder, takes care of adding some redundancy bits to the informational bits in order to make the transmitted frame of bits resilient to the channel impairments which could destroy the information being transmitted just by flipping one bit. This allows for the receiver to perform error detection or even error correction depending on the encoding scheme. Without going too deep in the description of the encoding process, it is sufficient for the reader to acknowledge the fact that for any k bits of information, n bits will be generated by adding r bits of redundancy very often referred to as parity bits.

$$n = k + r$$

Encoding schemes are hence also described by their coding ratio expressed by the ratio $\left(\frac{k}{n}\right)$ of information bits over the number of encoded bits for each codeword being generated. What the encoder does is, in fact, generating codewords starting from uncoded bits. Such codewords belong to the Hamming space $c \in H^n$ while the information frames being encoded belong to the Hamming space $c \in H^k$. For such reasons, the usual way of referring to any encoding logic is by writing $C(k, n)$. Since the correspondence between uncoded frames to codewords is a biunivocal relationship, the cardinality of the codebook (the ensemble of all the possible codewords generated by the same encoding scheme) is the same of the informational frames' Hamming space H^k (i.e. there are 2^k possible codewords for any $C(k, n)$ code). There are two main families of encoders nowadays and these are the Convolutional and the Block codes. Since the focus of this project is not on the development of any encoding process, the explanation of the aforementioned families will be skipped and it will be enough to just assume that the digital bit stream to be transmitted is possibly coded, hence more resilient to channel noise. Ultimately, it is to be noticed how the incoming bitrate is modified (increased) by the encoder since the incoming rate must match the outgoing flow rate otherwise congestion would occur at this processing stage.

$$R_b^{coded} = \frac{n}{k} R_b^{uncoded}$$

The Randomizer and the Attached Synchronization Marker (ASM) serve to avoid long sequences of zeros or ones thus ensuring a sufficient number of transitions and a uniform power distribution over the frequency spectrum occupied by the modulated waveform (the former) and to allow the recognition of the boundaries of the transmitted codewords (the latter).

The subsequent block in the processing chain is the Modulator which will map the bits of the encoded stream to I and Q samples depending on the constellation of the chosen modulation. For the MSC, following the guidelines from CCSDS, an Unbalaced QPSK modulation was chosen (Figure 5.3), with the I channel power being 10 times the power on the Q channel used for ranging purposes.

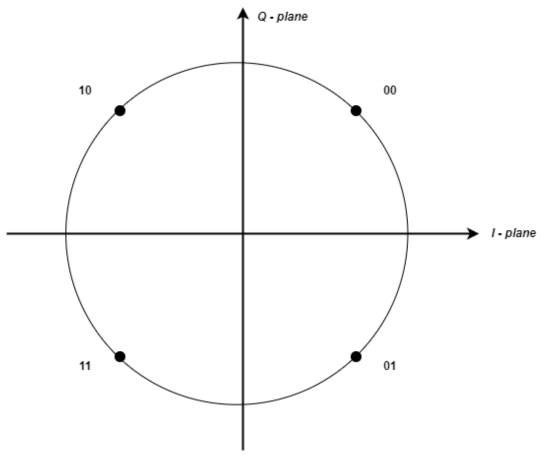

Figure 5.2: QPSK Constellation Gray Labeling

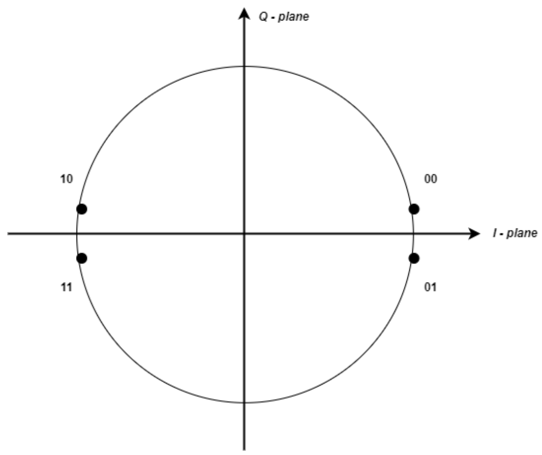

Figure 5.3: UQPSK Constellation Gray Labeling

Approaching first the analytical description of a QPSK (Figure 5.2) signal we have that a band-pass QPSK-modulated waveform can be written in the form:

$$x(t) = a(t)\cos(2\pi f_c t + \phi(t))$$

with:

- $a(t) = \sqrt{\frac{2E_s}{T_s}}$
- $\phi(t) = \frac{\pi}{4}(2i + 1)$ for i = 0,1,2,3

As previously mentioned, working with the USRPs we are interested in working as much as possible in the baseband domain therefore it is useful to expand the previous formula in order to express it as a two-dimensional linear modulation of the form:

$$x(t) = \sum_{k=1}^{2} a_k \psi_k(t)$$

with $\psi_1(t)$ and $\psi_2(t)$ being two orthonormal functions, basis of the two-dimensional Hilbert space. Thus, the QPSK-modulated signal can be written as:

$$x(t) = a(t)[\cos(\phi(t)) \cos(2\pi f_c t) - \sin(\phi(t)) \sin(2\pi f_c t)]$$

$$x(t) = a(t) \cos(\phi(t)) \cos(2\pi f_c t) - a(t) \sin(\phi(t)) \sin(2\pi f_c t)$$

$$x(t) = \sqrt{\frac{2E_s}{T_s}} \cos(\frac{\pi}{4}(2i+1)) \cos(2\pi f_c t) - \sqrt{\frac{2E_s}{T_s}} \sin(\frac{\pi}{4}(2i+1)) \sin(2\pi f_c t)$$

$$x(t) = \sqrt{E_s} \cos(\frac{\pi}{4}(2i + 1))\psi_1(t) + \sqrt{E_s} \sin(\frac{\pi}{4}(2i + 1))$$

where $\psi_1(t) = \sqrt{\frac{2}{T_s}} \cos(2\pi f_c t)$ and $\psi_2(t) = -\sqrt{\frac{2}{T_s}} \sin(2\pi f_c t)$ are the two basis of the two-dimensional Hilbert space. Their coefficients are the real and imaginary parts of the I-Q plane and they vary, each T_s, depending on the constellation symbol being transmitted. It is hence handful to represent the bandpass signal $x(t)$ with its complex envelope (its baseband representation) in order to work with a baseband low-frequency signal.

$$\tilde{x}(t) = I(t) + jQ(t)$$

$$\tilde{x}(t) = \sqrt{E_s}\cos(\frac{\pi}{4}(2i+1)) + j\sqrt{E_s}\sin(\frac{\pi}{4}(2i+1))$$

The up-converted real signal will then be:

$$x(t) = \Re\left(\tilde{x}(t)e^{j2\pi f_c t}\right)$$

$$x(t) = \Re(I(t)\cos(2\pi f_c t) + jQ(t)\cos(2\pi f_c t) +$$

$$jI(t)\sin(2\pi f_c t) - Q(t)\sin(2\pi f_c t))$$

$$x(t) = I(t)\cos(2\pi f_c t) - Q(t)\sin(2\pi f_c t)$$

as shown in figure 5.4.

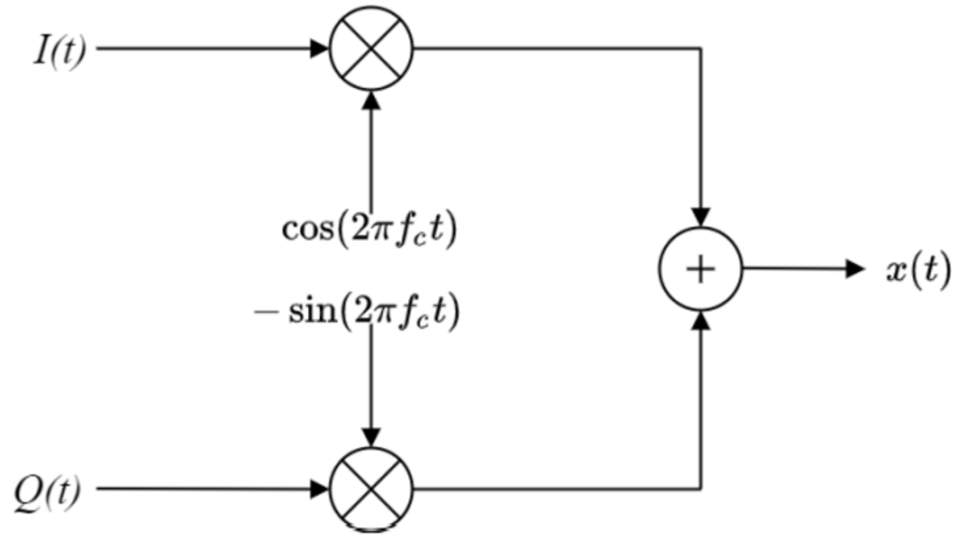

Figure 5.4: Baseband to Bandpass Up-conversion

Following what has been described so far, the structure of a QPSK modulator would be simply a mapper taking chunks of 2 bits and generating the in-phase and in-quadrature samples according to the grey labeling shown in figure 5.2.

As depicted in figure 5.5 the NRZ encoding has been set with the levels $\pm\frac{\sqrt{2}}{2}$ instead of the canonical ± 1 so that the constellation symbols all fall within a unitary energy circle. However, in compliance with CCSDS as of [7] and [8], the uplink should be characterized by a

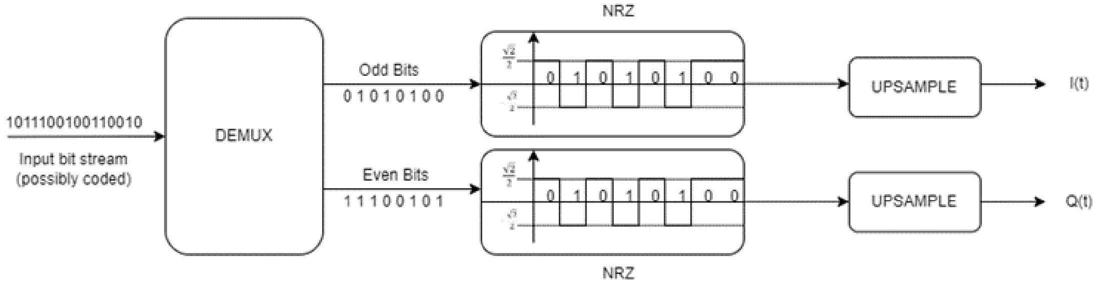

Figure 5.5: QPSK modulator

power unbalance 10:1 between the I and Q components in favor of the former. In order to realize it, the NRZ line coding should have different levels rather than $\pm\frac{\sqrt{2}}{2}$. By imposing the four constellation points to have all unitary energy we can derive the levels for the I plane to be $\pm\sqrt{\frac{10}{11}}$ and the levels of the Q plane to be $\pm\frac{1}{\sqrt{11}}$ (Figure 5.6). Finally, remembering that the MSC actually has to transmit the spread

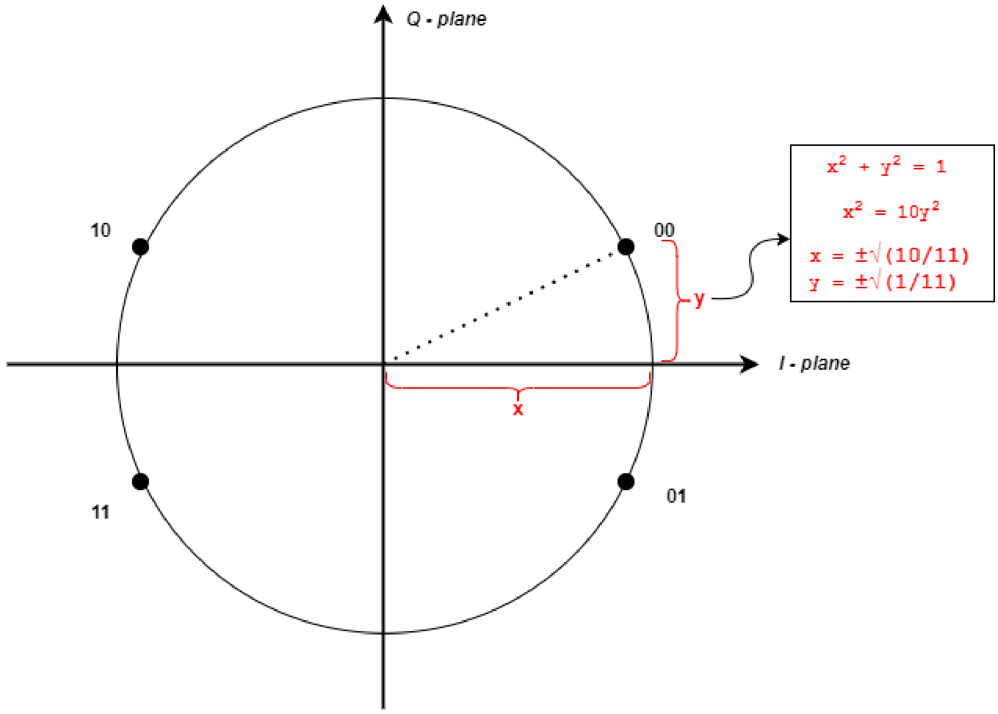

Figure 5.6: UQPSK Unitary Circle

sequence of command bits (possibly encoded) on the I channel and the ranging maximal length sequence on the Q channel, it is possible to define the UQPSK modulator of interest as in figure 5.7.

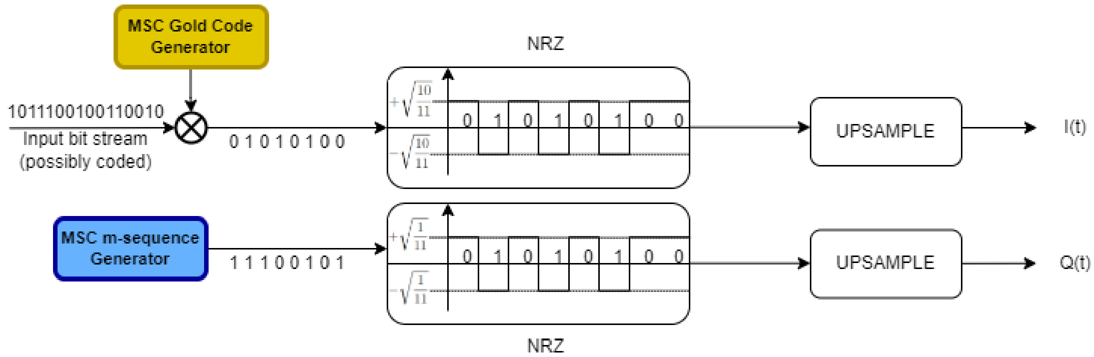

Figure 5.7: UQPSK modulator

Following the guidelines the Gold Code and the Maximal Length sequence have been found and tested for their correlation properties. In Appendix A both code families are presented in more details for the more interested reader.

5.1.1 MSC Gold Code

In order to generate the Gold Code to be transmitted on the I branch of the MSC, only the initial condition of register A has to be defined since the architecture of the two LFSRs has fixed and well defined taps (Figure 4.9). Register A has been set with initial condition 1111111111 (all 1s) and the 1023 chip sequence has been derived with MATLAB. Its autocorrelation, critical for the sequence alignment at the receiving DSC, is shown in the plot in Figure 5.8. It is evident that the sequence respects the typical correlation values for Gold codes which are:

- length L (only for $R(0)$)
- -t
- t-2

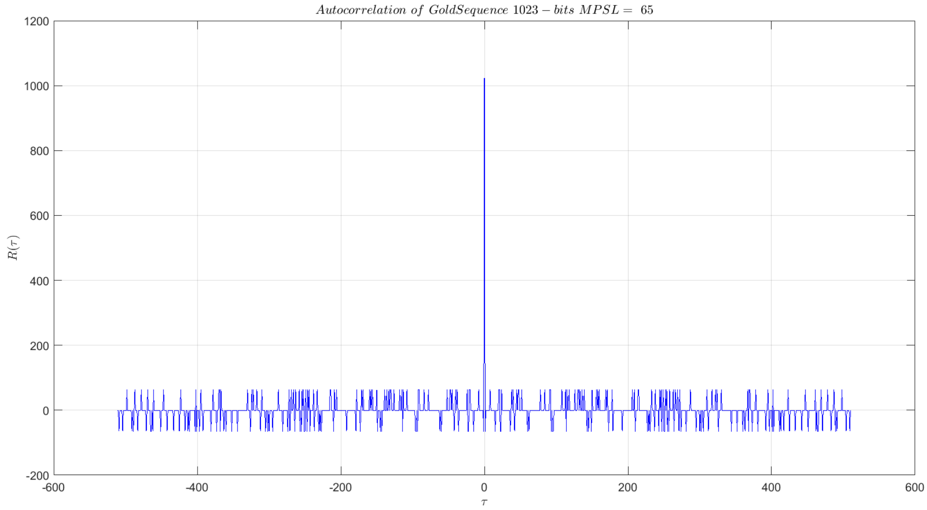

Figure 5.8: MSC Gold Code Autocorrelation

where $t = 2^{\frac{n+2}{2}} + 1$ and n is the number of registers of the two generating LFSRs. Whenever such n is an odd number $t = 2^{\frac{n+1}{n}} + 1$. Consequently, in the considered case $n = 10$, the 3 possible values assumed by the un-normalized correlation are 1023, -65 and 63.

5.1.2 MSC Maximal-Length sequence

Similarly, the maximal sequence has been generated in MATLAB. This time the initial condition is given and fixed for all CCSDS-compliant users (all 1s condition) since what differ from user to user is the feedback taps configuration. The primitive polynomial that has been found for the 18-stages LFSR is:

$$z^{18} + z^{10} + z^8 + z^7 + z^6 + z^5 + z^4 + z^3 + z^2 + z^1 + 1$$

This corresponds to 10 feedback taps. The obtained binary sequence has then been truncated of its last 255 bits in order to be an integer multiple (length-wise) of the Gold sequence (Figure 5.9). Truncating the maximal sequence degrades its autocorrelation function which is expected to peak in zero and to be equal to -1 for every other shift τ

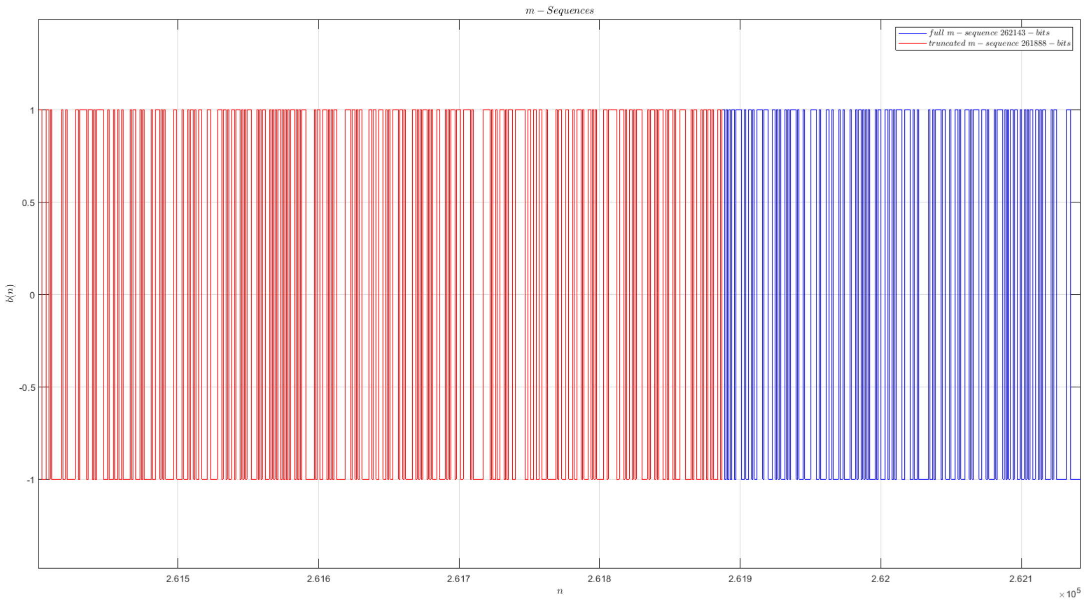

Figure 5.9: MSC M-sequence truncation

(Figure 5.10). It is predictable that truncating the sequence will lead to a significant increase in the Maximum Peak Side Lobe (MPSL) of the autocorrelation function $R(\tau)$ but this does not represent a problem as long as $MPSL \ll R(0)$.

As expected, for shifts different than 0 there is no more a constant autocorrelation value of -1 but the maximum absolute side peak reaches 1084 (Figure 5.11). A zoom at the right tail of the function (Figure 5.12) gives a better idea of such degradation which is however negligible if compared to the huge zero-centered peak.

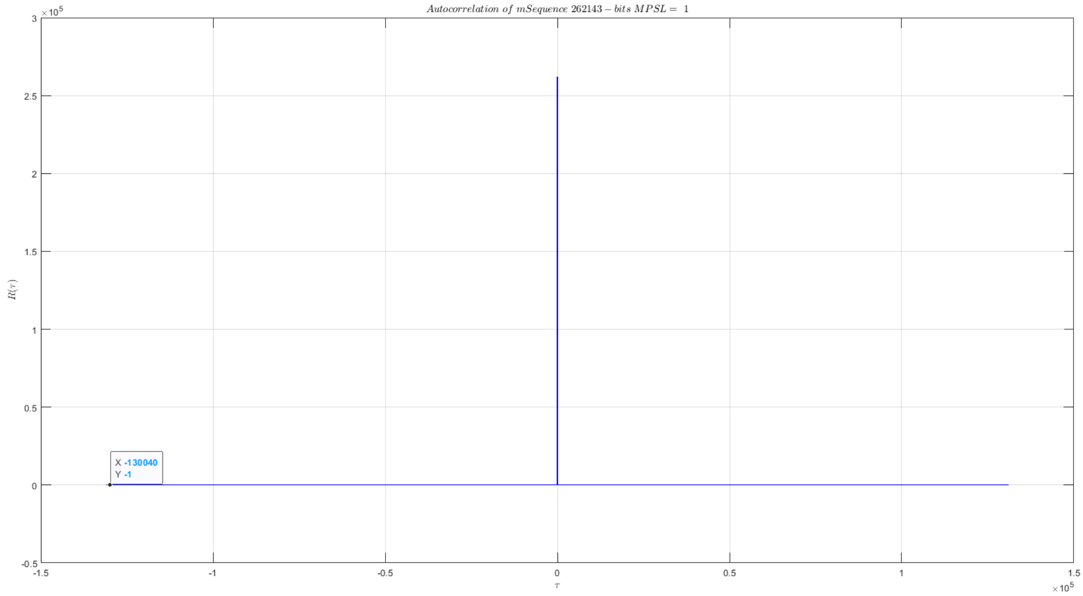

Figure 5.10: MSC M-sequence Autocorrelation

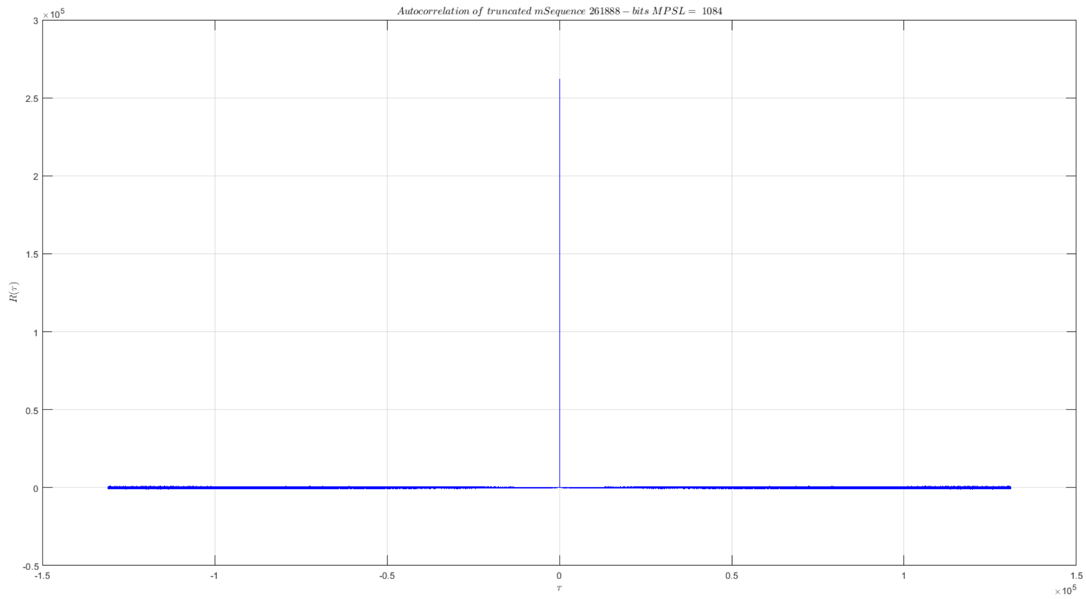

Figure 5.11: MSC Truncated M-sequence Autocorrelation

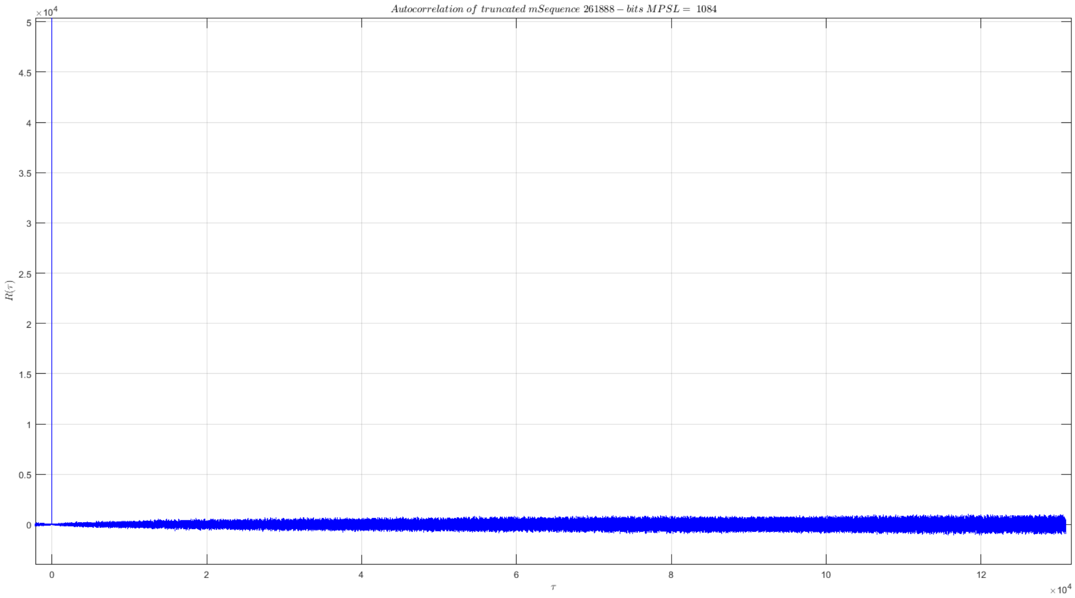

Figure 5.12: MSC Truncated M-sequence Autocorrelation Zoom

5.1.3 Transmitted Signal

After having generated and imported from MATLAB the PN sequences, the block scheme depicted in figure 5.1 has been implemented by writing a C++ program (5.13) interfaced to the USRP X300 thanks to the hardware APIs provided by the radio manufacturer.

Before transmitting at the desired chiprate of ≈ 3 Mcps, a lower rate transmission has been tested in order to verify the consistency and stability of the software. The latter iterates cyclically over a static vector preloaded with the Gold and Maximal-Length sequences interleaved (even bits belonging to the I branch code and odd bits belonging to the Q branch code).

By setting a 50 kchips/s transmission with rectangular pulse shape and connecting the signal outputted from the SMA connector of the BasicTX to a spectrum analyzer, the transmitted signal looks like shown in Figure 5.14. The setted chiprate corresponds to a 50 ksymbols/s (each IQ chip pair is carried by a symbol) and due to an up-sampling of 4 it resolves into a total sample rate of 200 ksamples/s. As expected, the null-to-null bandwidth of the main lobe is the nominal one for a

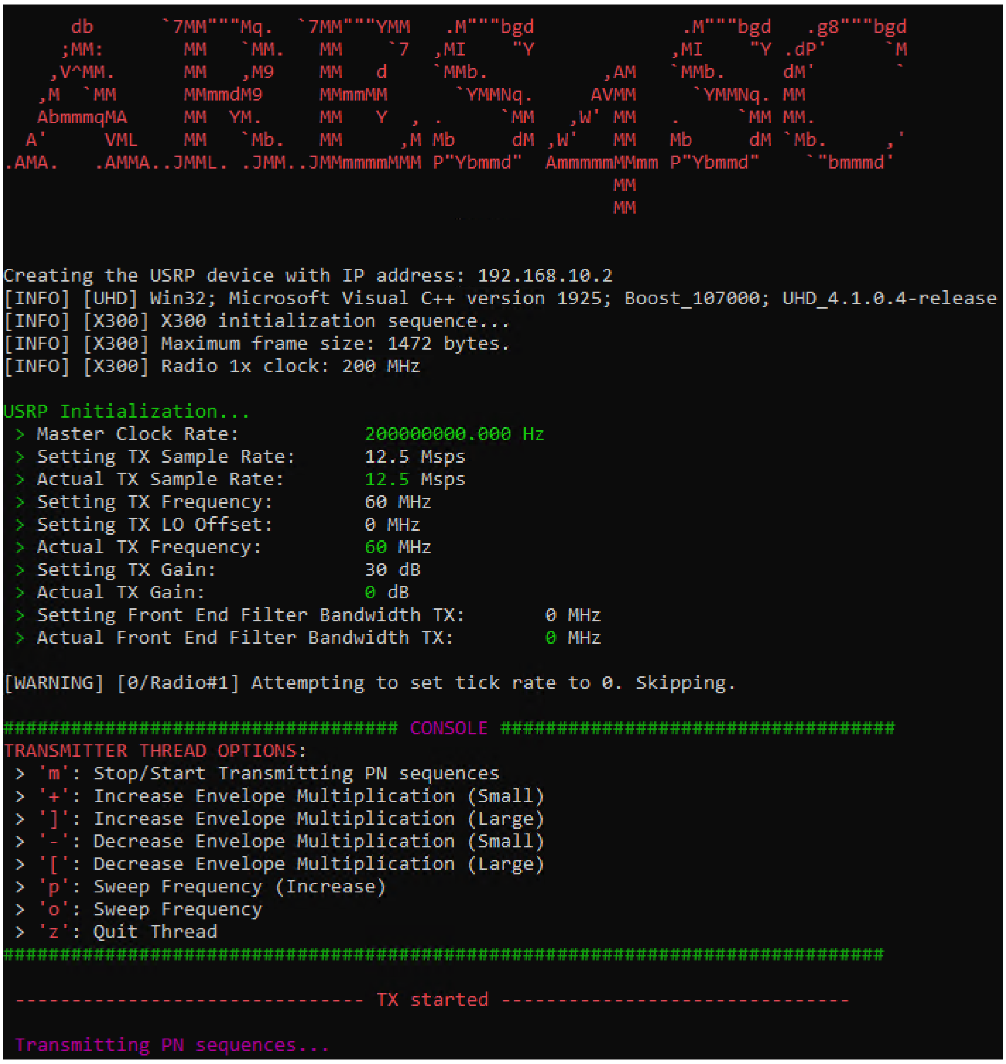

Figure 5.13: Insight of the C++ program

non filtered signal: twice the symbol rate, hence 100 kHz.

Even though the CCSDS guidelines suggest no pulse shaping, a test transmission has been performed anyway to appreciate the difference in the signal's spectrum when shaping the baseband pulse using a Square Root Raised Cosine Filter (SRRC) filter (Figure 5.15). The same symbol rate was adopted, with each symbol still being transmitted each 4 samples but going through a shaping which is spanning, in time, for 20 other symbols yielding a total of 80 filter taps representing the

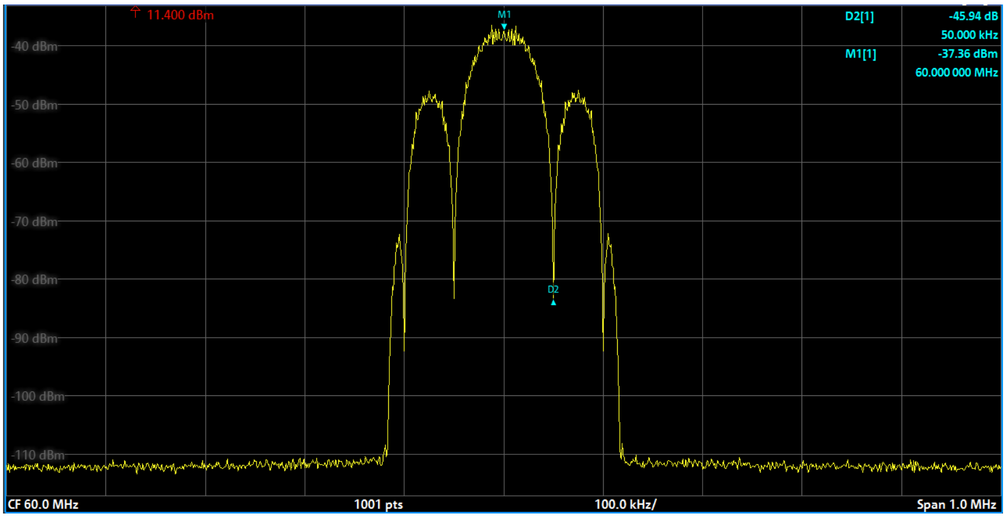

Figure 5.14: Low Chiprate, Rectangular Pulse Signal's Spectrum

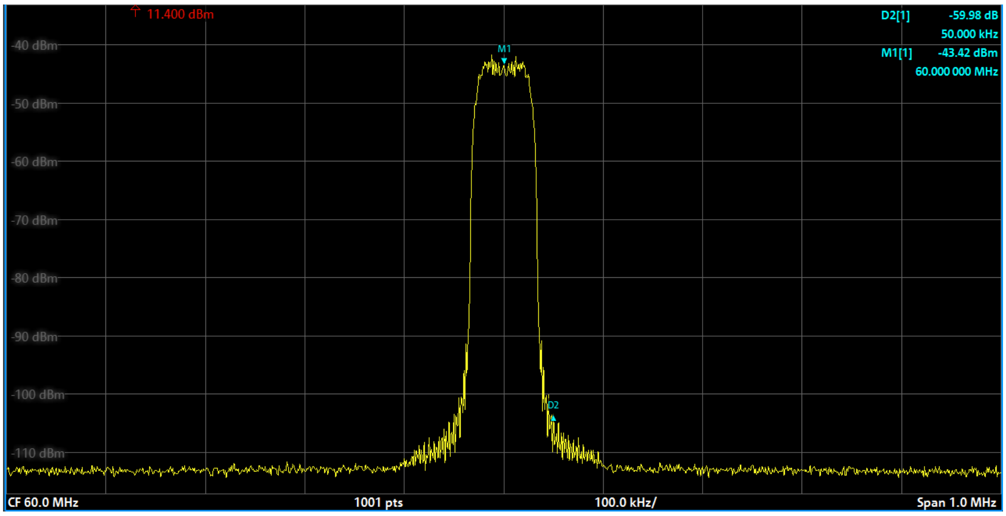

Figure 5.15: Low Chiprate, SRRC-filtered Signal's Spectrum

time domain representation of the SRRC impulse response. The chosen roll-off factor is 0.35 and the total signal's bandwidth depicted in Figure 5.15 matches the expected $Rs(1 + 0.35) = 67.5$ kHz.

Finally the target chiprate (3.125 Mchips/s) transmission was considered, applying the recommended rectangular pulse shape (Figure 5.16). The null to null bandwidth, being twice the symbol rate, equals

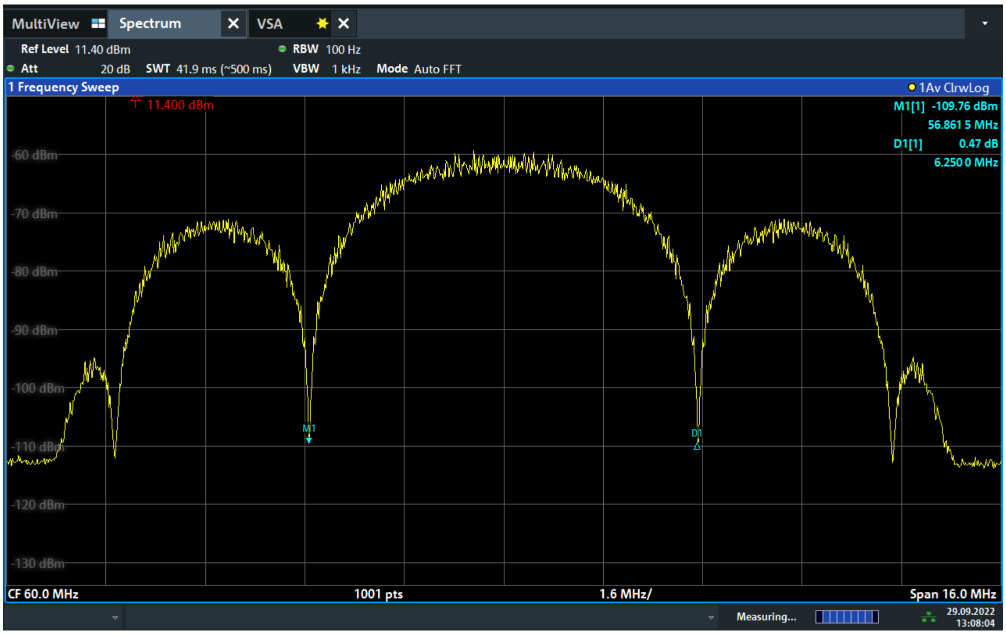

Figure 5.16: Target Chiprate, Rectangular Pulse Signal's Spectrum

6.250 Msymb/s.

One additional verification step aimed to verify the unbalancing of the QPSK modulation through the use of a Vector Signal Analyzer (VSA) (Figure 5.17).

Figure 5.17: Transmitted Signal at the VSA

5.2 RX DSP Chain

COMPANY CONFIDENTIAL

5.2.1 Signal Acquisition

COMPANY CONFIDENTIAL

5.2.2 Signal Tracking

COMPANY CONFIDENTIAL

Chapter 6

USO Stability

Critical aspect of the technology demonstrator is the characterization of the performances of the USO adopted as reference sinusoidal signal in the up and down-conversions stages at the MSC.

When speaking of ultra-stable oscillators, the performances are not related to how much its frequency is accurate with respect to the declared nominal one, but instead we refer to its frequency stability during a specified measurement interval. Depending on the length of the considered time interval we refer to long term stability ($\tau > 100$ s) or short term stability ($\tau < 100$ s).

The characterization of such frequency stability can be performed either in frequency domain by considering its Single Side Band (SSB) Power Spectral Density (PSD) or in time domain by considering the Allan Deviation [12] (square root of the Allan Variance) of the oscillator.

6.1 Phase Noise Characterization

The frequency domain description of the phase noise considers the PN power spectral density expressed in dBc/Hz since it is the ratio of the noise power measured in 1 Hz bandwidth at a given offset f_m with respect to the power of the carrier centered in f_c. Since the PSD of the oscillator is symmetric with respect to the center frequency the SSB fully characterizes its behavior (Figure 6.1).

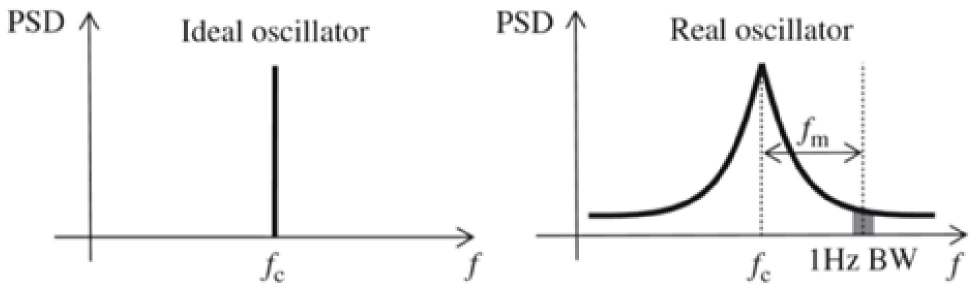

Figure 6.1: Ideal (left) vs Real Oscillator (right) PSD

6.2 Allan Variance Characterization

The Allan Variance (AVAR), also referred to as the two-sample variance, is the most common and effective way of characterizing the frequency stability of atomic clocks and crystal oscillators in the time domain. It was originally ideated by *David W. Allan* and it's denoted as $\sigma_y^2(\tau)$.

The Allan Deviation (ADEV), sometimes simply called sigma-tau is the square root of the AVAR and is denoted as $\sigma_y(\tau)$. When the frequency stability of ultra-stable signal references was investigated, it was discovered that the phase noise of such oscillators was not characterized only by white noise (which has a constant power spectral density virtually across all the frequency spectrum) but also by other types of noise like red noise and flicker noise, the latter having a power spectral density proportional to f^{-1} and sometimes also referred to as pink noise. Evaluating the classical standard deviation of these other types of noise would yield a non-converging result for long integration times. The ADEV, on the other hand, measures the normalized frequency deviations of a signal with respect to its nominal frequency and has the advantage of being convergent for most types of noise affecting the source under test.

We can model the clock as a sinusoidal waveform of a given amplitude and frequency both for the ideal case and for the real case scenario:

- $u(t) = A\cos(2\pi v_o t)$ **ideal clock**
- $u(t) = [A + \epsilon(t)]cos(2\pi v_o t + \phi(t))$ **real clock**

We can then derive the instantaneous frequency as the derivative of the cosine's argument for both cases:

- $v_o = \frac{1}{2\pi}\frac{\delta}{\delta t}(2\pi v_o t)$ **ideal instantaneous frequency**
- $v(t) = v_o + \frac{1}{2\pi}\phi^{'}(t)$ **real instantaneous frequency**

In the frequency stability characterization of a real clock source, we can disregard the non-ideal amplitude fluctuations, thus we are interested only in the frequency fluctuations or, equivalently, in the variability of the zero crossing instants of the signal (Figure 6.2).

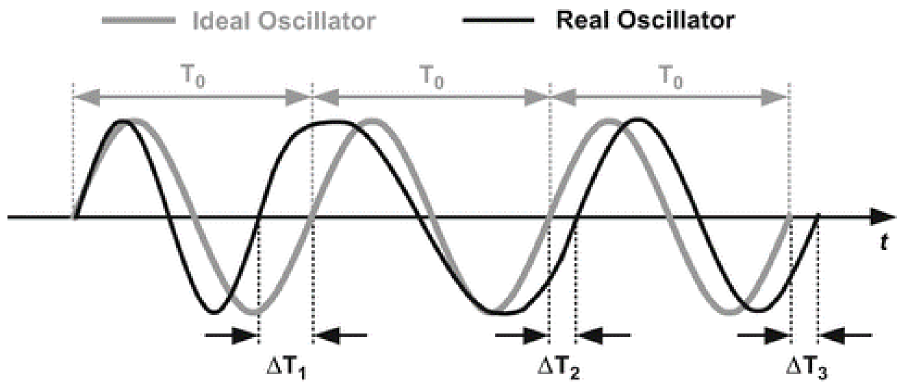

Figure 6.2: Ideal vs Real clocks in time domain

When characterizing clocks' stability there are two fundamental quantities to take in consideration. The first one, necessary to understand the Allan Variance, is the *normalized frequency deviation* expressed as:

$$y(t) = \frac{v(t) - v_o}{v_o}$$

The second is the *time deviation.* In fact, if we had to read the time from a stable reference, we could first define the ideal clock reading time as:

$$h_o(t) = t$$

For the ideal clock it holds:

$$u(t) = Acos(2\pi v_o h_o(t)) = Acos(2\pi v_o t)$$

While instead for the real case:

$$u(t) = Acos(2\pi v_o h_o(t)) = Acos(2\pi v_o t + \phi(t))$$

therefore,

$$h_o(t) = t + \frac{1}{2\pi v_o}\phi(t)$$

The time deviation can then be defined as:

$$x(t) = h(t) - h_o(t) = \frac{1}{2\pi v_o}\phi(t)$$

It can be noted that:

$$y(t) = \frac{\delta x(t)}{\delta t}$$

that is, the normalized frequency deviation is the time derivative of the time deviation.
The **Allan Variance** is defined as:

$$\sigma_y^2(\tau) = \frac{1}{2}\langle(\overline{y}(t+\tau) - \overline{y}(t))^2\rangle$$

where:

- τ is the measurement interval
- $\langle\rangle$ indicates an average over the entire time axis
- $\overline{y}(t)$ indicates the average of the normalized frequency deviation (the first fundamental quantity) over an interval of time of length τ

$$\overline{y}(t) = \frac{1}{\tau}\int_{t-\tau}^{t} y(t')\delta t'$$

The signature of each clock can be evaluated in the *Log Sigma-Log Tau* plot (Figure 6.3) which shows the Allan Deviation as a function of the averaging time. The different types of noise processes can be identified in such graph, also referred to as a bathtub graph due to its shape, by inspecting its slope [13].

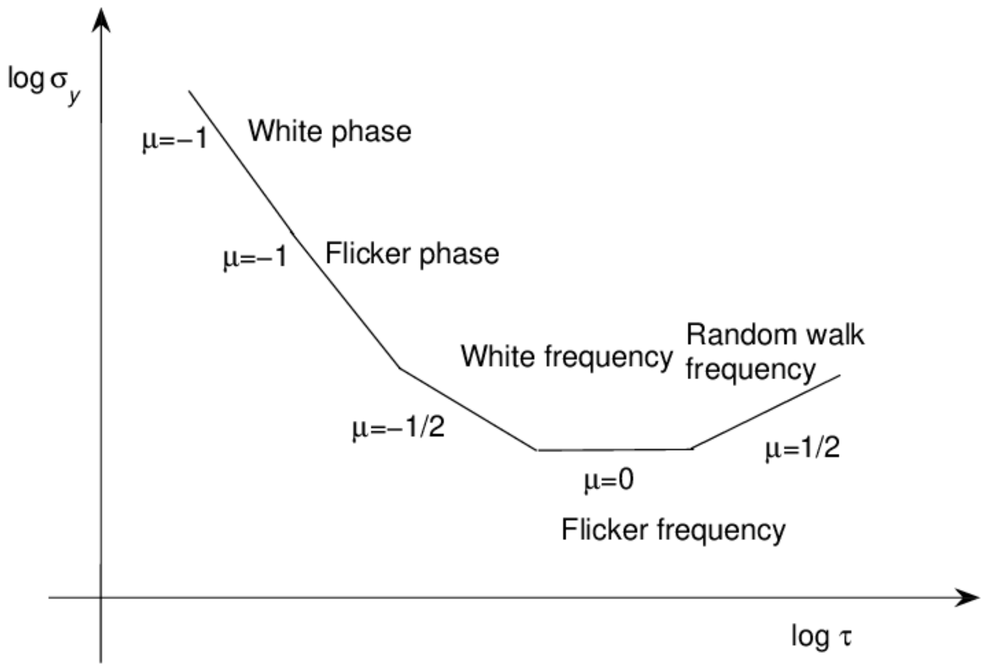

Figure 6.3: Bathtub graph

6.3 Tested USOs

For the developed Technology Demonstrator two different Temperature Compensated Crystal Oscillator (TCXO) have been selected. With respect to normal quartz crystal resonators, these are temperature-compensated meaning that their frequency stability suffers less of thermal changes due to an error control voltage supplied to the crystal oscillator to compensate for temperature-dependent frequency changes. The two selected frequency sources are provided by *Total Frequency Control Ltd.*, both output a 10 MHz sine-wave signal with a frequency accuracy $\leqslant$ 1 ppm and come packed in a small body represented in Figure 6.4.

In particular, two units were bought: one with an accuracy of ± 1 *ppm* and one with an accuracy of ± 0.05 *ppm* which, at 10 MHz, correspond to ± 10 Hz and ± 0.5 Hz respectively. The characterization of the two oscillators consisted in the determination of their SSB Phase Noise

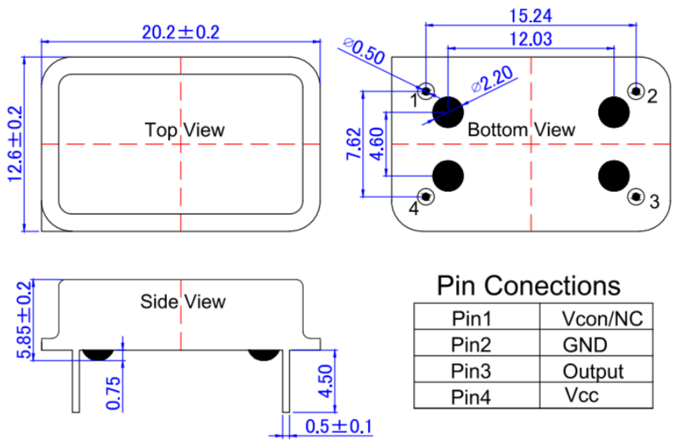

Figure 6.4: TCXOs body, dimensions in mm

and their Allan Variance. The first of the two considered metrics was evaluated by connecting their output signal to a Signal Analyzer with a software for phase noise evaluation. The obtained results are shown in Figure 6.5 for the first USO and in Figure 6.6 for the second USO.

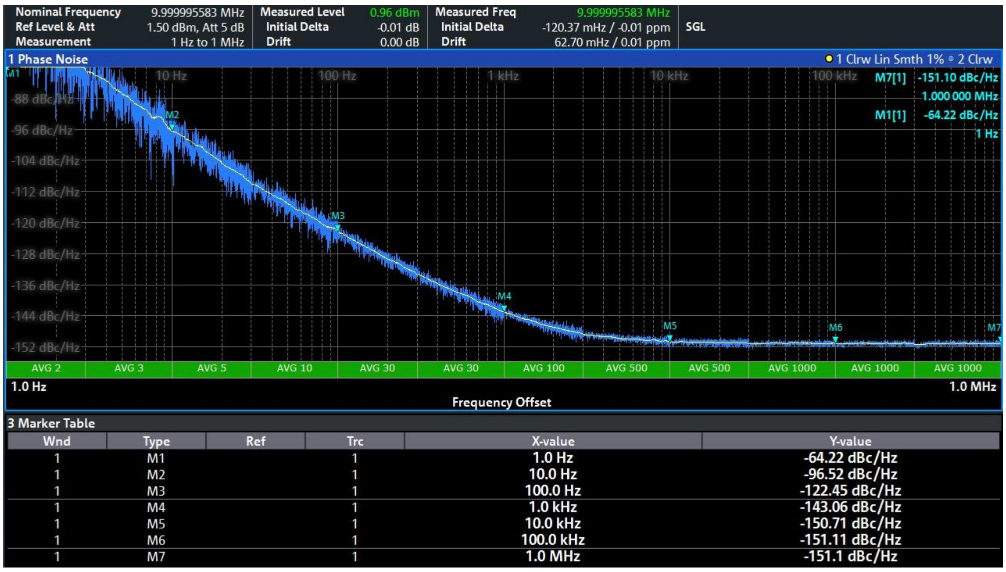

Figure 6.5: 1 ppm USO's Phase Noise Analysis

As shown by the spectrum analyzer screenshots, the less stable oscillator obtained a measured frequency about 4.5 Hz away from the

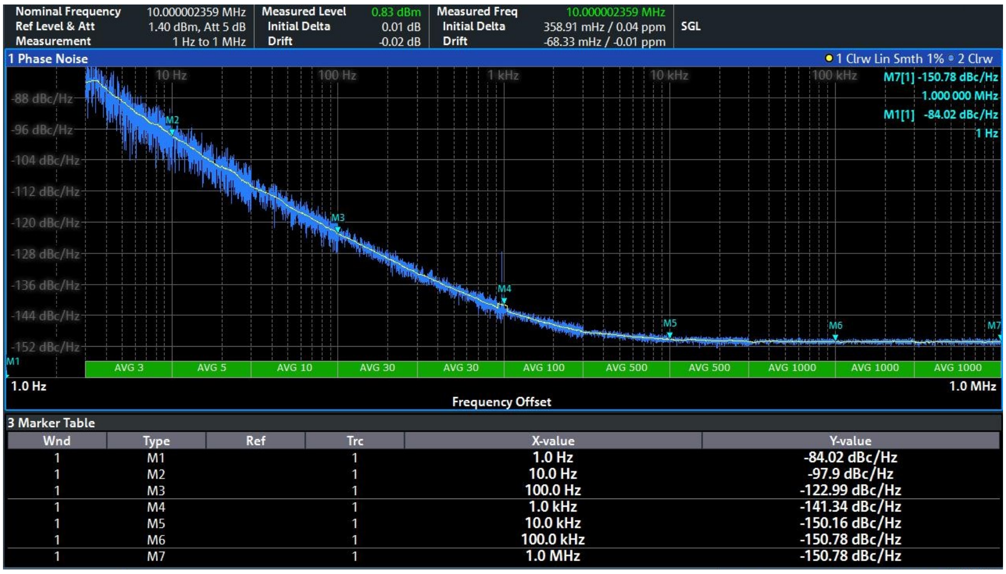

Figure 6.6: 0.05 ppm USO's Phase Noise Analysis

nominal 10 MHz, in accordance with the ±1 *ppm* accuracy, while the second device under test was deviating from the nominal frequency by more than 2 Hz which should be violating the stated ±0.05 *ppm* accuracy. Regarding the phase noise they showed similar, and even better, performances with respect to those provided by the manufacturer datasheets which, for example, were claiming −135 dBc/Hz at 1 kHz from the carrier.

In order to measure the Allan Deviation of the oscillators a ready-to-use software targetting both short term ($\tau < 100$ s) and long term ($\tau > 100$ s) stability was not available so a direct sampling through the USRP X300 was performed and a custom MATLAB application has been developed (Figure 6.8) for their processing. The signals coming from the USOs were fed to the SMA connector of the BasicRX daughterboard, digitally downconverted to baseband and sampled at 180.706 Msamples/s (1020 decimation factor from the 184.32 MHz Master Clock Rate) for 1.5 hours. Subsequently the signal's phase has been computed sample by sample and the instantaneous frequency derived as the phase derivative. For a proper sampling the hardware of the USRP was driven by an Ultra Stable Oven Controlled Crystal

Oscillator (OCXO), more stable than the one under test (Figure 6.7).

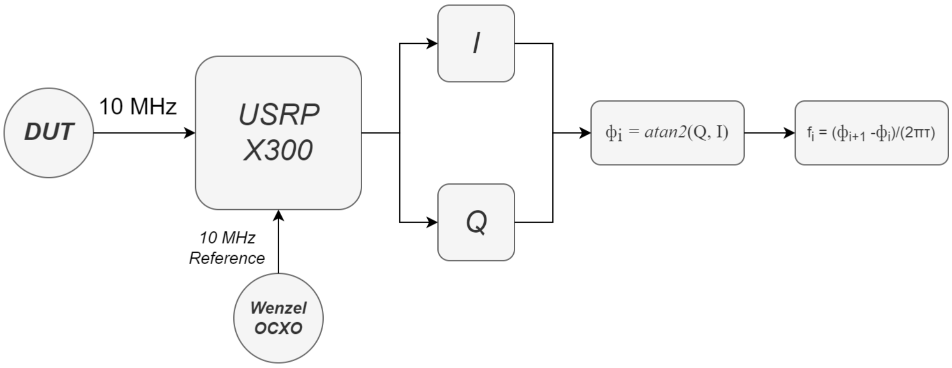

Figure 6.7: Uso Sampling Logic

Thanks to this sample-by-sample processing and implementing in MATLAB the formulas cited previously, it was possible to derive the canonical *Log Sigma-Log Tau* graph for the Allan Deviation characterization. Figure 6.9 and 6.10 report the "bathtub" graphs of the less

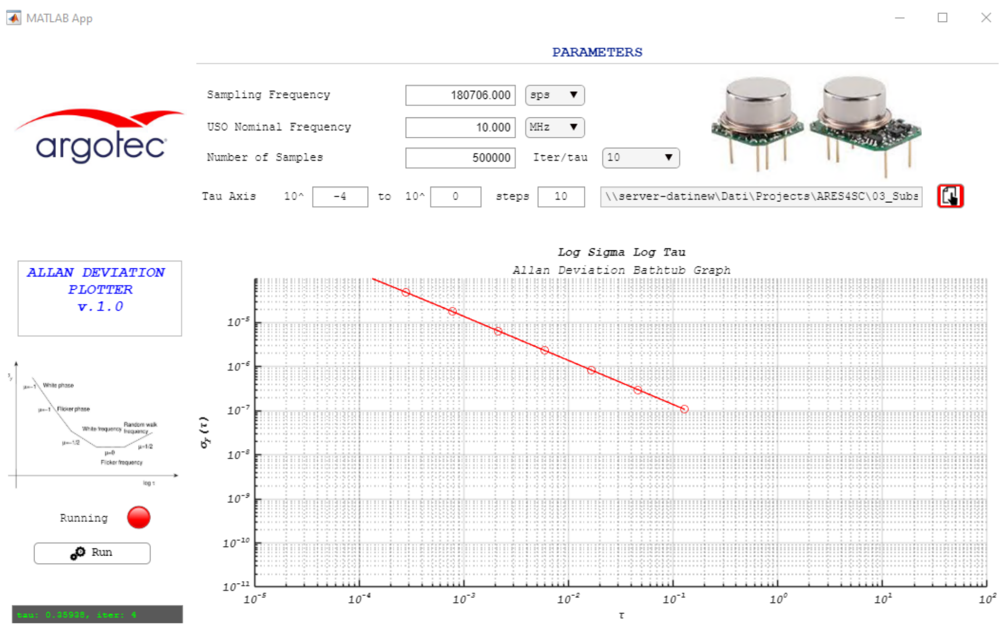

Figure 6.8: MATLAB processing interface

stable USO and more stable USO respectively. Both agree with their datasheets which were claiming an Allan Deviation value of $1.18 \cdot 10^{-10}$ in $\tau = 1$ s.

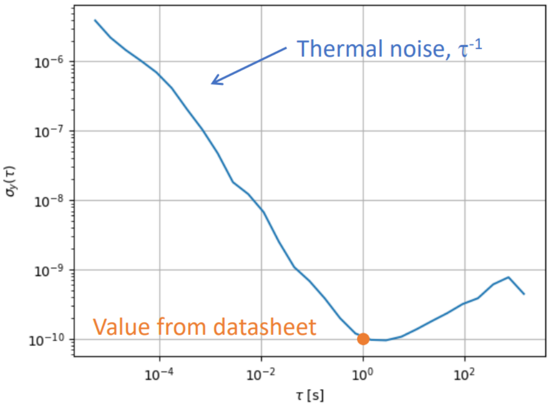

Figure 6.9: 1 ppm USO's Allan Deviation

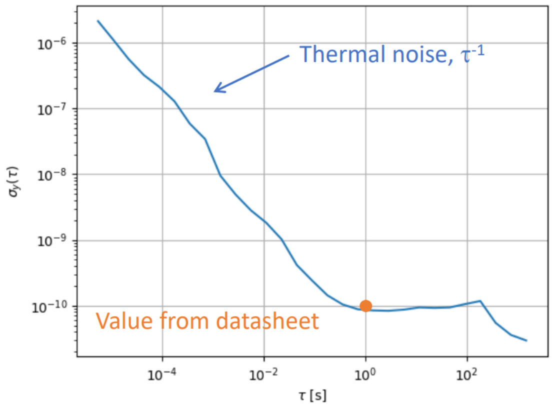

Figure 6.10: 0.05 ppm USO's Allan Deviation

6.4 Phase Noise Suppression Test

In order to prove the analytical demonstration of the Phase Noise suppression reported in section 3.3.2 a test bench has been setup as shown in Figure 6.11. The hardware elements involved in the test are:

- PCB with the two USOs under test
- Board with Integrated PLL and VCO Frequency Synthesizer for 2 GHz syntesis (Local Oscillator)
- LNA for Local Oscillator's signal amplification
- Mixer for Upconversion
- Mixer for Downconversion
- Image Rejection filter (Blue Filter Bar)

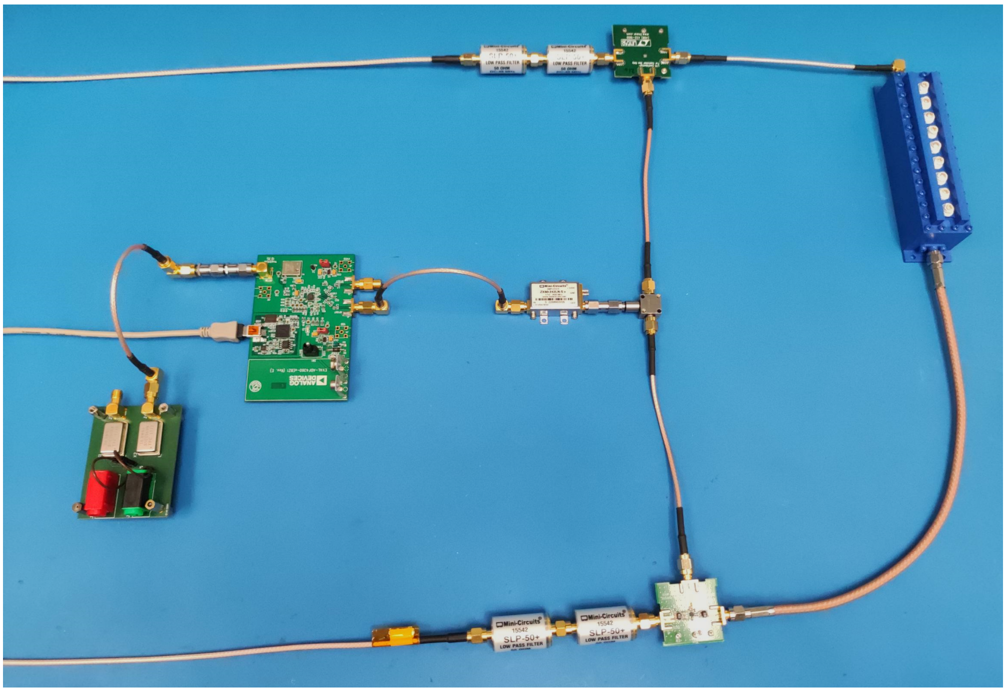

Figure 6.11: Phase Noise Suppression Test Bench

- Low Pass Filters $DC \sim 48$ MHz before Upconversion and after Downconversion

The idea behind Phase Noise suppression lays in the fact that when transmitting and then subsequently receiving a turned-around signal the frequency instabilities introduced by the USO in uplink are then partially suppressed when mixing the same signal for downconversion. The term "partially" in the previous sentence highlights the fact that, as the smartest reader might have already pointed out, not all frequencies are suppressed or better: which frequencies get suppressed depends on someting else, it is not a constant behaviour.

The right interpretation key is that, within a short time period, the noise of a frequency source is correlated with itself. This, along with the fact that the clock noise transfer function consists, in time, in two anticorrelated delta functions as mentioned in 3.3.2, implies that those frequency instabilities of duration greater than the time elapsing between one signal mixing and the other (up and down conversions) are actually suppressed.

In the ARES4SC scenario the short RTLT hence allows for a great phase noise suppression, in particular of all the frequency components whose inverse (period) is larger than the RTLT itself (46.7 ms at most). This translates in a sort of high pass filtering behavior whose cutoff frequency is: $\frac{1}{0.046\ \mathrm{s}} = 21.73$ Hz.

In order to observe such suppression, a Spectrum Analyzer with Phase Noise measuring software and a Signal Generator were used. Both instruments were connected to an Ultra Stable OCXO so that the Local Oscillator, driven by one of the two USOs under test, was the higher noise source in the system. A pure 40 MHz tone was generated, upconverted to 2.04 GHz and analyzed both after the image rejection filter and after the downconverting mixer.
The more stable USO (0.05 *ppm*) was used as reference for the 2 GHz frequency synthesis. Even at a first glance the frequency spectrum is showing clear signs of the happened noise reduction. The first 2.04 GHz signal (Figure 6.12) is clearly "dirtier" than the 40 MHz one (Figure 6.13) which has been downconverted by the same noisy local oscillator which mixed the first.

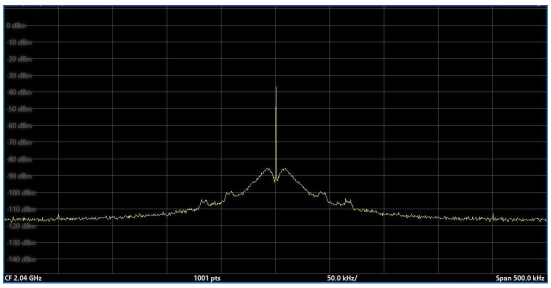

Figure 6.12: Upconverted tone. Oscillator introduced noise in the system.

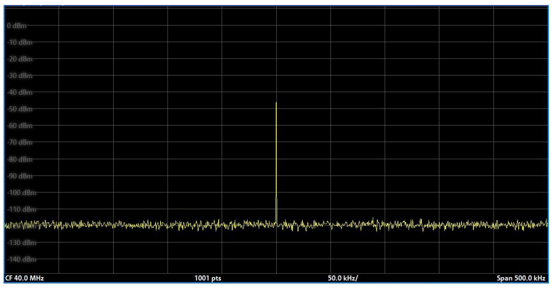

Figure 6.13: Downconverted tone. Some noise left the system.

Following this simple visual inspection, a Phase Noise measurement in the range 1 Hz $\sim$ 1 MHz was performed on the signal at the same previous two points in the circuit. Figure 6.14 shows the results obtained for the upconverted tone.

Figure 6.14: Phase noise measure of the upconverted 2.04 GHz signal

Figure 6.15 instead shows the results obtained for the downconverted tone clearly demonstrating the phase noise suppression.

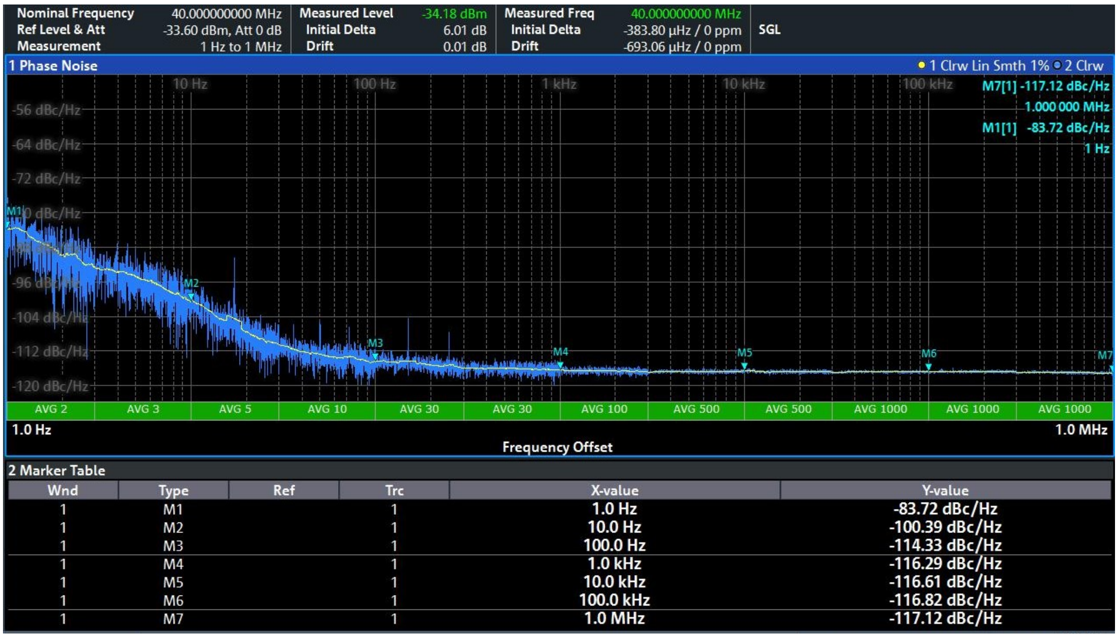

Wnd	Type	Ref	Trc	X-value	Y-value
1	M1		1	1.0 Hz	-83.72 dBc/Hz
1	M2		1	10.0 Hz	-100.39 dBc/Hz
1	M3		1	100.0 Hz	-114.33 dBc/Hz
1	M4		1	1.0 kHz	-116.29 dBc/Hz
1	M5		1	10.0 kHz	-116.61 dBc/Hz
1	M6		1	100.0 kHz	-116.82 dBc/Hz
1	M7		1	1.0 MHz	-117.12 dBc/Hz

Figure 6.15: Phase noise measure of the downconverted 40 MHz signal

The two results have been equally scaled and overlayed in order to compare the noise level differences (Figure 6.16).

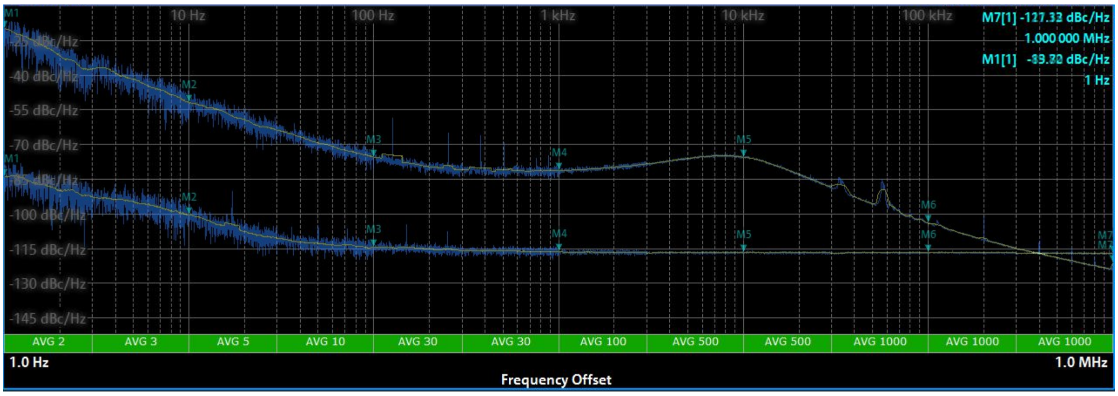

Figure 6.16: Phase noise comparison

Same suppression have been reported using the other USO under test.

Due to the dependency between the suppressed frequencies and the RTLT, the presented test bench with a 1 meter cable separating the two analog mixers is expected to provide a huge 300 MHz wide phase noise suppression. However as it is possible to see from Figures 6.12 and 6.13 the tones are attenuated differently due to the signal attenuating while propagating in the circuit. As a consequence the phase noise comparison presented in 6.16 is not completely fair.
By adjusting the transmitted power level of the Signal Generator, the two spectra have been adjusted (6.17 and 6.18), a phase noise test from 1 Hz to 1 GHz has been run and the results overlayed in Figure 6.19.

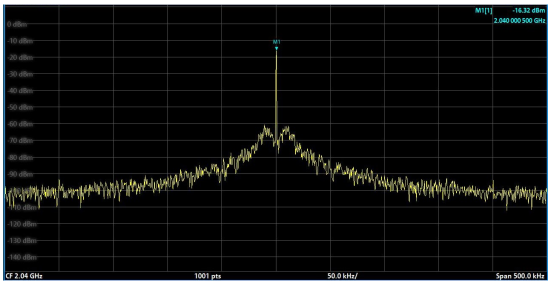

Figure 6.17: 2.04GHz controlled power level

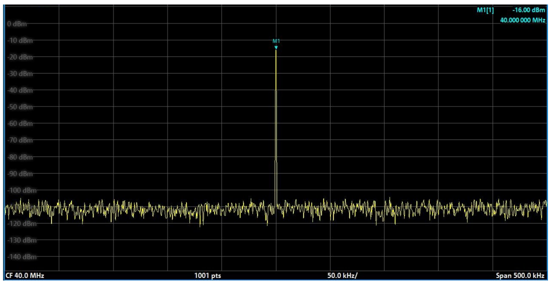

Figure 6.18: 40MHz controlled power level

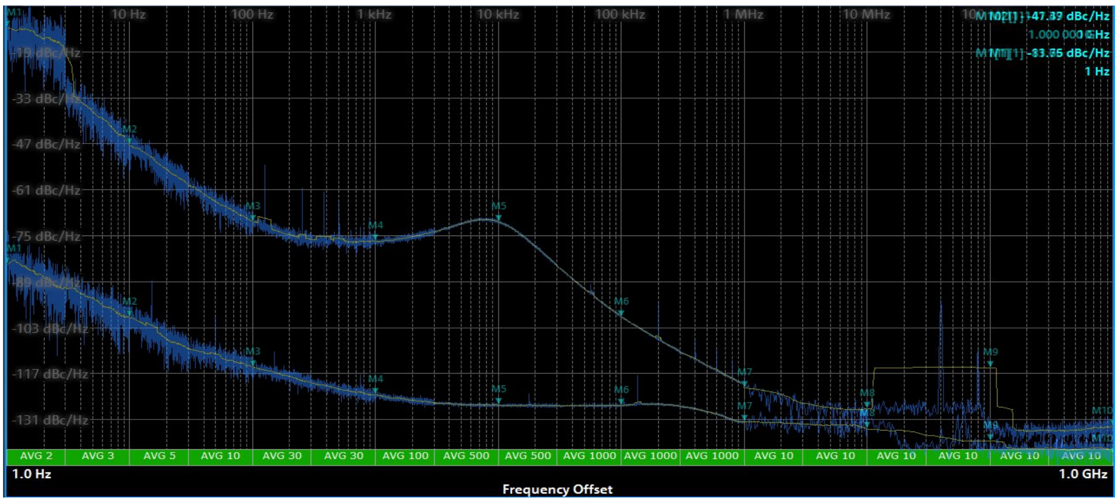

Figure 6.19: Phase noise comparison with same power level

Looking at Figure 6.19, however not possible to confirm the 300 MHz assumption, it is evident that the two signals both reach noise floor level in the 100 MHz - 1 GHz decade.

Chapter 7

Conclusions

7.1 Achieved Results

At the end of the thesis period the technology demonstrator has reached a development point at which the transmission and the reception of the CDMA signal has been developed and tested on a USRP. The designed modulated signal resulted suitable to perform the tracking of the radiometric measures of interest. In particular, it was possible to extract the estimates of the frequency shift and the ranging code delay. To do so, a receiver similar to a GNSS one has been developed within the same multithreaded C++ software also responsible for the transmission. Furthermore, the parallel investigation of the concept of phase noise suppression in the case of short RTLT has been verified in laboratory raising the consciousness about the possibility of adopting cheaper oscillators on-board deep-space missions.

Regarding the radiometric observables, their evolution can easily be followed through the telemetry grapher offered by the COSMOS interface. Concerning the range, instead of relying on a timestamping mechanism, it can be monitored by looking at the code delay change over time. However, in the current laboratory set up the channel emulator has yet to be implemented, thus not allowing to emulate the variable round trip time of the signal which therefore shows a constant code delay. At the present state, the accuracy of the range measure is strongly dependent on the front end sampling rate of the receiver.

Since the latter expects a constant number of samples per chip (which translates in the sampling frequency being an integer multiple of the chiprate), the alignment of the local replica with the incoming code happens with an accuracy of one sample time. In other words, since the chosen sampling frequency for the receiver is 12.5 Msamples/s the spatial accuracy is equal to $c \cdot \frac{1}{f_s} = 23.98$ m. This means that whenever the distance between transmitter and receiver increases (decreases) by 23.98 m the code delay estimate should increase (decrease) by one sample.

On the other hand, the frequency estimates resulted to have an approximate variability of $\pm$ 0.05 Hz when using a carrier tracking loop bandwidth of 100 Hz and a variability of $\pm$ 0.005 Hz when using a loop bandwidth of 15 Hz (Figures 7.1 and 7.2). Recalling section 3.3.2 on the Doppler measurement error budget and the fact that for a two-way link it holds $\Delta f = \frac{2\Delta v}{c} \cdot f_{tx}$, we have that the range-rate accuracy is within:

$$\Delta v = \frac{c\Delta f}{2f_{tx}} = \begin{cases} 249{,}8\ mm/s & @\ 60\ MHz \\ 7{,}5\ mm/s & @\ 2\ GHz \\ 1{,}875\ mm/s & @\ 8\ GHz \end{cases} \qquad \text{for } \Delta\text{f} = 0.1 \text{ Hz}$$

$$\Delta v = \frac{c\Delta f}{2f_{tx}} = \begin{cases} 24{,}98\ mm/s & @\ 60\ MHz \\ 0{,}75\ mm/s & @\ 2\ GHz \\ 0{,}1875\ mm/s & @\ 8\ GHz \end{cases} \qquad \text{for } \Delta\text{f} = 0.01 \text{ hz}$$

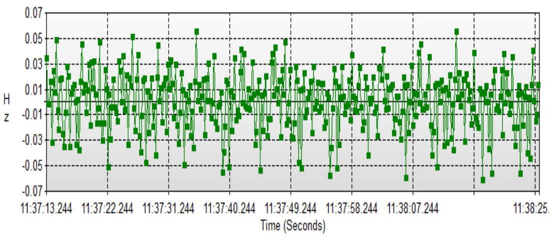

Figure 7.1: Frequency Estimate with 100Hz CTL bandwidth

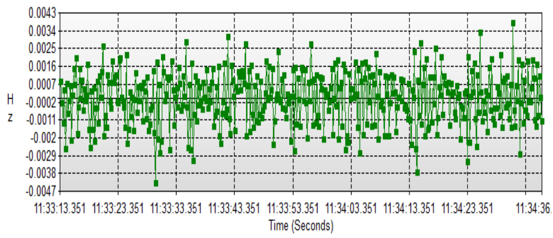

Figure 7.2: Frequency Estimate with 15Hz CTL bandwidth

7.2 Future Steps

Future improvements of the developed Technology Demonstrator will involve a proper channel emulation in order to test the studied signals against the realistic channel conditions that the satellites constellation would experience in their Martian orbits.

Concerning the radiometric observables extraction, there is margin for improving the obtained accuracies by either increasing the sampling rate of the receiver or by choosing the latter to be a non integer multiple of the chiprate in order to obtain a sub-sample accuracy in the code alignment performed within the DLL of the tracking stage. To reach sub-sample accuracy the *incommensurability constraint* shall be exploited, thus requiring the receiver to deal with a non constant number of samples per chip (which translates in the sampling frequency being a non integer multiple of the chiprate). To understand this concept the

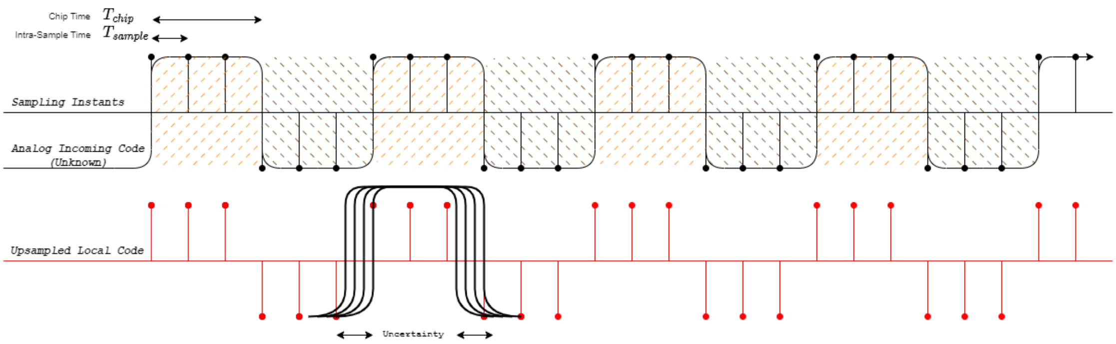

Figure 7.3: Integer Number of Samples Per Chip

condition of a constant number of samples per chip pulse is represented in Figure 7.3 with the continuous line representing the unknown analog signal of the incoming code sampled by the ADCs at a rate F_s. The red line, instead, represents the locally generated replica of the code. As it is highlighted in the picture, by aligning the two codes there is still uncertainty about the underlying analog signal true phase.

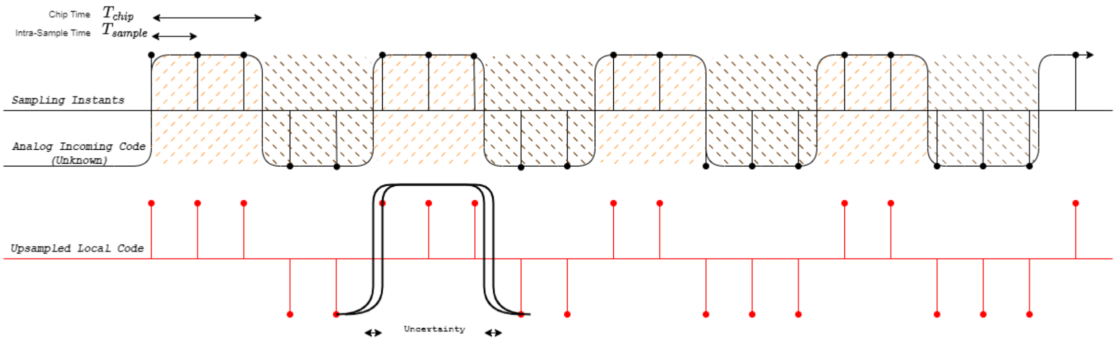

Figure 7.4: Non Integer Number of Samples Per Chip

On the other hand, in Figure 7.4 it is possible to see how such uncertainty can be reduced by setting the ADCs to sample at a rate non multiple of the chip rate. In the presented example some chips have been sampled 3 times while others only 2 with a periodic pattern which in this specific case is 3, 2, 3, 2, 2 samples per chip.

Appendix A
Gold Codes

This appendix is dedicated to a Professor of mine that significantly contributed to my accademical growth by instilling in me part of his passion for the digital communications, even though he is probably not aware of that. His name is *Roberto Garello*.

I was attending one of its classes at Politecnico di Torino when I first heard about Maximal Length sequences and, consequently, about Gold Codes. This section is meant to provide the reader with some insights about the properties and the usages of the mentioned pseudo noise sequences, as they were explained to me during the lectures.

The primary benefit of these codes concerns their auto and cross correlation properties which turn out to be essential in digital receivers for the detection and the unspreading of CDMA signals.

In particular, a Maximal Length sequence shows extremely low (ideally 0, practically -1) auto correlation values whenever the considered code shift is different than 0. On the other hand, a Gold Code exhibits advantageous cross correlation values with other Gold Codes which belongs to a certain set of other "privileged, matched" codes. Such features are widely exploited in the digital communications world and relevant are the use cases of GNSS signals and 5G which use these codes to respectively share the spectrum in a CDMA logic and distinguish the different Base Stations to allow a proper synchronization between the broadcasting antenna and the user equipment. Moreover, being able to generate a deterministic yet pseudo random sequence is exploitable in any randomization stage, a fundamental step to both hide the digital information stream to unintended users and evenly distribute the transmitted power over the whole portion of used bandwidth. Both can be easily generated in hardware with LFSRs and since the Gold sequences are a particular form of Maximal Length sequences, the latter are presented first.

M-sequences

Maximal Length sequences, often referred to as M-sequences, have very good properties in terms of randomness in the sense that they very closely resemble the characteristics of ideal random sequences.
In the ideal case, we have that the bits are equiprobable and statistically independent with:

$$P(b_i = 0) = P(b_i = 1) = 1/2$$

Hence, for any purely random sequence the number of zeros and the number of ones is expected to match in the long run. Same holds for the number of bit transitions. As a consequence, if we compare a binary random sequence against a shifted version of itself it will result in half of the bits being equal and half being different. Thus, converting a random sequence of length L from binary to its bipolar representation $(0 \to +1; 1 \to -1)$ it holds:

$$R(\tau) = \sum_{i=0}^{L-1} b_i \cdot b_{i-\tau} = 0$$

In the case of M-sequences these random properties are almost met, but not fully. As mentioned, these sequences are the results of the output line of a Linear Feedback Shift Register and this makes them reproducible and deterministic but at the same time prevents them from being purely random. This impossibility is, in fact, a direct consequence of the way an M-sequence is generated. In order to understand the reason, it is important to have in mind the exact structure of such generating shift register and the implications behind its

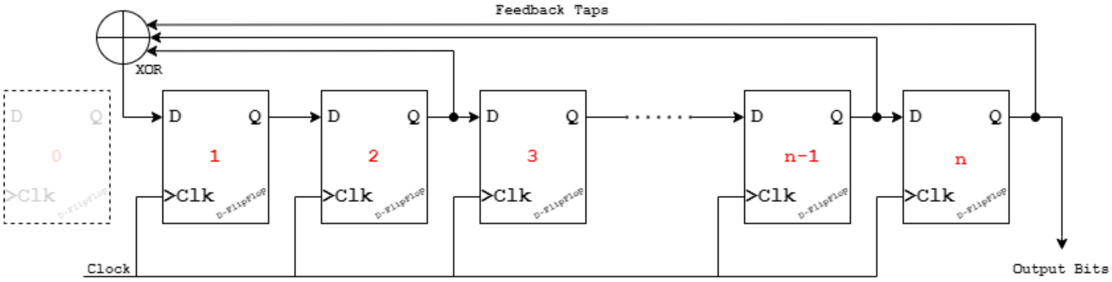

Figure A.1: LFSR for a generic m-sequence

feedback connections. In figure A.1 n Delay Flip Flops are aligned and connected one cascated to the other. At each clock cycle the bits (voltage levels) at the output of each Flip Flop are shifted left to right and the output of the rightmost one is one bit of the sequence. The outputs of some inner Flip Flops are derived, XORed together and feeded as input to the first element of the LFSR. It is now straightforward to assume that different feedback taps yield overall different output sequences and, given the same taps, different initial states for the registers result in different shifted versions of the same output sequence. Again, the smarter readers might have already guessed why the codes that are obtainable with this method cannot be purely random. There is, in fact, one state that is never allowable and that is the all zeros state. In such case, no matter the chosen feedback taps, the result of the xor operation will be indefinitely zero thus having the LFSR iterating forever in the same state. As a consequence, despite being theoretically 2^n the possible states of the n registers the feasible ones are $2^n - 1$: this constitutes part of the solution for the complete answer to what we were investigating, namely the non ideal randomness of the output sequence. The other piece of the puzzle lies in the term *maximal* itself. What does *"Maximal Length"* actually mean? Well, once we agree on the fact that are the feedback taps that determine which sequence it is outputted, the answer is only a small step further. In fact, being the possible states for the registers $2^n - 1$, does not automatically mean that the LFSR will iterate over all of them since which bit is inputted to the leftmost Flip Flop depends on the result of the XOR operation only.

Thus, the term maximal refers to a careful selection of the feedback taps that allow the n registers to traverse all the possible $2^n - 1$ states causing the output sequence to be of the *"Maximal Length"* $2^n - 1$ and to repeat itself cyclically. Finally we can show the nature and the reason behind the non ideal randomness by realizing that the sequence will always have an odd length and with a slightly unbalanced number of zeros with respect to the number of ones. In fact, by not allowing the all zeros state, the number of 0s will be equal to the number of 1s minus one. As a consequence, for a bipolar M-sequence it holds:

$$R(\tau) = \sum_{i=0}^{L-1} b_i \cdot b_{i-\tau} = -1 \qquad \forall \tau \neq 0$$

Furthermore, if the chosen number of feedback taps is odd then also the all 1s state has to be forbidden since the result of a XOR operation between an odd number of 1s is always 1.

Now there are enough premises to introduce the reader to the way LFSR-generated M-sequences are usually addressed, that is, with their polynomial representation. It is clear, in fact, that each feedback configuration yields a different output sequence and there are some configuration better than others since they provide a maximal lenght sequence. For this reason, to uniquely identify an M-sequence it is enough to declare the number of registers and the selected taps. Following the enumeration in red of Figure A.1 we can write a polynomial by considering the terms that take part in the summation at the input line of the first Flip Flop. The caracteristic polynomial of the shown LFSR would hence be:

$$D^0 + D^2 + D^{n-1} + D^n$$

It can be derived by considering the polynomial terms of grade equal to the Flip Flop numbers whose outputs get summed and inputted to the Flip Flop n^o 1. An imaginary Flip Flop n^o 0 can help remember this rule. Whenever such describing polynomial is primitive, the generated sequence is granted to be of maximal length.

Gold Codes

Gold Codes, named after *Robert Gold*, are binary sequences which share a similar nature with the Maximal Sequences but with some differences that makes them preferable over the former whenever good cross correlation properties are needed. Such good cross correlation (meaning that for every $\tau \neq 0$ the correlation value is considerably low) holds, however, only among certain sequences belonging to the same "privileged" set: the Gold Set. By selecting a *preferred pair* of M-sequences it is possible to generate a Gold Set by simply XORing one sequence with all possible shifted versions of the other. The mechanism is shown in Figure A.2. By preferred pair it is meant a couple of M-

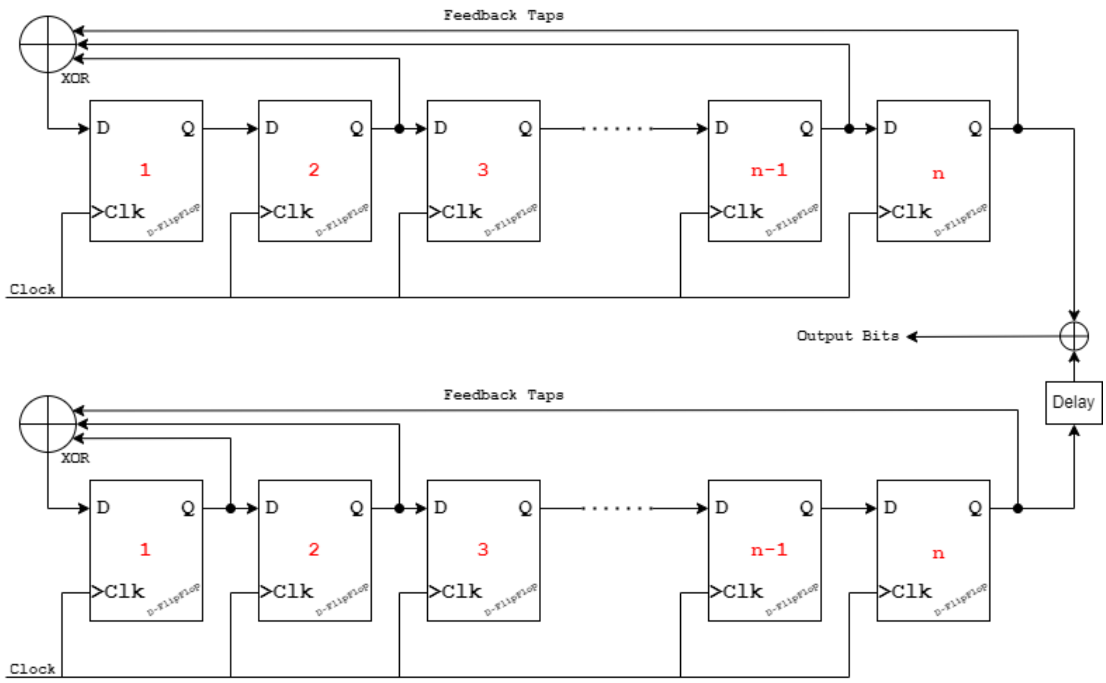

Figure A.2: LFSRs for a generic Gold sequence

sequences of the same length which show a maximum cross correlation value less or equal than $2^{(n+2)/2}$ where n is the degree of the generating polynomial of the two sequences. Since such Gold Set comprises the two chosen M-sequences plus all the sequences obtained by XORing the

first against all possible delays of the other, the resulting cardinality of the set is $2 + 2^n - 1 = 2^n + 1$.
Therefore, by picking two bipolar sequences of length L and within the same set we are sure that their cross correlation values would never exceed a certain value and in particular by defining:

- $t = 2^{(n+2)/2} + 1$ if n is even
- $t = 2^{(n+1)/2} + 1$ if n is odd

their correlation function can assume only 3 values:

$$R(\tau) = \sum_{i=0}^{L-1} b_1(i) \cdot b_2(i-\tau) = \begin{cases} -1 \\ -t \\ t-2 \end{cases}$$

Appendix B

Kalman Filter

This appendix, similarly to the previous one, is dedicated to another Professor of mine that made me grow in terms of passion towards the beautiful engineering field of signal processing. His name is *Lorenzo Galleani*.
Since the Kalman Filter (actually an extended version of it) has been used to estimate the orbital state of the constellation starting from the measures extracted from the ISL, this section will provide the reader with the basic functioning of such estimation technique, even though it is not at the core of this thesis work. A basic example of a system state estimation will be presented.
The following is taken from a *Lorenzo*'s lecture which is reported entirely due to its completeness and beauty.

The Kalman Filter provides **linear**, **unbiased**, **optimal** and **recursive** estimate of the state of a **dynamical system** from its **noisy measurements**.

- **linear**: the current estimate is a linear combination of the previous estimates and the current measurement

- **unbiased**: the mean estimation error is zero

- **optimal**: the variance of the estimator is minimum

- **recursive**: the current estimate depends only on the previous estimate and the current measurement

Before providing the necessary characterization of the models for the dynamical system and for its noisy measurements, let's see first why the Kalman Filter is actually called a filter and why it's recursive nature is so important.

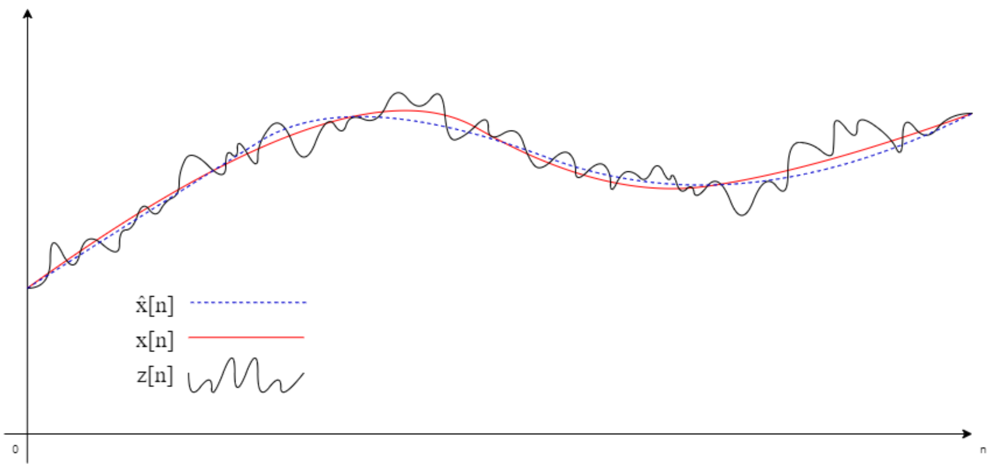

Figure B.1: State, State Estimate and Noisy Measures

As we can see in Figure B.1, in order to generate the state estimate $\hat{x}[n]$ by only having access to the noisy measurements $z[n]$ requires first to filter out noise, thus explaining the filtering nature of the Kalman Filter.

Concerning the importance of being recursive, it mainly concerns the computational cost which is notably lower compared to non recursive algorithms. Suppose, in fact, to want to calculate the estimate of the mean value of some measurements $z[1], z[2], z[3], ..., z[n-1]$. By using the sample mean estimator, at time $n-1$ we have:

$$\hat{x}[n-1] = \frac{1}{n-1}\sum_{k=1}^{n-1} z[k]$$

At time n, the estimator becomes:

$$\hat{x}[n] = \frac{1}{n}\sum_{k=1}^{n} z[k] = \frac{1}{n}\left[\sum_{k=1}^{n-1} z[k] + z[n]\right]$$

$$\hat{x}[n] = \frac{1}{n}\sum_{k=1}^{n-1} z[k] + \frac{1}{n}z[k]$$

by multiplying and dividing by $n-1$:

$$\hat{x}[n] = \frac{n-1}{n}\frac{1}{n-1}\sum_{k=1}^{n-1} z[k] + \frac{1}{n}z[n]$$

we get to a recursive definition of our mean estimator:

$$\hat{x}[n] = \frac{n-1}{n}\hat{x}[n-1] + \frac{1}{n}z[n]$$

The big advantage, which now should be more evident, lies within the computational cost and in the memory usage (Table B.1).

Table B.1: The importance of being recursive

Estimator Type	**Computational Cost**	**Memory Usage**
non recursive	$\sim n$	$\sim n$
recursive	fixed!	fixed!

Now we can proceed in characterizing the dynamical system's general model and how measurements can be defined in function of that.

In particular, at each time n, the discrete time **system state vector** can be expressed as linear combination of the system inputs, the system noise and the system evolution since time $n-1$.

$$x[n] = \Phi x[n-1] + \eta[n-1] + bu[n-1]$$

where:

- $x[n] = \begin{bmatrix} x_1[n] \\ x_2[n] \\ : \\ : \\ x_M[n] \end{bmatrix}$ is the $M \times 1$ **state vector**

- $\Phi = \begin{bmatrix} \cdot & \cdot & \cdot & \cdot \\ \cdot & \cdot & & \\ \cdot & & \cdot & \\ \cdot & & & \cdot \end{bmatrix}$ is the $M \times M$ **transition matrix** defined through the matrix exponential e^{Ft}. F is the system dynamic matrix.

- $\eta[n] = \begin{bmatrix} \eta_1[n] \\ \eta_2[n] \\ : \\ : \\ \eta_M[n] \end{bmatrix}$ is the $M \times 1$ system's **noise vector** in which $\eta_i \sim N(0, Q)$ where Q is the $M \times M$ covariance matrix $E\left[\eta[n]\eta^T[n]\right]$

- $u[n] = \begin{bmatrix} u_1[n] \\ u_2[n] \\ : \\ : \\ u_M[n] \end{bmatrix}$ is the $M \times 1$ vector of the **system's inputs**

Finally, the **noisy measurements** can be modeled as:

$$z[n] = Hx[n] + v[n]$$

where:

- $z[n] = \begin{bmatrix} z_1[n] \\ z_2[n] \\ : \\ : \\ z_L \end{bmatrix}$ is the $L \times 1$ **measurements vector**

- $H = \begin{bmatrix} \cdot & \cdot & \cdot & \cdot \\ \cdot & \cdot & & \\ \cdot & & \cdot & \\ \cdot & & & \cdot \end{bmatrix}$ is the $L \times M$ **measurement matrix**

- $v[n] = \begin{bmatrix} v_1[n] \\ v_2[] \\ \vdots \\ \vdots \\ v_L[n] \end{bmatrix}$ is the $L \times 1$ **measurement noise** vector in which $v_i \sim N(0, R)$ where R is the $L \times L$ covariance matrix $E\left[v[n]v^T[n]\right]$

Now, before presenting and demonstrating the nature of the Kalman estimator and before the reader will panic or get bored by the not so tangible flow of equations, an example of a dynamical system modeled along with its noisy measures is presented. Hopefully the patient reader will be able to resolve all its doubts by reasoning with something real and concrete.

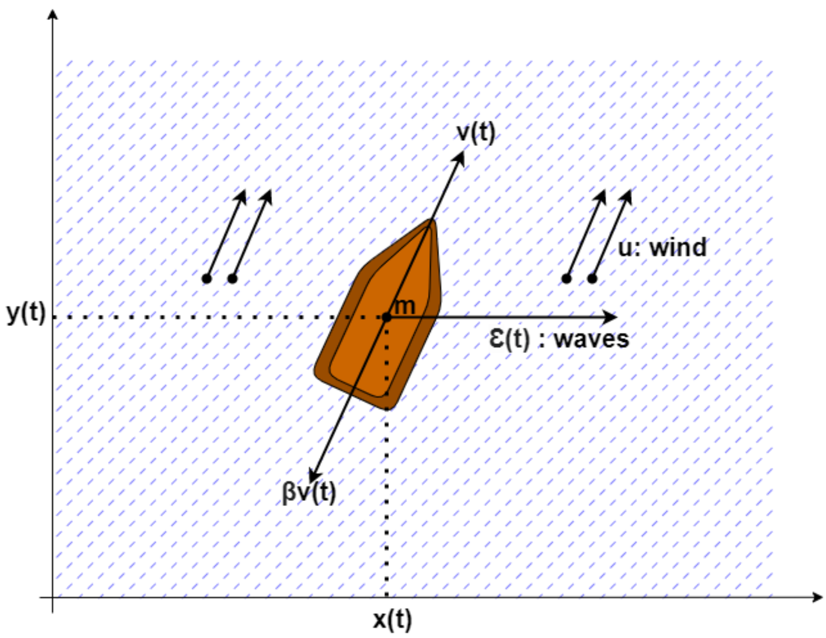

Figure B.2: A boat on the ocean...

As shown in Figure B.2 the motion of a boat on the ocean will be the pivot element to allow ourselves to relate the theory with the practice. In the image, u is a constant **wind force**, m is the **mass** of the boat, $v(t)$ its **velocity**, β is the friction **coefficient**, $\beta v(t)$ the **force** of such friction and finally $\varepsilon(t)$ the **force** due to the random motion of the waves, thus assumed to be White Gaussian Noise.

Let's describe the boat's motion by starting from the Newton's Law:

$$f(t) = m \cdot a(t)$$

Along the x direction we hence have:

$$f_x(t) = m \cdot a_x(t)$$

Thus, the total forces acting on the x direction:

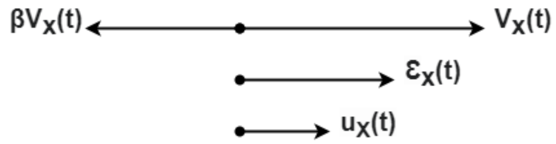

$$f_x(t) = \varepsilon_x(t) + u_x - \beta v_x(t)$$

By substituting $a_x(t) = \frac{\delta v_x(t)}{\delta t} = \dot{v}_x(t)$:

$$\varepsilon_x(t) + u_x - \beta v_x(t) = m\dot{v}_x(t)$$

$$m\dot{v}_x(t) + \beta v_x(t) = \varepsilon_x(t) + u_x$$

Considering, for simplicity and without lack of generality, $m = 1$:

$$\dot{v}_x(t) + \beta v_x(t) = \varepsilon_x(t) + u_x$$

$$\ddot{x}(t) + \beta\dot{x}(t) = \varepsilon_x(t) + u_x$$

Since the same hold for the y axis, the equations of the boat's motion are:

$$\begin{cases} \ddot{x}(t) + \beta\dot{x}(t) = \varepsilon_x(t) + u_x \\ \ddot{y}(t) + \beta\dot{y}(t) = \varepsilon_y(t) + u_y \end{cases}$$

Remembering the state vector we can now define one for this example:

$$\underline{x}(t) = \begin{bmatrix} x_1(t) \\ x_2(t) \\ x_3(t) \\ x_4(t) \end{bmatrix} = \begin{bmatrix} x(t) \\ \dot{x}(t) \\ y(t) \\ \dot{y}(t) \end{bmatrix}$$

Since:

$$\underline{\dot{x}}(t) = \begin{bmatrix} \dot{x}_1(t) \\ \dot{x}_2(t) \\ \dot{x}_3(t) \\ \dot{x}_4(t) \end{bmatrix} = \begin{bmatrix} x_2(t) \\ -\beta x_2(t) + \varepsilon_x(t) + u_x \\ x_4(t) \\ -\beta x_4(4) + \varepsilon_y(t) + u_y \end{bmatrix}$$

We can write the **continuous time system model equation**:

$$\frac{\delta}{\delta t}\begin{bmatrix} x_1(t) \\ x_2(t) \\ x_3(t) \\ x_4(t) \end{bmatrix} = \begin{bmatrix} 0 & 1 & 0 & 0 \\ 0 & -\beta & 0 & 0 \\ 0 & 0 & 0 & 1 \\ 0 & 0 & 0 & -\beta \end{bmatrix}\begin{bmatrix} x_1(t) \\ x_2(t) \\ x_3(t) \\ x_4(t) \end{bmatrix} + \begin{bmatrix} 0 \\ \varepsilon_x(t) \\ 0 \\ \varepsilon_y(t) \end{bmatrix} + \begin{bmatrix} 0 \\ u_x \\ 0 \\ u_y \end{bmatrix}$$

which is written in the form

$\dot{X}(t) = FX(t) + \varepsilon(t) + U(t) \qquad where\ F:\ the\ system\ dynamic\ matrix$

Note that these system equations are still expressed in continuous time. In order to derive those in discrete time let's first write the corresponding continuous time integral equation for the system.

$$\underline{x}(t) = \Phi(t - t_0)\underline{x}(t_0) + \int_{t_0}^{t} \Phi(t - t')\underline{\varepsilon}(t')\delta t' + \int_{t_0}^{t} \Phi(t - t')\underline{u}(t')\delta t'$$

where the transition matrix Φ is the matrix exponential:

$$\Phi(t) = e^{Ft} = I + Ft + \frac{1}{2}F^2t^2 + \frac{1}{6}F^3t^3 + ... = \sum_{k=0}^{+\infty} \frac{1}{k!}F^k t^k$$

By introducing a fictitious sample time T_s we can now write the discrete time system model equation introduced at the beginning:

$$\underline{x}[n] = \Phi\underline{x}[n-1] + \underline{\eta}[n-1] + b\underline{u}[n-1]$$

$$x[n] = \Phi x[n-1] + \int_{(n-1)T_s}^{nT_s} \Phi(nT_s - t')\varepsilon(t')\delta t' + \int_{(n-1)T_s}^{nT_s} \Phi(nT_s - t')u(t')\delta t'$$

with a certain initial condition given by $x[0] = x_0$.

Let's now assume that the x and y coordinates of the boat are measured through a GNSS receiver which at every sample time n provides the right position plus some gaussian noise.

$$z_x[n] = x[n] + v_x[n]$$

$$z_y[n] = y[n] + v_y[n]$$

By assigning $z_1[n] = z_x[n]$ and $z_2[n] = z_y[n]$ we can write the measurement vector as:

$$\begin{bmatrix} z_1[n] \\ z_2[n] \end{bmatrix} = \begin{bmatrix} 1 & 0 & 0 & 0 \\ 0 & 0 & 1 & 0 \end{bmatrix} \cdot \begin{bmatrix} x_1[n] \\ x_2[n] \\ x_3[n] \\ x_4[n] \end{bmatrix} + \begin{bmatrix} v_1[n] \\ v_2[n] \end{bmatrix}$$

according to the form $\underline{z}[n] = H\underline{x}[n] + \underline{v}[n]$ presented at the beginning.

Thus summarizing:

- $\underline{x}[n] = \Phi\underline{x}[n-1] + \underline{\eta}[n-1] + b\underline{u}[n-1]$
- $\underline{z}[n] = H\underline{x}[n] + \underline{v}[n]$

where $\underline{\eta}[n-1] \sim N(0, Q)$ and $\underline{v}[n] \sim N(0, R)$ are statistically independent.

Now the reader has all the necessary background to follow the iterations that will explain why and how the Kalman Filter provides a **linear**, **unbiased**, **optimal** and **recursive** estimate $\underline{\hat{x}}[n]$ of the dynamical system's state $\underline{x}[n]$ from its noisy measurements $\underline{z}[n]$.
Familiarize for a moment with Figure B.3 and try guessing its nomenclature which, however, will be shortly explained...

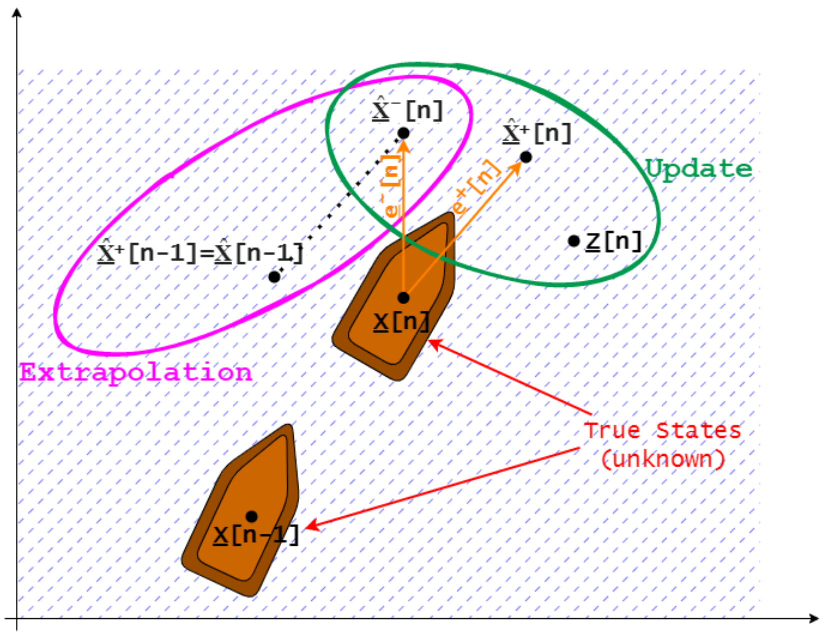

Figure B.3: Extrapolation and Update

The estimation process is composed of two steps, to be repeated at each time n: an **extrapolation** and an **update** phase. At this point the reader should remember that we had to spend some time to figure out a physical model of our system: well that is crucial for extrapolating the state vector $\underline{x}^-[n]$ from its estimate at time $n-1$. In fact, $\underline{x}^-[n]$ is nothing less than our best estimate, based on the previous one made at time $n-1$, of the system state at time n if we had no measurements for time n, thus only relying on the physical model that we built. Since however we hope to receive some position measurements at time n, we can exploit $\underline{z}[n]$ to **update** the extrapolated state vector $\underline{x}^-[n]$ and define the final estimate for time n ($\underline{x}^+[n]$) by a linear combination of

the two quantities. Of course, both in the extrapolated system state and in the one updated with the measures we inevitably commit errors, respectively denoted as $e^-[n]$ and $e^+[n]$.
Therefore, reminding that we are seeking for a **linear**, **recursive**, **unbiased** and **optimal** state estimate, it is possible to already define the Kalman estimator exploiting the first two mentioned properties.

$$\underline{\hat{x}}^+[n] = k'[n]\underline{\hat{x}}^-[n] + k[n]\underline{z}[n] \qquad\qquad Kalman\ Estimator$$

In the presented equation $k'[n]$ and $k[n]$ are matrices, the latter being usually referred to as the Kalman Gain.

The goal is to find these matrices, which at this point are of course still unknown. By imposing the estimator to be **unbiased** it is possible to find the value of $k'[n]$ as a function of the Kalman Gain! Remembering that being unbiased for and estimator implies that its mean estimation error is zero we can proceed as follows:

$$Since\ it\ holds\ that: \begin{cases} \underline{x}^-[n] = \underline{x}[n] + \underline{e}^-[n] & (1) \\ \underline{x}^+[n] = \underline{x}[n] + \underline{e}^+[n] & (2) \end{cases}$$

We can substitute (1) and (2) in the equation of the Kalman estimator:

$$\underline{x}[n] + \underline{e}^+[n] = k'[n](\underline{x}[n] + \underline{e}^-[n]n) + k[n](H\underline{x}[n] + \underline{v}[n])$$

$$\underline{e}^+[n] = -\underline{x}[n] + k'[n]\underline{x}[n] + k'[n]\underline{e}^-[n] + k[n]H\underline{x}[n] + k[n]\underline{v}[n]$$

$$\underline{e}^+[n] = (k'[n] + k[n]H - I)\underline{x}[n] + k'[n]\underline{e}^-[n] + k[n]\underline{v}[n]$$

As said, for the estimator to be **unbiased** it must be $E\left[\underline{e}^+[n]\right] = 0$

$$E\left[(k'[n] + k[n]H - I)\underline{x}[n]\right] + E\left[k'[n]\underline{e}^-[n]\right] + E\left[k[n]\underline{v}[n]\right] = 0$$

By moving out of the ensemble averages the deterministic quantities:

$$(k'[n] + k[n]H - I)E\left[\underline{x}[n]\right] + k'[n]E\left[\underline{e}^-[n]\right] + k[n]E\left[\underline{v}[n]\right] = 0$$

The result of the first E operator is the only one different from zero since the boat moves, while the results of the second and third E

operators are zero because in the long run the system model must hold unbiased (it can be shown that $\underline{\hat{x}}^-[n] = \Phi\underline{\hat{x}}^+[n-1] + b\underline{u}[n-1]$ is an unbiased estimator for $\underline{x}^-[n]$) and because $\underline{v}[n]$ is Gaussian with zero mean. Therefore in order to respect $E\left[\underline{e}^+[n]\right] = 0$, we must set:

$$(k'[n] + k[n]H - I) = 0$$

$$\Rightarrow k'[n] = I - k[n]H$$

Substituting:

$$\underline{x}^+[n] = (I - k[n]H)\underline{x}^-[n] + k[n]z[n]$$

$$\underline{e}^+[n] = (I - k[n]H)\underline{e}^-[n] + k[n]\underline{v}[n]$$

Now, in order to find the Kalman Gain $k[n]$, the **optimality** property of the Kalman estimator has to be exploited: that is, the variance of the estimates must be minimum! Therefore, the average length of the estimation error, namely $E\left[\ ||\underline{e}^+[n]||\ \right]$ has to be minimized.
Being $||\underline{e}^+[n]|| = \sqrt{e_1^+[n]^2 + e_2^+[n]^2 + ... + e_M^+[n]^2}$, it is equivalent to minimize $E\left[\ ||\underline{e}^+[n]||^2\ \right] = E\left[e_1^+[n]^2 + e_2^+[n]^2 + ... + e_M^+[n]^2\right] = E\left[e_M^+[n]^2\right] + ... + E\left[e_M^+[n]^2\right]$ At this point it can be noted that this summation to be minimized corresponds to the trace of the update error covariance matrix $P^+[n]$:

$$P^+[n] = E\left[\underline{e}^+[n]\underline{e}^+[n]^T\right] = E\begin{bmatrix} e_1^+[n]^2 & ... & ... & e_1^+[n]e_M^+[n] \\ : & e_2^+[n]^2 & ... & : \\ : & ... & ... & : \\ e_M^+[n]e_1^+[n] & ... & ... & e_M^+[n]^2 \end{bmatrix}$$

We are now convinced that $trP^+[n] = E\left[\ ||\underline{e}^+[n]||^2\ \right]$ where $trP^+[n]$ is the trace of the covariance matrix and has to be minimized.

$$\Rightarrow \frac{\delta}{\delta k[n]} trP^+[n] = 0$$

In particular:

$$P^+[n] = E\left[\underline{e}^+[n]\underline{e}^+[n]^T\right]$$

$$P^+[n] =$$

$$E[\left[(I - k[n]H\underline{e}^-[n] + k[n]\underline{v}[n]\right] \cdot \left[(I - k[n]H)\underline{e}^-[n] + k[n]\underline{v}[n]\right]^T]$$

$$=$$

$$E\left[\left[(I - k[n]H)\underline{e}^-[n] + k[n]\underline{v}[n]\right] \cdot \left[\underline{e}^-[n]^T(I - k[n]H)^T + \underline{v}[n]^T k[n]^T\right]\right]$$

$$=$$

$$E\left[(I - k[n]H)\underline{e}^-[n]\underline{e}^-[n]^T(I - k[n]H)^T\right] + E\left[k[n]\underline{v}[n]\underline{v}[n]^T k[n]^T\right] +$$

$$+E\left[(I - k[n]H)\underline{e}^-[n]\underline{v}[n]^T k[n]^T\right] + E\left[k[n]\underline{v}[n]\underline{e}^-[n]^T(I - k[n]H)^T\right]$$

Letting all the deterministic quantities out of the E operator:

$$P^+[n] =$$

$$(I - k[n]H)E\left[\underline{e}^-[n]\underline{e}^-[n]^T\right](I - k[n]H)^T + k[n]E\left[\underline{v}[n]\underline{v}[n]^T\right]k[n]^T +$$

$$+k[n]E\left[\underline{v}[n]\underline{e}^-[n]^T\right](I - k[n]H)^T$$

$$P^+[n] =$$

$$(I - k[n]H)P^-[n](I - k[n]H)^T + k[n]Rk[n]^T$$

where $P^-[n]$ and R are symmetric because are covariance matrices. Since $tr(A + B) = trA + trB$ and $\frac{\delta}{\delta k[n]}$ is a linear operator:

$$\frac{\delta}{\delta k[n]} trP^+[n] =$$

$$\frac{\delta}{\delta k[n]} tr(I - k[n]H)P^-[n](I - k[n]H)^T + \frac{\delta}{\delta k[n]} trk[n]Rk[n]^T = 0$$

Since $\frac{\delta}{\delta A} trABA^T = 2AB$ and $\frac{\delta}{\delta A} trAB = B^T$:

$$\Rightarrow -2(I - k[n]H)P^-[n]H^T + 2k[n]R = 0$$
$$\Rightarrow -P^-[n]H^T + k[n]HP^-[n]H^T + k[n]R = 0$$
$$\Rightarrow k[n] = P^-[n]H^T(HP^-[n]H^T + R)^-1 := Kalman\ Gain$$

The found value of $k[n]$ is by construction the one that minimizes the estimates' variance. Note that a linear and unbiased estimator for $P^-[n]$ is given by $\hat{P}^-[n] = \Phi P^+[n-1]\Phi^T + Q$

Summary of Equations:

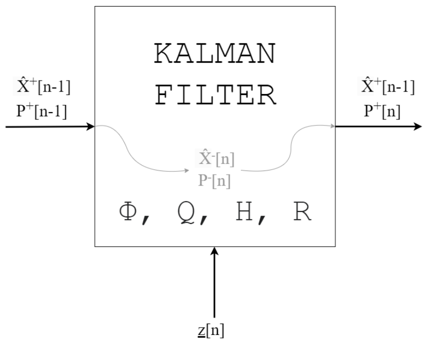

- System Model Equation
  $\underline{x}[n] = \Phi\underline{x}[n-1] + \underline{\eta}[n-1] + b\underline{u}[n-1]$
- Measurement Model Equation
  $\underline{z}[n] = H\underline{x}[n] + \underline{v}[n]$
- Initial Conditions
  $\hat{\underline{x}}[0] = E\left[\underline{x}[0]\right]$
  $P[0] = E\left[(\hat{\underline{x}}[0] - \underline{x}[0])(\hat{\underline{x}}[0] - \underline{x}[0])^T\right]$
- State Estimate Extrapolation
  $\hat{\underline{x}}^-[n] = \Phi\hat{\underline{x}}^+[n-1] + b\underline{u}[n-1]$
- Error Covariance Extrapolation
  $\hat{P}^-[n] = \Phi P^+[n-1]\Phi^T + Q$
- Kalman Gain
  $k[n] = P^-[n]H^T(HP^-[n]H^T + R)^-1$
- State Estimate Update
  $\hat{\underline{x}}^+[n] = (I - k[n]H)\hat{\underline{x}}^-[n] + k[n]\underline{z}[n]$
- Error Covariance Update
  $P^+[n] =$
  $(I - k[n]H)P^-[n](I - k[n]H)^T + k[n]Rk[n]^T$

Bibliography

[1] *"Technology Readiness Level Definitions"*. "NASA". URL: https://www.nasa.gov/pdf/458490main_TRL_Definitions.pdf (cit. on p. 8).

[2] *"Technology Readiness Level Definitions"*. Extract from Part 19 - Commission Decision C(2014)4995". "ESA". URL: https://ec.europa.eu/research/participants/data/ref/h2020/wp/2014_2015/annexes/h2020-wp1415-annex-g-trl_en.pdf (cit. on p. 8).

[3] L. Vigna et al. «Design and Validation of an Autonomous Orbit Determination System for a Smallsat Constellation». In: *29th IAA Symposium On Small Satellite Missions*. Paris, France, Sept. 2022 (cit. on p. 10).

[4] SFCG. *"Frequency Assignment Guidelines For Communications in the Mars Region"*. Recommendation SFCG 22-1R4. 10 December 2021 (cit. on p. 12).

[5] Jet Propulsion Laboratory. *"DSN Telecommunications Link Design Handbook"*. 810-005, Rev. E. November 2000. URL: https://deepspace.jpl.nasa.gov/dsndocs/810-005/ (cit. on pp. 13, 24, 35).

[6] ANYWAVES. *X-Band Payload Telemetry Antenna*. URL: http://space-for-space.com/wp-content/uploads/2018/12/ANYWAVES-X-Band-Payload-Telemetry-Antenna-datasheet.pdf?msclkid=51cc8fc7b64311ec878ad57a1f754202 (cit. on p. 14).

[7] CCSDS. *"Data Transmission and PN Ranging For 2 GHz CDMA Link via Data Relay Satellite"*. Recommended Standard. CCSDS 415.1-B-1. September 2011. URL: `https://public.ccsds.org/Pubs/415x1b1.pdf` (cit. on pp. 16, 43, 64).

[8] CCSDS. *"Data Transmission and PN Ranging For 2 GHz CDMA Link via Data Relay Satellite"*. Informational Report. CCSDS 415.0-G-1. April 2013. URL: `https://public.ccsds.org/Pubs/415x0g1.pdf` (cit. on pp. 16, 43–47, 49, 50, 52, 54, 55, 57, 64).

[9] "Catherine L.Thornton - James S.Border - Jet Propulsion Laboratory - California Institute of Technology". *"Radiometric Tracking Techniques for Deep-Space Navigation"*. JPL Publication 00-11. October 2000. URL: `https://descanso.jpl.nasa.gov/monograph/series1/Descanso1_all.pdf` (cit. on pp. 28, 34).

[10] J.P. Costas. «Synchronous communications». In: *Proceedings of the IEEE* 90.8 (2002), pp. 1461–1466. DOI: `10.1109/JPROC.2002.800876` (cit. on p. 38).

[11] Mauro Di Benedetto, Luigi Imperi, Daniele Durante, Michele Dougherty, Luciano Iess, Virginia Notaro, and Paolo Racioppa. «Augmenting NASA Europa Clipper by a small probe: Europa Tomography Probe (ETP) mission concept». In: Sept. 2016 (cit. on p. 40).

[12] Lorenzo Galleani and Patrizia Tavella. «Time and the Kalman Filter». In: *IEEE Control Systems Magazine* 30.2 (2010), pp. 44–65. DOI: `10.1109/MCS.2009.935568` (cit. on p. 76).

[13] Lorenzo Galleani and Ilaria Sesia. «The Corrected Allan Variance: Stability Analysis of Frequency Measurements With Missing Data». In: *IEEE Transactions on Ultrasonics, Ferroelectrics, and Frequency Control* 66.10 (2019), pp. 1667–1683. DOI: `10.1109/TUFFC.2019.2927424` (cit. on p. 79).